Spring 1-1-2016

A Reduced Order Model of an External Compression Supersonic Inlet

Kyle Joseph Woolwine
University of Colorado at Boulder, kyle.woolwine@colorado.edu

A Reduced Order Model of an External Compression Supersonic Inlet

by

Kyle J. Woolwine

A.A., General Studies, Edison State College, 2007

B.S., Aerospace Engineering, University of Florida, 2011

B.S., Mechanical Engineering, University of Florida, 2011

A thesis submitted to the

Faculty of the Graduate School of the

University of Colorado in partial fulfillment

of the requirements for the degree of

Doctor of Philosophy

Department of Aerospace Engineering

2016

This thesis entitled:
A Reduced Order Model of an External Compression Supersonic Inlet
written by Kyle J. Woolwine
has been approved for the Department of Aerospace Engineering

Prof. Kenneth Jansen

Prof. Peter Hamlington

Date

The final copy of this thesis has been examined by the signatories, and we find that both the content and the form meet acceptable presentation standards of scholarly work in the above mentioned discipline.

Woolwine, Kyle J. (Ph.D., Aerospace Engineering)

A Reduced Order Model of an External Compression Supersonic Inlet

Thesis directed by Prof. Kenneth Jansen

The research contained in this thesis was performed in order to model the external compression axisymmetric inlet portion of a supersonic jet engine in a way that captures the effects of a full 3-D CFD model while maintaining the quickness of a lower dimensional model. This was accomplished by first creating high fidelity 3-D and 2-D models with the CFD code PHASTA. These models were used as base models to both verify and drive the creation of the lower dimensional model. The lower dimensional 1-D model, created in MATLAB, was developed by piecing together established methods with novel ones. In particular, a new approach was developed in order to properly model the dynamics of the inherently three dimensional external compression flow field. With comparison to the higher order PHASTA models, the lower order model proved capable of accurately modeling both the steady state and dynamic response of the the external compression supersonic inlet. This was accomplished approximately 13,000 times more efficiently than using the higher order CFD models. The results of this research provided a lower dimensional supersonic inlet model that maintains the dynamic accuracy of a higher order CFD model while exhibiting the benefit of quick execution time and adaptability allowed by its simpler construction.

Dedication

To my parents, I couldn't have done this without their unwavering love and support.

Acknowledgements

Undertaking a Ph.D. requires an immense amount of dedication and time. I would like to thank my family, friends and my Chelsea for their support and patience during this process. I would also like to thank Dr. Kenneth Jansen and George Kopasakis for their belief in my abilities and for giving me the opportunity to preform this research.

Contents

Chapter

Tables

Table

Figures

Figure

Chapter 1

Introduction

The following scientific investigation stems from ongoing research that is intended to meet specific goals of the of the AeroServoElasticity (ASE) task in the Supersonics Project under the Fundamental Aeronautics Program, which aims to investigate integrated vehicle performance such as ride quality, vehicle stability and integrated controls. The focus in this thesis is to develop and verify a dynamic model of the external compression inlet, baselined for the supersonic propulsion system, that will be integrated with the rest of the propulsion system and the structure-aerodynamic vehicle model in order to allow for these integrated AeroPropulsoServoElasticity studies.

The focus of this research will be on modeling the baseline axisymmetric inlet geometry to include both the external and internal inlet portions (before the engine face), extending the flow field to the freestream, which is necessary to capture the conical flow field. It is important to accurately model the engine inlet because its dynamic response to freestream flow fluctuations can couple with the propulsion dynamics and with the full APSE system to cause performance challenges such as vehicle ride quality and stability (Figure 1.1). This can occur from pressure, temperature or Mach number disturbances in the free stream due to atmospheric turbulence and/or vehicle maneuvering, together with flow field disturbances caused by potential excitation of the vehicle structural modes. These disturbances can enter the inlet and the engine to affect the thrust dynamics, which in turn can couple back to the structural modes of the vehicle to disturb the flow field into the inlet, acting as a closed loop system.

Under most steady state flight conditions the solution of a conical flow in the inlet can be

modeled using a well established technique such as the axisymmetric method of characteristics method [4]. However, the inlet model must also be able to handle variations in pitch as part of APSE model dynamics and the flow field in that case will become inherently three dimensional. This poses a dilemma because the current ASPE model is written in Simulink and developing a time efficient 3-D CFD code in Simulink would be extremely difficult if not impossible. There are two possible solutions to this problem; either run an external CFD code on a parallel cluster which is called by Simulink during simulations or create a simpler, scaled down, two or one dimensional approximation of the flow field, using dynamic variables developed from the results of a high fidelity CFD code, to approximate the inherently three dimensional flow. This necessitates the use of a high fidelity 3-D CFD code to be either used directly as in the first case or indirectly and as a verification tool in the second case. As will be discussed in further detail, the research described here will focus on the second option as that is deemed to be the less problematic of the two choices. This will be carried out using the CFD code PHASTA as the verification tool to create 3-D and 2-D models. Using the results from these models, a quasi 1-D CFD model will be created in simulink

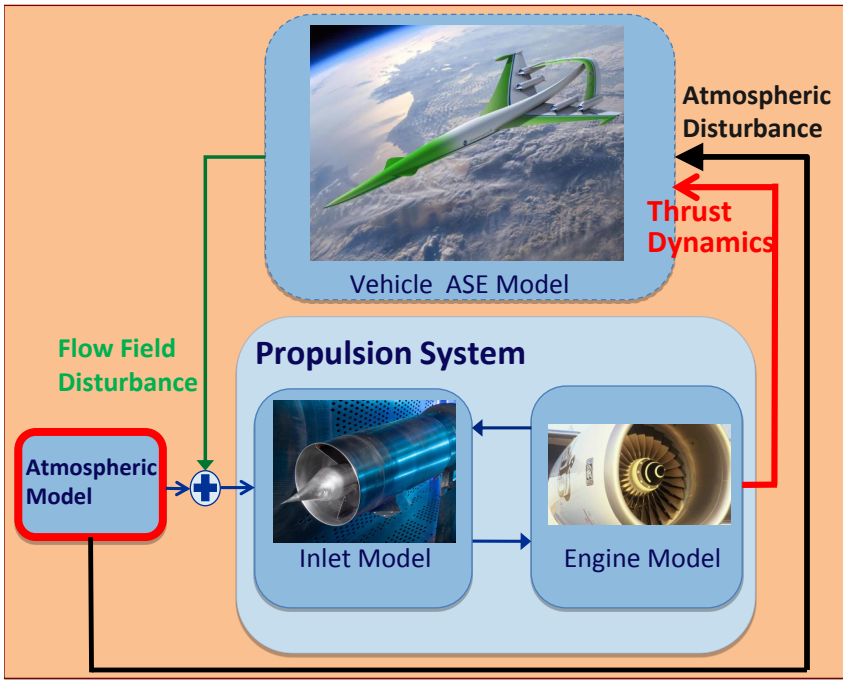

Figure 1.1: AeroServoElastic Model Overview (Kopasakis[33])

and inserted into the overall ASPE model. The creation of the verified quasi 1-D CFD model that accurately captures the 3-D effects of the true model is the basis of the thesis.

Chapter 2

Background

As mentioned, the purpose of this research is to create a quasi 1-D inlet model that captures the dynamic effects of the inherent 3-D flow field. In order to understand the issues facing this task, it is best to split the flow field into five main sections and discuss the problems facing modeling each region. The first region is the atmospheric model where the inflow plane of the model is defined. This region includes the inflow boundary conditions as well as the turbulence models from which the perturbation tests are based. The next region includes the external conical shock wave and subsequent isentropic compression. The remaining regions of interest are the normal shock, the cowl lip and associated mass spillage and finally the internal subsonic region which leads to the compressor face. Following the discussion of the different regions of the inlet will be a discussion on the current inlet models being used and their strengths and weaknesses.

2.1 Research Scope

Before proceeding into the details of the various modeling techniques and background of supersonic inlets, it is a good idea to give a scope of the contained research. The end result of this research is to provide collaborators at NASA Glenn with a dynamic supersonic inlet model written in the Matlab/Simulink environment that they can 'plug' into a larger propulsion system model. This model will be combined with an aero-elastic model of the aircraft structure to create an overall aero-propulso-servo-elastic model. The inlet model thats described here will have flow variable input variables from the free stream, including atmospheric disturbances and output flow

variables of mass flow rate, temperature, pressure, and velocity that will act as inputs to the turbo-machinery.

The inlet model was created by piecing together several established modeling techniques, altering them when necessary and using the approach that the model should be as simple as possible but not simpler. The intent is to capture the relevant dynamics of the inherently 3D flow field while minimizing computational expense. In order to accomplish this several assumptions had to be made. The first is that the free stream perturbations resulting from atmospheric turbulence or sudden vehicle maneuvers will be modeled using small perturbations to individual flow variables at the inflow plane of the inlet. Modeling disturbances in this way, will cause the perturbation to travel through the inlet as two acoustic wave (δ^+, δ^-) and an entropy wave(δ^e) from the source of the perturbation (i.e. the tip of the inlet). In reality, the disturbance will propagate from a source further upstream. This is not seen as an issue because the point of this research is to create a model capable of responding to inflow disturbances regardless of their source. The current approach is to use atmospheric turbulence models to determine the amplitude and frequency range that will exist in reality and apply perturbations to the individual flow variables within that range. A more detailed discussion of this approach will follow in the next section.

The second assumption, is that the flow field may be approximated as inviscid. Indeed, the unsteady 3-D viscous CFD results from both Chima et. al. and Conway et. al. show little boundary layer separation in the flow of the their simulations [12, 16]. It is recognized that normal shock movement due to perturbation may cause increased separation and thus effect the assumption that the quasi 1D Euler equations are accurately capturing the dynamics of the flow field. However, for this research effort it is assumed that the volume dynamics of the bulk flow will be the greater contributor to this effect. Furthermore, many inlets use bleed to reduce the amount of separation experienced by the inlet so this assumption is deemed acceptable.

The last main assumption, is that the upstream vehicle effects, such as the oblique shock wave which emanates from wing (Figure 2.2), will not be considered. Essentially, this results in modeling a 'flying inlet' or perhaps an inlet in a wind tunnel without wall effects. This assumption

Figure 2.1: N + 2 Concept Vehicle (Connolly [14])

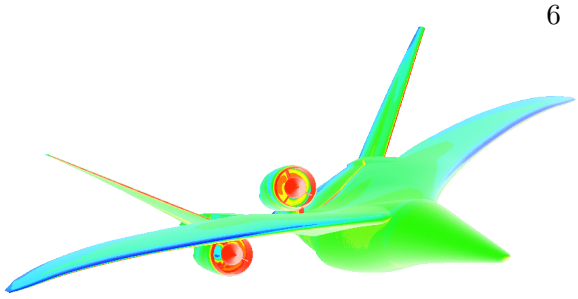

Figure 2.2: Total Vehicle CFD Simulation - Relative Surface Pressure (Connolly [14])

is assumed valid for two reasons. First, the vehicle being studied is still in the conceptual design stage and a physical prototype does not exist (Figure 2.1). Spending a lot effort modeling this specific configuration would most likely be wasted down the road. Second, the modeling techniques of this inlet model are robust and general enough to account for changes in geometry or free stream conditions later on. For this reason, free stream conditions are assumed to enter the inlet unimpeded by aircraft affects.

Lastly, in connection with the previous statement, the inlet is modeled at cruise altitude with zero base line angle of attack. While this does prevent the inlet model from used over the entire flight envelope, it would not take a complete overhaul of the model to add this capability. However, due to time constraints, it was not possible to include this capability. The final chapter of this paper will detail potential options for further work.

2.2 Atmospheric Model

The atmospheric model contains the inflow boundary conditions and how they should vary to properly simulate the steady state conditions, atmospheric turbulence and the effects that vehicle maneuvering have on the incoming flow field. For purposes of this research all flight conditions will be considered supersonic and as such, the flow must be completely defined at the furtherest point upstream. This is because at the inlet of supersonic flows the viscous terms in the Navier-Stokes equations are of negligible scale and thus all the characteristics point downstream [4]. In the case

of the Euler equations, the result is that the pressure, velocity, and temperature must be defined at the inflow plane. These states at the steady state condition are defined simply by altitude and flight Mach number using an atmospheric properties table [6].

Properly defining the inflow condition becomes more difficult when atmospheric perturbations are introduced. The literature shows that most methods for handling this are based off of a variation of the Kolmogorov turbulence model [31, 53, 42, 18]. In this model, turbulence is considered locally isotropic and kinetic energy cascades from large eddies to smaller ones until the length scales become small enough that the kinetic energy is dissipated as heat [30]. The rate in which this happens is dependent on the eddy dissipation rate. However this model used by itself is problematic because the energy approaches infinity as frequency approaches zero [31, 32]. Many models therefore use the von Karmen model which is similar to the Kolmogorov method but with finite energy. One of the more popular atmospheric models is based off of the von Karmen turbulence model and was developed by Tank et. al [53, 54]. This model is similar to the Kolmogorov method in that it follows the -5/3 power law seen in Equation(2.1) but levels off at lower wave numbers as seen in Figure 2.3. An additional model named the Dryden model developed by Hoblit [24] uses a second

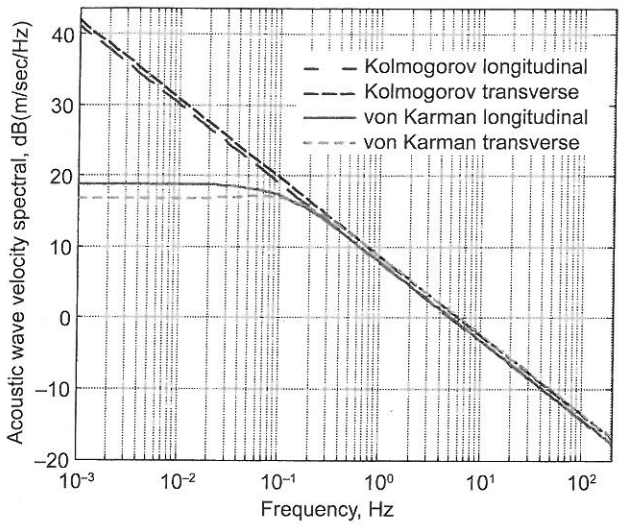

Figure 2.3: Acoustic wave velocity spectral comparisons for the Kolmogorov and Von Karman spectral (Kopasakis[32])

order approximation of the 5/3 fractional order of the energy spectral. However, as Kopasakis notes [32] this model underestimates the magnitude of the atmospheric turbulence.

$$S_t(k) = \alpha_t \epsilon^{2/3} k^{-5/3} \tag{2.1}$$

Kopasakis's atmospheric disturbance model differs from previous models mainly in that he uses integer order transfer functions to approximate the fractional order transfer functions of the von Karman model. His model was created specifically for analyzing and developing control systems for supersonic propulsion models in the Simulink environment. The model was created using a circuit analog as a basis to derive the pole-zero product approximate transfer functions. The transfer function approximation works by "interleafing" integer order poles and zeros symmetrically about the von Karman transfer function using the turbulence parameters until the approximation falls on top of the von Karman model as seen in Equation (2.2).

$$W_{t,o} \cong K_{t,fit} \frac{\prod_{1}^{m_z}(s/\omega_{zi} + 1)}{\prod_{1}^{m_p}(s/\omega_{pi} + 1)} W_t \tag{2.2}$$

Here the proportional gain $K_{t,fit}$ differs depending on the type of turbulence being modeled and is based off of the model developed by Tank. For instance, if a temperature disturbance is being simulated $K_{t,fit}$ can be calculated from Equation (2.3). Figure 2.4(a) show the results as compared to the fractional order von Karman model.

$$K_{T,fit(temp)} = \sqrt{14.0 \varepsilon^{2/3} L^{5/3}} \tag{2.3}$$

From Equation (2.3) it can be seen that the proportional gain is dependent on both eddy viscosity and integral length (turbulence patch length). Kopasakis notes that observations show an offset in magnitude but not frequency when eddy viscosity is changed. Integral length scale however does effect frequency response but only at very low frequencies where typical feedback control design would have no problem handling. The effects of eddy viscosity and integral length

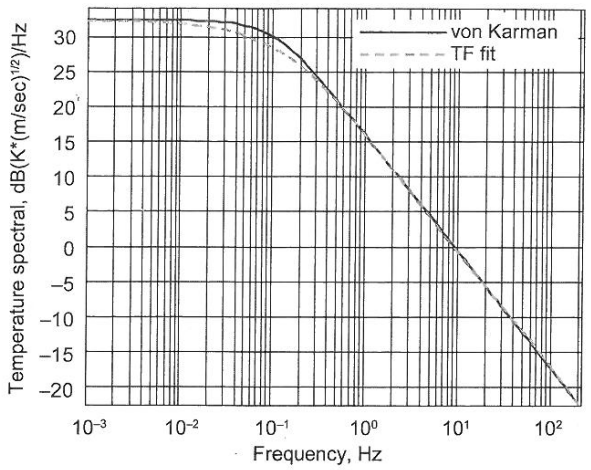

(a) Temperature von Karman spectral and its TF fit

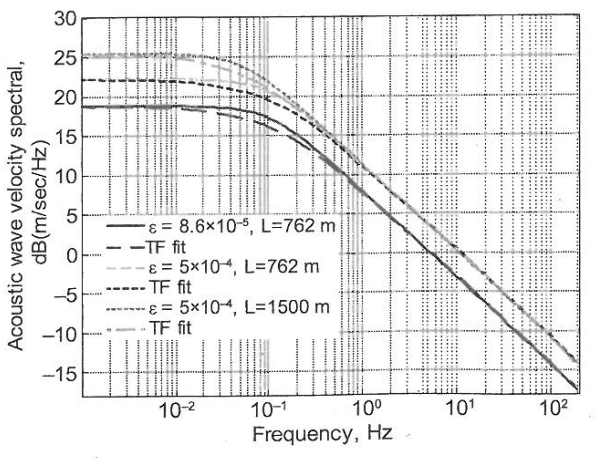

(b) von Karman longitudinal acoustic wave velocity spectral and its TF due to different values of eddy dissipation rates and integral length scales

Figure 2.4: Kopasakis Turbulence Model Results [32]

scale on the turbulence model can be seen in Figure 2.4(b). A simplified model can therefore be developed using poles and zeros for industry standard length scale of 762m and by making gain adjustments strictly from eddy viscosity. This simplified model is the one which is implemented in Simulink. Again using temperature disturbances as an example, Equation (2.4) displays what this looks like.

$$G_T(s) = 943\varepsilon^{2/6}\frac{(s/33.0+1)(s/45.6+1)(s/602.4+1)}{(s/1.1+1)(s/25.1+1)(s/109.8+1)(s/816.3+1)} \tag{2.4}$$

The resulting atmospheric turbulence model (implemented in Simulink as shown in Figure 2.5) provides the correct magnitude perturbations for each flow variable (P, T, rho, u, v) based on the desired frequency disturbance to model. This model will eventually be used to analyze the lower order inlet. For now small amplitude single frequency flow variable perturbations will be applied to the PHASTA and Simulink models in the frequency range of interest to analyze it's dynamic behavior.

In addition to the differences found amongst the atmospheric models there are also a variety of different ways to apply the atmospheric disturbances in a larger model. Ashun [1] used the Tank

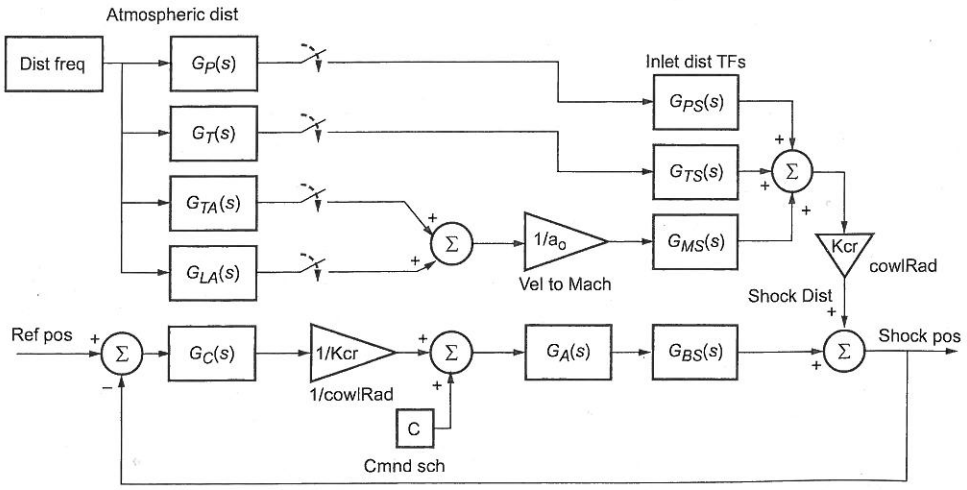

Figure 2.5: Feedback control diagram of inlet shock position system with disturbance model (Kopasakis[32])

model as the source of the disturbance and applied them to his inlet model as a combination of characteristic forms (a fast moving acoustic wave *J+*, slow moving acoustic wave *J-*, or entropy wave). These forms are regarded by the author as 'fundamental modes' of the atmospheric disturbances and are applied by perturbing three of the flow variables simultaneously to propagate a single characteristic wave. These modes are what Ashun used to develop the controller laws used to stabilize his inlet model. Conversely, Kopasakis [31, 32] used his atmospheric model to apply the disturbances to the individual flow variables. Applying these individual disturbances is similar to the Ashun model in that they will cause the three characteristic modes to propagate through the inlet simultaneously. This is similar to a Reimann problem using a shock tube as described in [29]. The difference is that in the Ashun model, the controller design will be based off characteristic mode disturbances whereas using the Kopasakis model will results in a controller design based off of flow variable perturbations. Therefore, the response of the inlet and subsequent designed control laws will be accurate as long as the user is consistent.

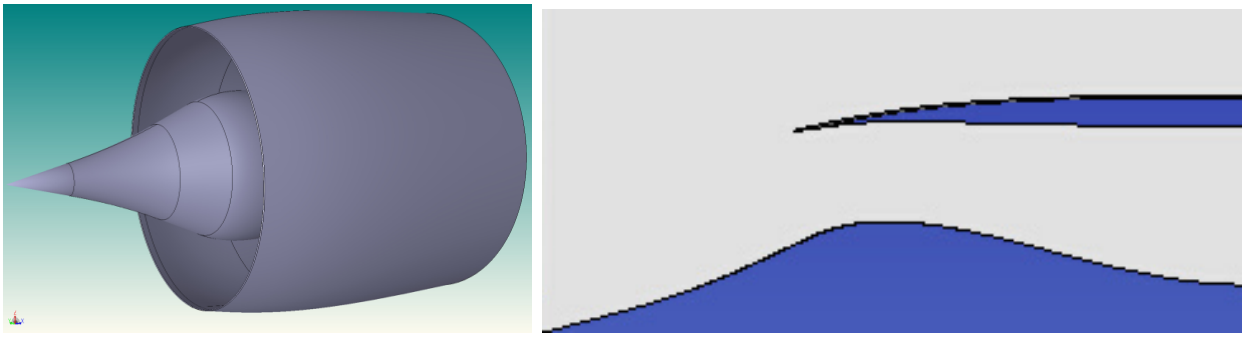

(a) 3-D View (b) 2-D Slice

Figure 2.6: Axisymmetric Inlet

2.3 External Compression

Supersonic inlets have a moderate degree of variation in their shape and flow field characteristics but they all are designed to perform the same basic function, which is to provide the compressor face of the turbo machinery with the required amount of subsonic flow in the most efficient way possible and with the least amount of distortion [50]. Therefore, careful thought and design are dedicated to compressing the incoming air as close to isentropically and with as little boundary layer separation as possible. Depending on the flight regime and position of the engines, the shape of the inlet will vary to accomplish these objectives. For aircraft operating near sonic conditions, pitot inlets and streamlined Buseman designs are common due to weakness of the shock field. If the operating point is at a higher Mach number near ≈ 2, it is common to use an axisymmetric external compression inlet design. According to Slater [51], "external-compression inlets are considered better choices for flight Mach numbers below Mach 2.0 due to greater shock system stability and the possibility of simpler inlet mechanisms". Beyond a Mach number of 2, conditions are such that mixed compression inlets (2-D, 2-D bifurcated, and axisymmetric) become more efficient. For the purposes of this research, the focus will be on axisymmetric external compression inlets and their specific characteristics.

The exterior of a typical external compression axisymmetric inlet is characterized by an external cone of a fixed angle followed followed by either a smooth or abrupt transition to a larger

angled cone (Figure 2.6). The purpose of this is to compress the flow through a series of conical shocks as close to isentropically as possible. The greater number of angle transitions (and therefore shocks) in the centerbody, the closer to isentropic conditions the flow is compressed. Ideally, the centerbody would start very thin and smoothly transition to the desired angle over a long distance thereby compressing the flow through mach waves instead of shocks. Due to structural instability, this is impossible. It is therefore common for the centerbody to have the shape seen in Figure 2.6(a). In Figure 2.6(b), it can be seen that the cone transitions smoothly to a larger angle. This design feature causes the flow to pass through an initial shock wave at the tip of the centerbody and smoothly compress afterwards though a series of Mach waves which coalesce in a shock wave at the cowl lip. If this section was instead replaced by an abrupt change in cone angle, a second shock wave would emanate from the centerbody. While this design feature results in closer to isentropic compression and therefore more efficient compression, it nonetheless makes modeling this field more difficult.

Steady supersonic flow around a semi-infinite cone, at zero angle of attack, can be solved using the Taylor-Maccoll equations [4, 56]. Under these conditions the flow is axisymmetric and the flow properties are constant along rays (Figure 2.7). Using these assumptions, the Navier-Stokes equations (in spherical coordinates) can be reduced to a single ordinary differential equation. Although this equation has no closed-form solution, it can be solved numerically, the solution of which is exact for this flow field. As previously stated, the goal of this research is to develop an inlet model capable of handling variations in free stream conditions as well as angles of attack. While the assumptions used to develop the Taylor-Maccoll equations would be violated in this case, they can still be used to determine the initial shock wave for the steady state case and in conjunction with other techniques.

Another popular technique for solving steady supersonic flow fields is the method of characteristics. If the flow field is supersonic everywhere, the behavior of the Navier-Stokes equations outside of the boundary layer become more like the Euler equations and become hyperbolic. At a given point there exists a direction in which the local velocity has a Mach number of one. Lines

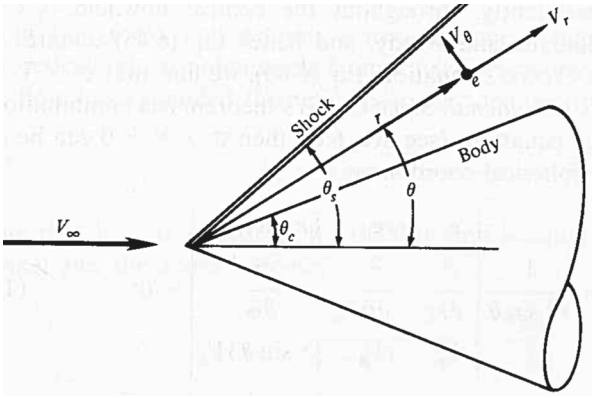

Figure 2.7: Supersonic Conical Flow Field (Anderson[4])

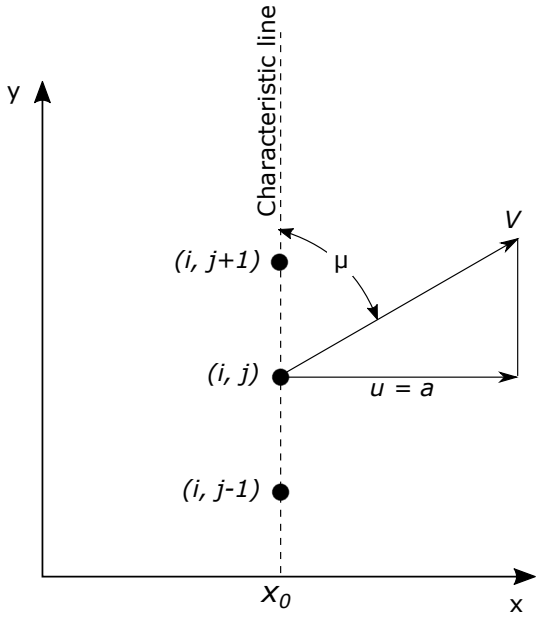

Figure 2.8: Illustration of the characteristic direction. (Anderson[4])

perpendicular to them are Mach lines or characteristic lines as seen in Figure 2.8. Along the characteristic lines the flow variables are continuous but their derivates are indeterminate. The conservations equations may therefore be reduced to ordinary differential equations along these lines and solved for. The procedure for this method is outlined in Anderson and is a popular choice for both inlet design [3, 50, 51] as well as the analysis of inlets [13, 46, 52]. The popularity of this method is due to reduced complexity of solving ODEs rather than PDEs.

The above description of the method of characteristics is related to two dimensional and axisymmetric flow fields. While this method is useful in determining the steady state condition of the external portion of the inlet, it is not applicable when atmospheric disturbances or changes in angle of attack are introduced. One reason is that when changes in angle of attack are introduced, the flow field becomes inherently three dimensional. Fortunately, this method has been extended to three dimensions by Rakich, Chuskin and Sauerwein, amongst others [13, 46, 48]. The extended method, as outlined by Anderson [4], is similar to the lower order methods and involves dividing the flow field into arbitrary number planes around the centerline of the body of revolution. Within

in these planes, information is propagated along characteristic lines and an additional streamline. While, this method accurately solves the flow field, it is considerably more complex and computationally expensive. Likewise, most other solutions to three dimensional flows around axisymmetric bodies involve complex CFD methods as seen in Anderson [4].

The other shortcoming of the original method of characteristics is that it is for steady flow and therefore cannot account for changes in flow variables at the boundaries (i.e. atmospheric changes). Sauerwein has developed a multidimensional unsteady method of characteristics procedure [48]. However, due to its complexity and computational expense, it becomes similar to running a traditional unsteady 3D CFD method (finite difference, finite volume, etc.). Likewise, several authors have created unsteady, dynamic models using 3D CFD, but due to their complexity are limited in there application [22, 43]. Other models have attempted to introduce flow field perturbations by using a simpler method such as the oblique shock relations coupled with a time delay [34]. As will be discussed in greater detail in a later section, this approach does not accurately represent the correct physics and will lead to unacceptably large errors. Summarily, several simplified models exist for determining the steady state flow field of the external compression portion of a supersonic inlet but there does not appear to exist any that can properly simulate the unsteady response to perturbations without resorting to full 3-D CFD.

2.4 Operating Condition

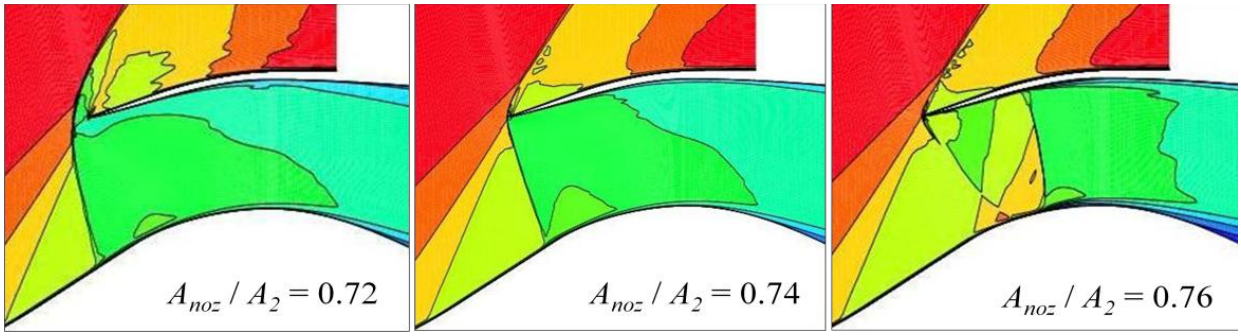

Figure 2.9: External compression inlet Mach contours at sub-critical(left), critical(center), and super-critical(right) operating points (Slater[50]).

External compression axisymmetric inlets are designed for a specific cruise Mach number such that the conical shock field terminates at or just above the cowl-lip and the normal shock sits just outside of the cowl-lip [51](center Mach contour Figure 2.9). The inlets are designed this way for two main reasons. The first is that this operating point (called the critical point) corresponds to the optimal combination of total pressure recovery and mass flow capture. If the normal shock is ingested by the inlet (i.e. supercritical operation), the upstream Mach number before the normal shock increases, the normal shock becomes stronger, and the total pressure loss increases. If the normal shock moves further upstream from the cowl lip (i.e. subcritical operation), there will be greater subsonic mass flow spillage around the cowl lip and the mass flow rate that is fed to the engine will suffer. Where the normal shock sits, and consequently what operating point it is at, will depend on the free stream conditions and the back pressure at the compressor face. This relationship between mass flow capture and total pressure loss as a function of operating condition is illustrated by a standard "cane curve" (Figure 2.10).

If the normal shock is pushed far enough upstream the "buzz" phenomenom will occur. This condition is highly unstable and results in the normal shock oscillating back and forth along

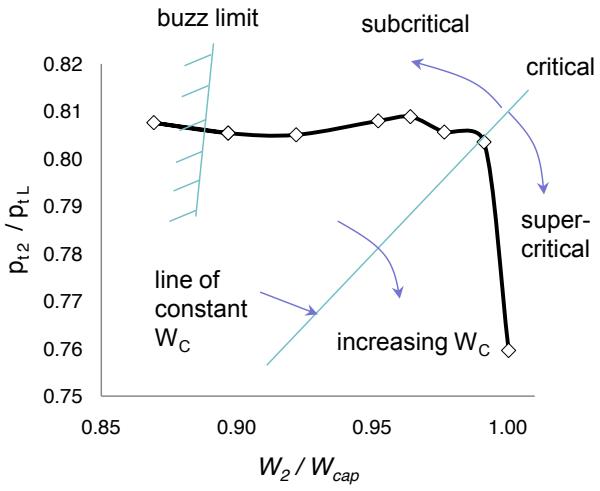

Figure 2.10: Cane Curve Example (Slater[51]).

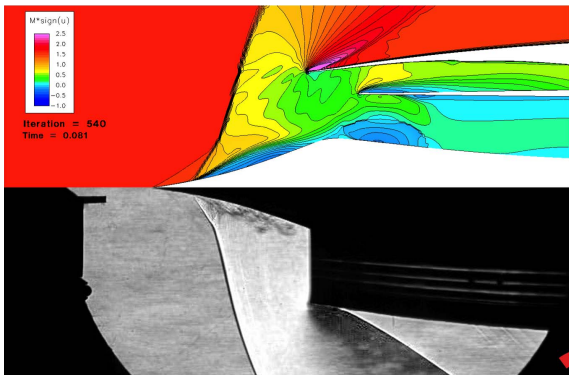

Figure 2.11: Centerbody Separation (Chima[11]).

the external position of the inlet, causing drastic oscillations in pressure and mass rate into the engine [49]. The buzz condition can be initiated either because the shear layer created from the intersection of the oblique and normal shocks is ingested by the inlet or because of separation at the centerbody caused by the normal shock(Figure 2.11). Both of these situations are due to viscous affects.

This leads to the other reason that proper inlet design requires the normal shock to sit just outside of the cowl lip and that is to provide a measure of stability to the inlet by allowing it to absorb perturbations better. Seddon et. al. describe the mechanisms and phenomena that determine the stable operation of an external compression inlet [49]. In it, they list the ingestion of the shear layer created from the intersection of the oblique or conical shock system with the normal shock as a main trigger for causing instability. If the normal shock sits just outside the cowl lip and intersects the oblique shock above the cowl lip, the shear layer will pass over the inlet. Conversely, if the intersection point is at the cowl lip, the system is only marginally stable because perturbations in free stream conditions can cause the intersection point and thus the shear layer to drop below cowl lip and initiate 'buzz".

Additionally, Bogar, et. al. [7] showed that the dynamic response of an external compression inlet will vary depending on the operating point its in. In their experimental work, they found that the inlet's behavior became more nonlinear under critical and especially sub-critical operating conditions. This behavior was more exaggerated when the perturbation frequency was near the natural frequency ("buzz" frequency) of the normal shocks movement. Ideally, a dynamic supersonic inlet model would accurately represent these flow physics. However, as mentioned, the buzz phenomenon is triggered by viscous effects and the model created in this research makes the assumption that the flow field can be approximated as inviscid. This is an important distinction to make because it means that the dynamic response of the model to flow field perturbations will only be valid during the critical and super-critical operating conditions. While this limits its total range of simulation, the model will still be able to predict the operating state that it is in so it is not deemed a critical limitation.

2.5 The Cowl Lip Region

Not many papers in the literature provide detail concerning how to model the normal shock position and subsequent mass flow spillage near the cowl lip in reduced order models. Most of the publications that do describe this are based off of the same model found in the LAPIN report [19, 34, 57]. In the report, subsonic spillage is modeled using a technique developed by Moeckel used to determine the mass flow spillage around a pitot tube or inlet. In Moeckel [41], the author first develops a relationship between distance of detached bow shockwave and a flat faced body and calculated mass flux through an assumed straight sonic line (Figure 2.12(a)). The mass flux properties across the sonic line, indicated with an asterisk, are easily determined though the continuity equation (2.5).

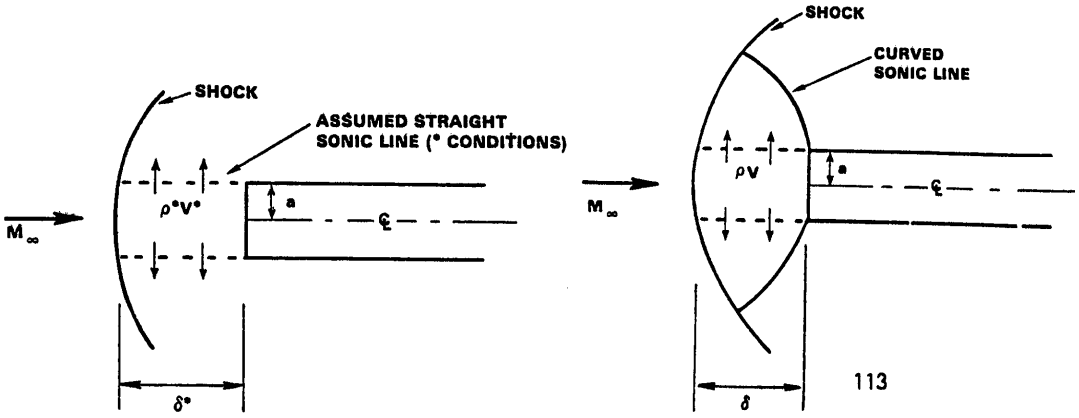

(a) Straight sonic line approximation (b) Curved sonic line

Figure 2.12: Shock Distance and Mass Flow(Varner[57])

$$\frac{\delta^*}{a} = \frac{1}{2^j} \frac{\rho_\infty V_\infty}{\rho^* V^*} \tag{2.5}$$

In reality, the sonic line is curved, as seen in Figure 2.12(b). Moeckel, develops a correction factor F to account for this which relates the mass flow in the real case(Figure 2.12(b)) to the approximate case(Figure 2.12(a)) as seen in Equation (2.6).

$$\rho V = F\rho^* V^* \tag{2.6}$$

where, $F = \frac{\delta^*/a}{\delta/a}$

Moeckel goes on to show that the parameter F can be determined strictly from the free stream Mach number. With F determined both the mass flow spillage and distance δ can be determined. Finally, he shows that the same factor F can be applied to a similar relationship for flow through a pitot tube. The authors of LAPIN extend this model for use in a supersonic inlet by creating a new correction factor F_C, that effectively scales the original F which can be seen in Equations (2.7) and (2.8). The parameters in Equation (2.8) are seen in Figure 2.13.

$$\rho V = F_C\rho^* V^* \tag{2.7}$$

$$F_C = F\left\{\left(\frac{2Y_C - a_L}{Y_C}\right)^j \left(\frac{a_L}{a_I}\right)\left[\frac{1 - \frac{\rho_I U_I}{\rho_L U_L}\left(\frac{2Y_C - a_I}{2Y_C - a_L}\right)^j \left(\frac{a_I}{a_L}\right)}{1 - \frac{\rho_I U_I}{\rho_L U_L}}\right]\right\} \tag{2.8}$$

This method is then used to determine not only the mass flux leakage but the momentum and energy flux leakage as well. The resulting model compared well to experimental data when modeling the unstart condition in mixed compression inlets where the normally ingested normal shock is expelled

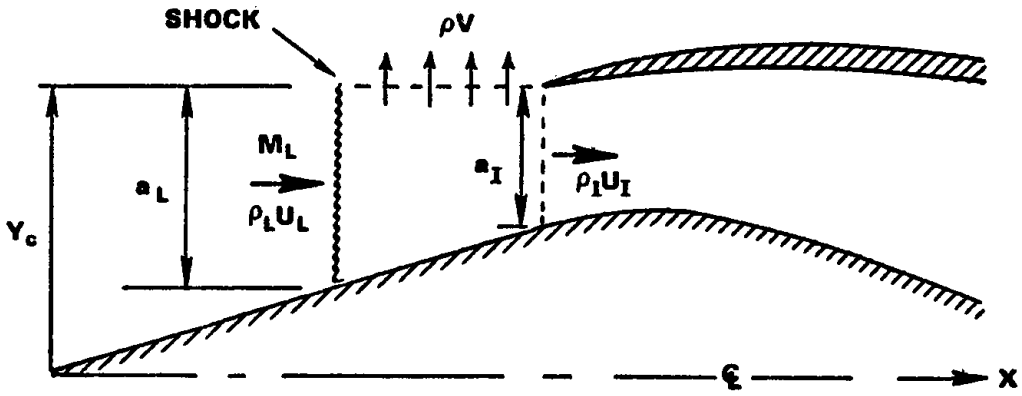

Figure 2.13: Mass spillage model for a supersonic inlet (Varner[57]).

from the inlet [57]. While this modification was intended to model a mixed compression inlet, the same physics in the cowl lip region are experienced by an external compression inlet at its design point, so the model is applicable.

Kopasakis, et. al. provide an alternative method for determining the mass flux leakage around the cowl lip in [34]. This method is based of off the assumed mass capture at the freestream and the experimentally determined mass flow demand at the compressor face. The mass flow leakage is then calculated as the difference between the two. The issue with this approach is that it requires *a priori* knowledge of the inlet's behavior and can therefore not be generalized to untested geometries. Additionally, this approach, while accurate for the steady state case, may not accurately simulate dynamic response of the inlet to perturbations. This is due to the fact that changes in mass flow demand and/or mass flow capture would be felt instantaneously at the cowl lip location. Likewise, changes in normal shock position caused by free stream perturbations would not effect the amount of mass flow spillage, which is unphysical. For these reasons, this type of modeling approach will not be used.

2.6 Internal Duct Modeling

After the flow undergoes external compression it enters the inlet at the cowl lip station. At this point conservations equations can be used to model the flow inside the inlet. The general Navier-Stokes equations can be simplified under the assumptions that the flow is quasi one dimensional, an ideal gas, inviscid, and has no external heat sources added to it. The flow can still vary in time and changes in area as a function of time are allowed as well. The resulting Euler equations will accurately model the internal portion of the inlet if there is very little boundary layer separation [12, 16].

The quasi 1-D Euler equations, along with the equation of state, are listed as Equations (2.9), (2.10), (2.11), and (2.12) which were taken from [5].

Continuity:

$$\frac{\partial}{\partial t}(\rho A) + \frac{\partial}{\partial x}(\rho A u_x) = 0 \tag{2.9}$$

Momentum:

$$\frac{\partial}{\partial t}(\rho A u_x) + \frac{\partial}{\partial x}\left(\rho A u_x^2\right) = -A\frac{\partial p}{\partial x} \tag{2.10}$$

Energy:

$$\frac{\partial}{\partial t}(\rho A E_{tot}) + \frac{\partial}{\partial x}(\rho A u_x H_{tot}) = -p\frac{\partial A}{\partial t} \tag{2.11}$$

where, $E_{tot} = c_v T + \frac{u_x^2}{2}$ and $H_{tot} = c_p T + \frac{u_x^2}{2}$

Equation of State:

$$P = \rho R T \tag{2.12}$$

The continuity, momentum, and energy equations can be expressed generally as equation (2.13):

$$\boldsymbol{U_{,t}} + \boldsymbol{F_{,x}} = \boldsymbol{S} \tag{2.13}$$

where, $\boldsymbol{U}$ is the flow state, $\boldsymbol{F}$ is the flux term and $\boldsymbol{S}$ is the source term for each equation.

These equations, while simplified, require a CFD method to solve them. Several methods exist for solving unsteady quasi-one dimensional flow [5, 57], but for the sake of brevity only one method of interest will be discussed in detail. MacCormack's technique has been a popular choice for solving unsteady quasi-one dimensional flow problems since it's inception. It's popularity is due to it ease of implementation and it's degree of accuracy for many flow problems. The technique is an explicit CFD method which utilizes a predictor-corrector step for the time integration and a central difference approximation for the spatial derivatives. As such, the method is second order accurate in both space and time [5]. The method is also able to handle transitions from supersonic to subsonic flow through a normal shock wave with the addition of artificial viscosity. Previous reduced order inlet models have used this method to model the internal compression portions of the inlet with much success [15, 34, 57]. In these models the method was able to match the steady-state and dynamic results of other more complicated quasi 1-D CFD models and experimental data very closely.

Another popular choice for solving unsteady quasi-one dimensional flow is the split characteristics method. This method is described in detail in the LAPIN report [57]. In the report, five separate CFD methods (MacCormack, Beam-Warming, Hybrid Beam-Warming, Split Flux, and Split Characteristics) were tested to model the internal duct flow of a supersonic inlet. The authors found that the split characteristic method produced high fidelity solutions, handled large perturbations such as hammershock transients correctly, and could run with the highest Courant number. While the method ran half as fast as the less accurate and robust MacCormack method, it ran between one and a half and twice as fast as the other methods while maintaining or exceeding their accuracy. A complete description of the Split Characteristics method is beyond the scope of this thesis, but the basic approach is to propagate information numerically in the same direction as physically predicted by characteristic theory. This is done by determining the characteristic directions as well as the compatibility equations from the eigenvalues of the system of equations at each nodal point. From there, a new set of equations are created and are solved separately using either forward or backward differences depending on their characteristic direction. A more complete description of the method can be found in the LAPIN report [57]. Originally, this method was considered for the model created with this research but it was found that the already developed MacCormack method compared well with higher fidelity CFD. Therefore, at this stage only the MacCormack method is used in the reduced order model but the split characteristics method should be considered in the future if limitations are found.

In contrast to these methods and others like them where the quasi 1-D Euler equations are solved, MacMartin has developed a reduced order model of a mixed compression supersonic inlet by focusing solely on the normal shock movement [40]. For mixed compression inlets, stability of the inlet is determined by the normal shock position. Mixed compression models are focused primarily on controlling normal shock movement so this is a valid approach. In his model, only internal duct flow is considered and a simplified ODE is developed to model the normal shock. Atmospheric disturbances are applied as perturbations to either acoustic or entropy waves to induce motion in the shock. MacMartin develops the ODE by combining the equation perturbation model with

normal shock relations and a linearized approximation of the pressure increase across the normal shock.

Additionally, MacMartin shows that disturbances that propagate through the duct can be modeled, on either side of the shock wave using Equations (2.14) and (2.15), and through the normal shock using Equation (2.16).

$$\tau^{\pm} = \int_{x_i}^{x_j} \frac{1}{c} \frac{1}{M \pm 1} dx, \qquad \tau^{e} = \int_{x_i}^{x_j} \frac{1}{cM} dx \tag{2.14}$$

$$\frac{\delta_j^{\pm}}{\delta_i^{\pm}} = \frac{M_i \pm 1}{M_j \pm 1} \left(\frac{M_j}{M_i} \right)^{\frac{1}{2}} \left\{ \frac{1 + \left[(\gamma - 1)/2 \right] M_j^2}{1 + \left[(\gamma - 1)/2 \right] M_i^2} \right\}^{\frac{1}{2}} \tag{2.15}$$

$$\delta_2^{+} = \sigma_2^{-} \delta_2^{-} + \sigma_1^{+} \delta_1^{+} + \sigma_1^{-} \delta_1^{-} + \sigma_1^{e} \delta_1^{e} \tag{2.16}$$

In Equation (2.15) the $\delta's$ are perturbation waves, c is the speed of sound, subscript j denotes a point downstream of a location represented by subscript i, subscripts 1 and 2 denote properties upstream and downstream of the shock wave, respectively, and superscripts +, -, and e denoted fast and slow acoustic waves and entropy waves, respectively. This equation relates the amplitude of a single acoustic wave at different points in the flow field that travel at a speed found using Equation (2.14). Entropy waves are convected at a constant amplitude with a propagation time found using the second equation in Equation (2.14). Equation (2.16) predicts the amplitude of the disturbance propagating downstream of the normal shock based on the upstream and downstream disturbances using reflection and transmission coefficients (σ). A more detailed explanation and derivation of these equations can be found in MacMartin [40]. The main feature of this work that is relatable to this research, is that a method is presented for properly modeling disturbance propagation in a reduced order model as a function of local flow variables. While this method will not be used to model the internal duct dynamics of the inlet, it will be used to help develop a more accurate external compression model.

2.7 Boundary Conditions

In addition to the flow solver used for the internal duct modeling, the choice of boundary conditions have an impact on the accuracy and stability of the simulation. For the upstream boundary condition, the flow is supersonic regardless of whether the domain extends past the cowl lip. The characteristics for supersonic flow propagate information downstream and as such, all of the state variables must be defined at the inflow boundary proscribed by the external compression model [5]. The outflow boundary on the other hand has only one characteristic coming from outside the domain and therefore one state variable must be defined. Common choices in the literature are Mach number, mass flow rate, and static pressure [5, 35, 57] with varying degrees of accuracy and stability. Kopasakis, for instance, reports stability issues with using mass flow rate [35]. Regardless of the choice of the boundary condition, the preferred method for determining the remain boundary conditions at the exit plane involves solving the flow along characteristic lines as detailed in [34, 57]. Pressure seems to be the most common choice though and according to Chima et. al [12], the results of an unsteady RANS simulation of a coupled axisymmetric-fan system confirm that this is a realistic boundary condition. In the simulation close to uniform static pressure was measured at the compressor face. Unless the flow separates upstream this behavior is predicted by the fact that static pressure is constant across boundary layers [36]. However, this

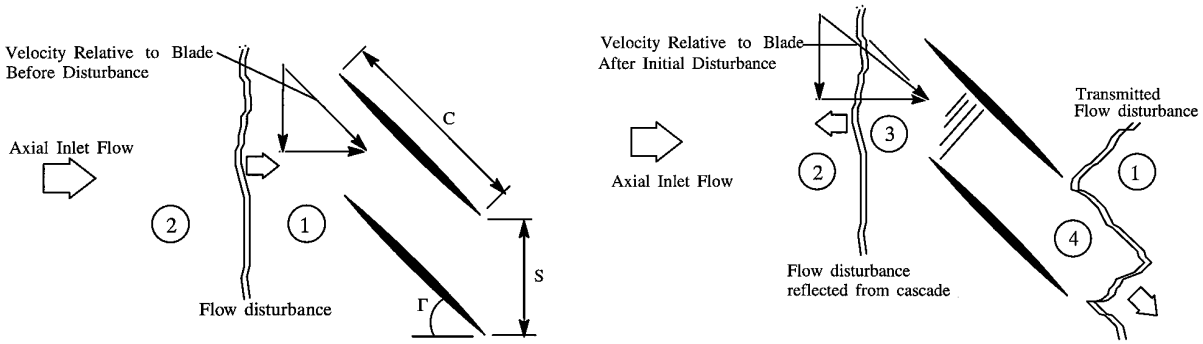

(a) Incoming disturbance before interacting with compressor fan

(b) Disturbance partially reflected and transmitted after interaction

Figure 2.14: Disturbance interaction with compressor fan (Paynter[45])

is only true of the steady state case where atmospheric disturbances are not being modeled. For unsteady simulations, more sophisticated boundary conditions are needed.

It has been shown separately by both Paynter et. al. [45] and Sajben et. al. [47] using a linearized theory of the conservation equations, that portions of a flow disturbance will be both reflected and transmitted by the compressor fan system(Figure 2.14). Both authors assume small planar perturbations and base there relations off of the upstream flow characteristics and the compressor blade geometry. These results were confirmed experimentally by Opalski et. al. [44] using a subsonic duct coupled with a single row compressor fan. In the experiment a wire spanning the duct was exploded creating two acoustic waves and an entropy wave that travel through the duct. The researchers measured the propagation of the waves as they intersected with the compressor fan and accurately measured the reflected and transmitted portions of the waves. In both the theoretically derived and experimentally obtained results, it was found that the traditional compressor face boundary conditions (constant pressure, velocity or Mach number) created reflections into the inlet that were much larger in magnitude than what should naturally occur. This is illustrated nicely by Paynter et. al. [45] in Figure 2.15. Here, the new compressor face boundary conditions were implemented in the code LAPIN and compared to experimental results as well as the results of using traditional boundary conditions. Figure 2.15 clearly shows that the modified boundary conditions better represent the physics of this disturbance interaction.

The method by Paynter et. al., is the most detailed and supported method found in the literature for applying inlet compressor boundary conditions in reduced order inlet models. The derivation is beyond the scope of this thesis so the following explanation is meant only to highlight the method. The authors start by assuming the flow state upstream of the compressor is known and the the compressor blades are flat plates of zero thickness. From there, they assume the disturbance is of a small amplitude and use a small-perturbation analysis along with isentropic relations to develop a system of equations to relate the flow properties in regions 1-4 seen in Figure 2.14. They then combine the equations though some algebraic manipulation to yield an expression for the reflection coefficient which is defined as the ratio of the reflected disturbance

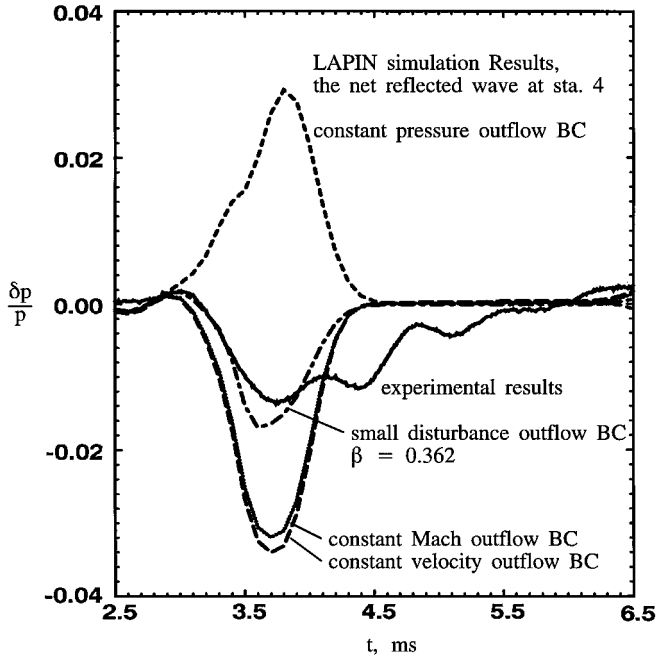

Figure 2.15: Compressor boundary condition comparison (Paynter[45]).

pressure change to the incident disturbance pressure change as seen in eqn (2.17).

$$R = tan^2\left(\frac{\Gamma}{2}\right)\left(\frac{1+M_{x1}}{1-M_{x1}}\right) \tag{2.17}$$

where, Γ is the blade stagger angle and M_{x1} is the upstream Mach number.

From here the authors linearize the Euler equations and use a characteristic approach to develop their boundary condition model. By determining what information should be propagated into and out of the domain and by making some assumptions related to their small disturbance analysis, they develop a set of boundary conditions using a reflection parameter β, that properly represent the compressor in a reduced order model. By setting β to the value of R developed in eqn (2.17), the proper boundary condition can be established. Furthermore, traditional boundary conditions of constant pressure or velocity can be modeled by setting β to -1 or 1 respectively. Nonreflecting boundary conditions can be obtained by setting β to 0.

2.8 Complete Inlet Models

In general, the literature presents two approaches to creating a total inlet model. Either several methods are put together to represent the different parts of the flow field in a piecewise fashion or a reduced order model is created from a linearized high fidelity CFD model. Of the 'piecewise models', most model 2-D mixed compression inlets and therefore model the external compression using oblique shock relations which are not applicable to conical flow fields [1, 17, 23, 35, 40]. Many did not apply atmospheric disturbances to verify the dynamics of the model [17, 23, 50, 52, 57]. Finally, almost none of the previous models have a subsonic mass spillage model for the cowl lip [1, 17, 23, 35, 40, 50, 52] or account for the dynamics of the external compression flow field [1, 17, 23, 35, 40, 50, 52, 57]. Of the current 'piecewise models' in existence, the work by Varner, et. al. [57] and Kopasakis, et. al [34, 35], are most closely related to the proposed research. The main improvement over these works will be a more complete and accurate modeling of the external compression field and the added capability to simulate changes in angle of attack. A summary of the state of the art 'piecewise models' and their features can be seen in Figure 2.16. Here, cells in green represent methods that correctly represent the physics of an external compression inlet, where cells in red resent methods that may have worked for a different type of inlet or problem but are not applicable to the research in this proposal. Cells with a red 'X' signify that the paper does not have the capability to model the region of the flow field seen in the associated column title.

The second common method for creating a reduced order supersonic inlet model involve higher fidelity CFD and mathematical model reduction [10, 21, 37, 60]. In these models a high fidelity CFD code is used to obtain a single or many steady state solution(s) to the overall flow field. The model is then linearized about this point and projected onto a lower dimensional space characterized by set of basis vectors using a model reduction technique such as Arnoldi [37, 60] or modified square root reduction [10]. Dynamic simulations are created by slightly perturbing the reduced order model. Although these model have produced excellent results when compared to the respective higher order CFD model they are derived from, they do not handle large perturbations

Paper Title	Author(s)	Atmospheric/ Perturbation Model	External Compression Type	External Compression Model	Cowl Lip Spillage Model	Internal Duct Model(s)	Boundary Conditions
Dynamic Characterization and Active Control of Unstarts in a Near Isentropic Supersoic Inlet	U. Ashun	Applied as acoustic waves	X	X	X	Quasi 1-D and Euler based 2-D CFD	Traditional
Reduced Order Models of 2D Supersonic Flow with Applications to Scramjet Inlets	D. Dalle, M. Fotia, and J. Driscoll	X	2-D/ Mixed Compression	X	Supersonic spillage only	Steady state "wave interaction"	Supersonic outflow only
Supersonic Inlet Dynamics Model Based on Equilibrium Manifold	B. He, J. Chang, W. Bao, and D. Yu	X	2-D/ Mixed Compression	X	X	MacCormack's Method	Traditional
Quasi 1D Modeling of Mixed Compression Supersonic Inlets	G. Kopasakis, J. Connolly, D. Paxson, and K. Woolwine	Kopasakis Model	2-D/ Mixed Compression	Oblique shocks/ no dynamic model	Supersonic spillage only	Quasi 1-D CFD	Traditional
Quasi One-Dimensional Unsteady Modeling of External Compression Supersonic Inlets	G. Kopasakis, J. Connolly, and J. Kratz	Kopasakis Model	Axisymmetric/ External Compression	Oblique shocks/ simple time delay dynamic model	Based off engine mass flow	MacCormack's Method	Traditional
Dynamics and Control of Shock Motion in a Near-Isentropic Inlet	D. MacMartin	Applied as acoustic waves	2-D/ Mixed Compression	X	X	Linearized Equations	Uses reflection/transmission coeffs.
Design and Analysis Tool for External-Compression Supersonic Inlets	J. Slater	X	All types	Method of chars./ no dynamic model	Unclear	Analytical steady state equations	Traditional
Computer Program for Calculating Flow Fields in Supersonic Inlets	V. Sorensen	X	Axisymmetric, 2-D/ Mixed Compression	Method of chars./ no dynamic model	Supersonic spillage only	Method of chars./supersonic portion only	Supersonic outflow only
Large Perturbation Flow Field Analysis and Simulation for Supersonic Inlets	M. Varner, W. Martindale, W. Phares, K. Kneile, and J.C. Adams	Mach number disturbance	Axisymmetric, 2-D/ Mixed Compression	Custom model/ no dynamic model	Yes	4 Quasi 1-D CFD models	Uses reflection/transmission coeffs.

Figure 2.16: Summary of current inlet models.

such as shock movement. Additionally, one of the main goals of this research is to develop the model in simulink. The mathematical complexity of these methods may make it difficult or impossible to implement in the Simulink environment, which may be unnecessary if a robust and simpler model may be used. Finally, recent work by Farhat et. al. [2, 9, 38, 39] has taken this approach and modified to be accurate over a larger range for nonlinear systems. His work, while focused mostly on aero-elastic models, would be applicable to modeling supersonic inlets as it is a less complex system than the method is already proven to work for. His method does not suffer the drawbacks associated with linearizing the N.S. equations but would still be difficult to reproduce in Simulink due to its complexity.

2.9 High Fidelity CFD Verification

An additional large component of this research, is to verify the lower order inlet model using a high fidelity CFD code. The CFD code PHASTA has been chosen as that verification tool. PHASTA is a good choice for verification not only for its proven accuracy and efficiency but also for it ability to solve complex turbulent flow fields. Although the current simulations employ the

Euler equations and using such a powerful CFD solver may seem overkill, a higher fidelity model may be needed in the future to study the effects of turbulence and boundary layer separation in the model. Using PHASTA would remove the uncertainty involved in switching models if a different verification tool had been used for the 3D inviscid model.

PHASTA is a parallel, hierarchic (2nd to 5th order accurate), adaptive, stabilized (finite-element) transient analysis tool for the solution of compressible or incompressible flows. PHASTA (and its predecessor ENSA) was the first massively parallel unstructured grid LES/DNS code [25, 26, 28] and has been applied to flows ranging from verification benchmarks to cases of practical interest. The practical cases of interest not only involve complicated geometries (such as detailed aerospace configurations or human arterial system) but also complex physics (such as fluid turbulence or multi-phase interactions).

In PHASTA, flow computations are performed using a stabilized, semi-discrete finite element method for the transient, compressible or incompressible Navier-Stokes partial differential equation (PDE) governing fluid flows. In particular, PHASTA employs the streamline upwind/Petrov-Galerkin (SUPG) stabilization method introduced in [8] to discretize the governing equations. The stabilized finite element formulation currently utilized has been shown to be robust, accurate and stable on a variety of flow problems (see for example [55, 58]). In the flow solver (PHASTA), the Navier-Stokes equations (conservation of mass, momentum and energy) plus any auxiliary equations (as needed for turbulence models or level sets in two-phase flow) are discretized in space and time. The discretization in space based on a stabilized finite element method leads to a weak form of the governing equations, where the solution (and weight function) are first interpolated using hierarchic, piecewise polynomials [58, 59], and followed by the computation of integrals appearing in the weak form using Gauss quadrature. Implicit integration in time is then performed using a generalized-α method [27] which is second- order accurate and provides precise control of the temporal damping to reproduce Gear's Method, Midpoint Rule, or any blend in between. On a given time step, the resulting non-linear algebraic equations are linearized to yield a system of equations which are solved using iterative procedures. For the current stage of research, the following Euler

equations are being solved by PHASTA.

Continuity:

$$\rho_{,t} + [\rho u_i]_{,i} = 0 \tag{2.18}$$

Momentum:

$$[\rho u_j]_{,t} + [\rho u_i u_j]_{,i} = -P_{,j} \tag{2.19}$$

Energy:

$$[\rho e_{tot}]_{,t} + [\rho u_i e_{tot}]_{,i} = -[u_i P]_{,i} \tag{2.20}$$

where, $e_{tot} = e + u_i u_i/2 = CpT + u_i u_i/2$

2.10 1D Model Overview

As mentioned the main research goal of this proposal is to develop a quasi 1-D model of an external compression inlet that can be implemented easily in Matlab/Simulink. The model needs to be constructed in the Matlab/Simulink environment using either Simulink blocks or S-functions so that it can be incorporated with a larger AeroPropulsoServoElastic model. The implementation in Simulink should be general enough to handle multiple geometries and robust enough to be modified with additional features in the future if necessary (i.e. mass sources and sinks for flow control). The model must be able to handle changes in free stream perturbations as well as perturbations coming from the engine(compressor surge, etc.). While the perturbations applied to the model will mostly likely be small, the engine must be able to handle large nonlinear changes in the flow field, namely shock movement and mass flow spillage at the cowl lip. Finally, the model must simulate this inherently 3-D flow field as efficiently possible.

Modeling the inlet can be broken up into five main components (Figure 2.17), the atmospheric model, the external compression region, the cowl lip spillage, the internal duct and the exit boundary conditions. In Section 2.2 it was shown that there exists two common methods for applying atmospheric perturbations. One model developed by Ashun [1], applies perturbations as either acoustic or entropy waves using a combination of perturbations to the flow variables. The

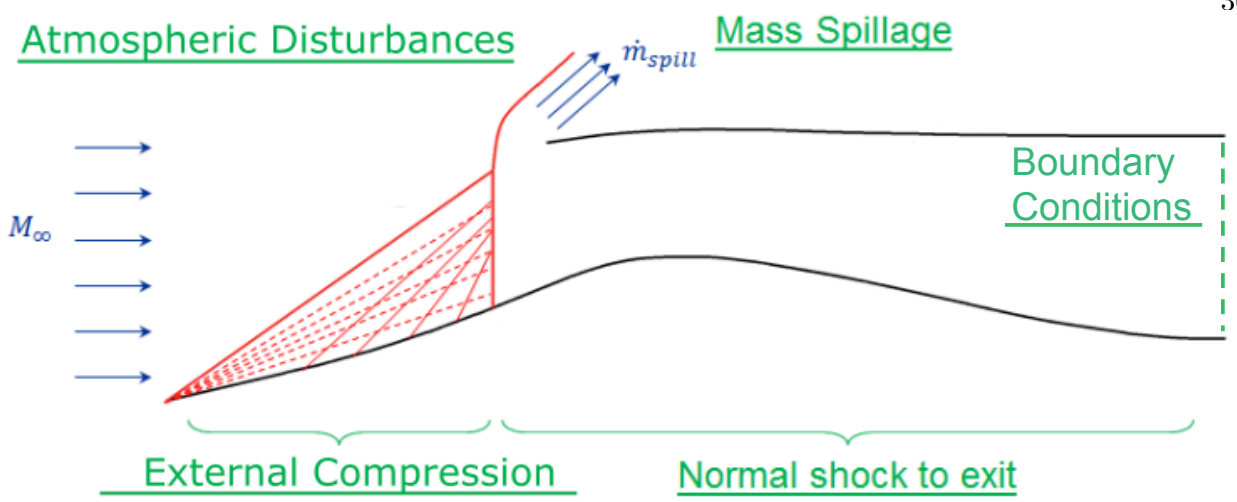

Figure 2.17: Inlet modeling techniques

other, developed by Kopasakis [31, 32], applies the perturbations to the flow variables individually. As shown, both methods are valid for either characterizing the dynamic behavior of a model or developing control algorithms. The researchers at NASA Glenn who are developing the rest of the propulsion model use the latter method developed by Kopasakis. For this reason, his model will be used in characterizing the dynamics of both the reduced order and high fidelity inlet models.

The next region is the external compression portion of the inlet, which consists generally of a single conical shock followed by isentropic compression (as is the case with the model used in this research) or as a series of conical shocks (as is the case with simpler models). This portion of the flow field is modeled using a combination of the solution to the Taylor-Maccoll equations and the method of characteristics. These methods are modified in a novel way to account for atmospheric perturbations. The cowl lip mass flux spillage region as well as the location of the normal shock will be modeled in two separate ways, first using the method developed in the LAPIN report [57] and then using new approach that makes use of PHASTA simulations. The merits of both approaches are compared. The internal duct portion will be modeled using previously developed methods from

Kopasakis [34, 35] that solves the quasi 1D equations using the MacCormack method. Finally, the compressor face exit boundary condition will be modeled using the procedure described in Section 2.7. This model ensures that the proper information is being reflected and transmitted as was shown to be the case experimentally

Chapter 3

High Fidelity Simulations

The supersonic transport vehicle and inlet model being used for this research is still in the design phase and therefore no experimental data exists for this inlet. As such, using PHASTA to as verification device was crucial in the development of the 1D model. This was true both for verifying the results of the 1D model and, as will be seen in subsequent chapters, in the development of certain capabilities that would otherwise be impossible. Next the results from the PHASTA simulations are presented. First the results of a few calibration tests are presented, followed by the steady state and dynamic results of the total inlet. These results were verified at all three operating conditions (sub-critical, critical, and super-critical). The PHASTA results were obtained using the full 3D model as well as a quasi 2D model. These results will be followed by the results of simulations run just using the external compression portion of the inlet.

3.1 PHASTA Calibration Tests

As mentioned in Section 2.9, PHASTA is a proven high fidelity CFD solver shown to accurately model a wide range of flow regimes. PHASTA is also a robust tool with a wide range of flow solver settings that allow it to optimize both speed and accuracy. For these reasons it is necessary to run test cases to ensure not only that the results match theoretical predictions for the flow regimes relevant to this research but that the correct flow solver attributes are set to achieve accurate results. In order to accomplish this, three test cases were devised which together make up the relevant flow features of the simulations to be run on the total inlet model. The first test cases

assess PHASTA's ability to capture normal shocks. This test determines not only the proper shock location but all the jump in flow states across a normal shock as well. The second test determines PHASTA's capability to simulate a conical shock field. This is relevant to the external compression portion of the inlet. The final test case consists of a simple 1D duct with constant area. This test case was used to track speed and amplitude of perturbations as they travel through a flow field as compared to theoretical predictions. The test was also used to determine the affects of time integration and discontinuity capturing settings as well. In all three test cases the results matched theoretical predictions with very little error.

The first step in verifying PHASTA's ability to simulate supersonic flows is the ability to capture normal shockwaves. This test involved creating a simple expanding duct. Supersonic inflow conditions were applied for the velocity, pressure and temperature and a subsonic back pressure was applied that would cause a normal shockwave to form close to the middle of the duct. The value of the back pressure was predicted using quasi 1-D compressible flow equations which can be found in Anderson [5]. Initial attempts failed in acquiring a stable solution when attempting to start from supersonic initial conditions. Compressible flows require care in the setting of initial conditions if one is to avoid generating spurious waves that may take a very long time to decay. It was observed that the fastest convergence to steady state was achieved by initializing the flow to linearly vary between inflow and outflow conditions.. In this simulation velocity, pressure and temperature were initialized based on the quasi 1-D predictions of the inflow and predicted outflow. Using this method and applying PHASTA's discontinuity capturing feature, the predicted quasi 1-D results were obtained.

Figure 3.1 shows the Mach number variation in a cross sectional slice of the duct. It should be noted that PHASTA is correctly capturing the 3-D features of the flow not present in the quasi 1-D prediction, i.e. the expansion waves before the normal shock wave. The expansion waves cause the flow properties to oscillate about the predicted values, which are smooth in the quasi 1-D prediction. This can be seen in Figures 3.2(a) and 3.2(b), which display the Mach number and non-dimensional pressure variation along the center of the duct respectively. The pressure variation

matches the predicted values almost exactly after the normal shock wave. The Mach number also matches closely but has some constant error after the shock.

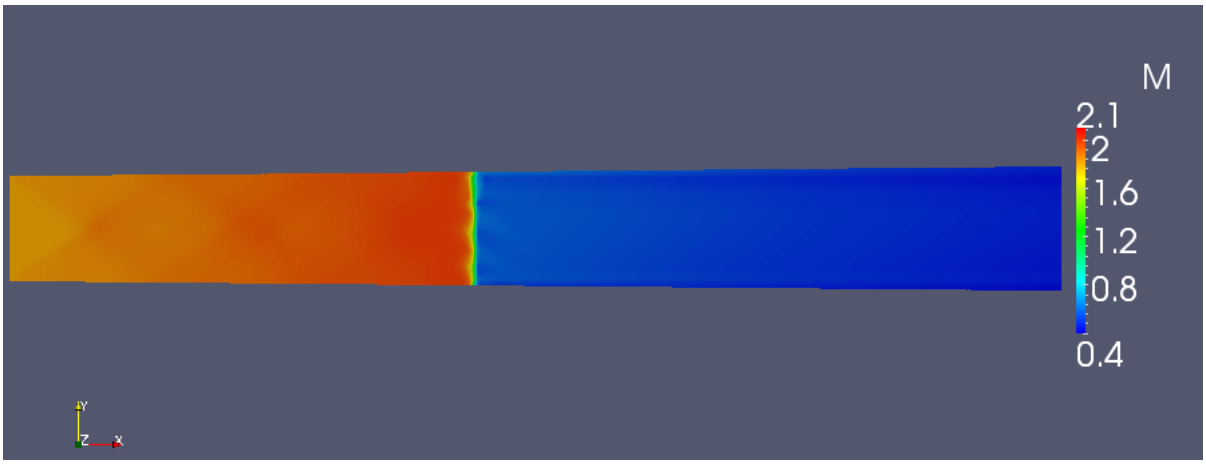

Figure 3.1: Mach Number Variation From PHASTA

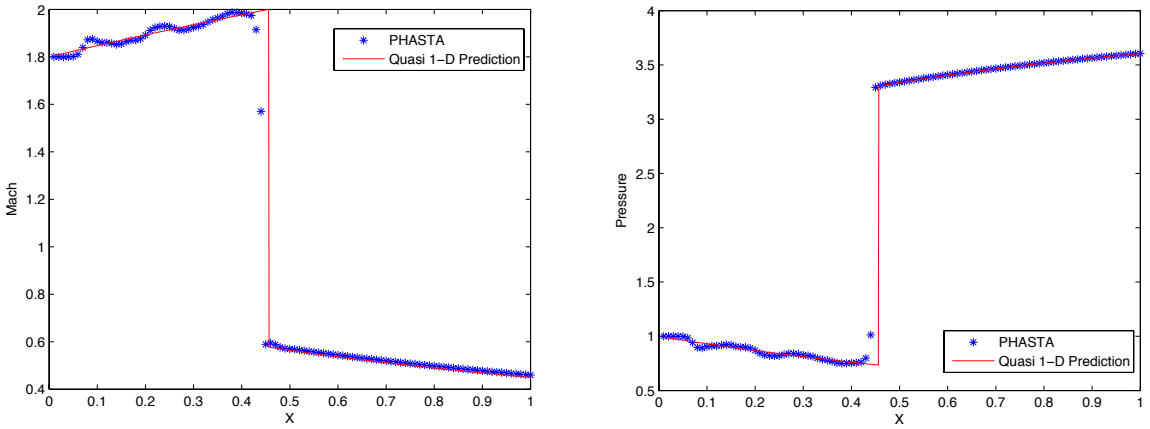

(a) Mach number

(b) Non-dimensional Pressure

Figure 3.2: PHASTA results compared to compressible flow theory

The second test was to verify PHASTA's ability to model conical shock waves correctly. For this test, the first third of the centerbody of the inlet being studied was analyzed (Figure 3.3(a)). The conical centerbody has an initial angle of 15 degrees followed by smooth transition to a final angle of 25 degrees. Supersonic inflow conditions were applied for the pressure, velocity, and temperature, based off of relevant flight conditions with a freestream Mach number of 1.8 at an altitude

of 50,000 ft. The simulation was inviscid, and no outflow conditions were applied. Figure 3.3(b) shows the results of the PHASTA simulation, which displays the Mach number variation past the cone. This test used a fairly coarse mesh, which accounts for the fuzziness of the conical shock wave location.

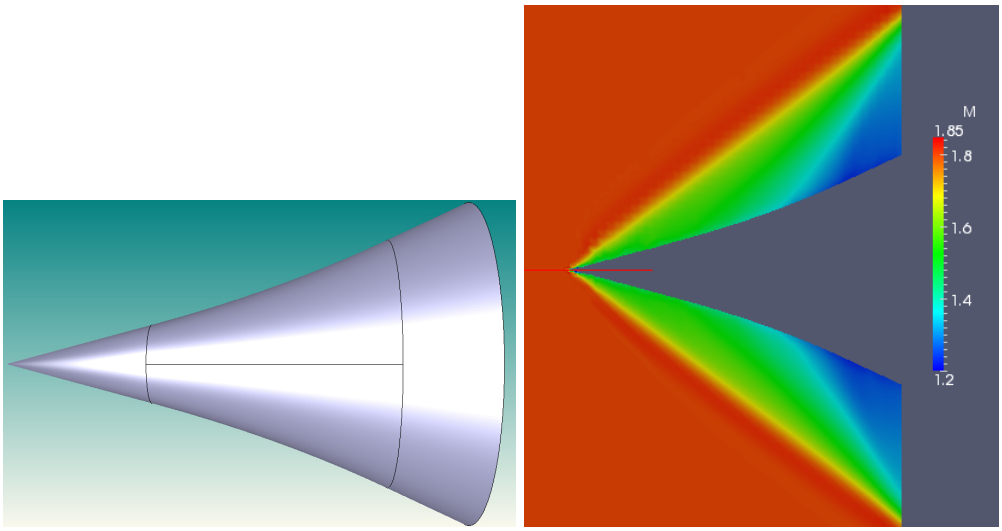

(a) Geomtery (b) Mach number variation

Figure 3.3: External compression section of the inlet

In order to validate the results of this simulation, the Taylor-Maccoll equations were solved. As mentioned in Section 2.3, the solution to these equations is exact for flow around a semi-infinite cone. To accomplish this, a function was written in MATLAB which solves these equations to a specified tolerance.For this comparison, the region just behind the first conical shock emanating from the initial flow deflection angle was chosen. Table 3.1 displays this comparison where it can be seen that the flow variables from PHASTA match the predicted values very closely. It should be noted that values from other regions of the flow were compared and showed similar precision.

The final test case was created to assess PHASTA's ability to propagate small amplitude disturbances with little to no artificial damping or phase lag. The test geometry consisted of a straight, thin pipe with a square cross section and no change in cross sectional area or essentially, a 1D duct. Two tests were performed on this geometry that included a step change in pressure

Table 3.1: Supersonic Conical Flow Field

	Taylor - Maccoll Solution	**PHASTA**	**% Difference**
Shock Angle	37.30°	37.05°	0.670
Mach Number	1.659	1.646	0.784
$P_{t2}/P_{t\infty}$	0.998	0.997	0.100
P_2/P_∞	1.244	1.259	1.206
T_2/T_∞	1.064	1.066	0.188

applied at the inflow plane and a sinusoidal change in pressure applied at the inflow plane. In order to accomplish these tests the time integrator function in PHASTA was altered to call the new function before every time step. The new function then scanned all of the surface nodes of the model. Nodes on the inflow boundary that were tagged with an ID number during pre-processing were then updated with the pressure perturbation as a function of time.

Once the ability of the new function was confirmed, the 1-D test case was used to optimize PHASTA's settings for unsteady simulations. Specifically, this model was used to determine the effect of the mesh size, time step, and discontinuity capturing feature. These test cases were performed using a second order accurate time integrator. The first test was performed by altering the mesh size and time step. Table 3.2 details the list of trials that were run. For these tests a sinusoidal pressure wave was prescribed at the inflow with an amplitude of 100 Pa and a frequency of 1000 Hz. The results of this test were analyzed by looking at the CFL number and the non-dimensional wavenumber. The CFL number is a measure of how well the physics of the flow are being represented. The Courant number should be less than 1 for this reason. If its greater than 1, the simulation is propogating the solution faster than the flow can physically respond(Ref Singer CFD PDF). Additionally, the non-dimensional wave number kh determines how well a sinusoidal disturbance is resolved. According to Hughes [19] a non-dimensional wave number less than 0.6 is desired to decrease the amount of damping and phase lag in the simulation. The results of these tests are seen in Figures 3.4(a) and 3.4(b), where Figure 3.4(b) shows a close up of one of the peaks. From these figures it is clear that the simulations with a non- dimensional wave number more than

0.6 have considerable damping (plots in red) and was the greatest determination for error. The rest of the simulations had acceptable amounts of error and for computational time consideration, a time step of $\Delta t = 1e-5(s)$ and grid size of $\Delta x = h/2 = 0.0125(m)$ were chosen as the optimal combination for the remaining simulations.

Table 3.2: Time Step and Mesh Size Tests

Mesh Size *(h = 0.025m)*	h	h	h	h/2	h/2	h/2	h/4	h/4	h/4
Time Step (s)	1e-05	5e-06	1e-06	1e-05	5e-06	1e-06	1e-05	5e-06	1e-06
$\mathbf{Cr = (u + c)\frac{\Delta t}{\Delta x}}$	0.33	0.17	0.03	0.66	0.33	0.07	1.32	0.66	0.13
$\boldsymbol{kh = h\frac{2\pi}{\lambda}}$	0.66	0.66	0.66	0.33	0.33	0.33	0.17	0.17	0.17

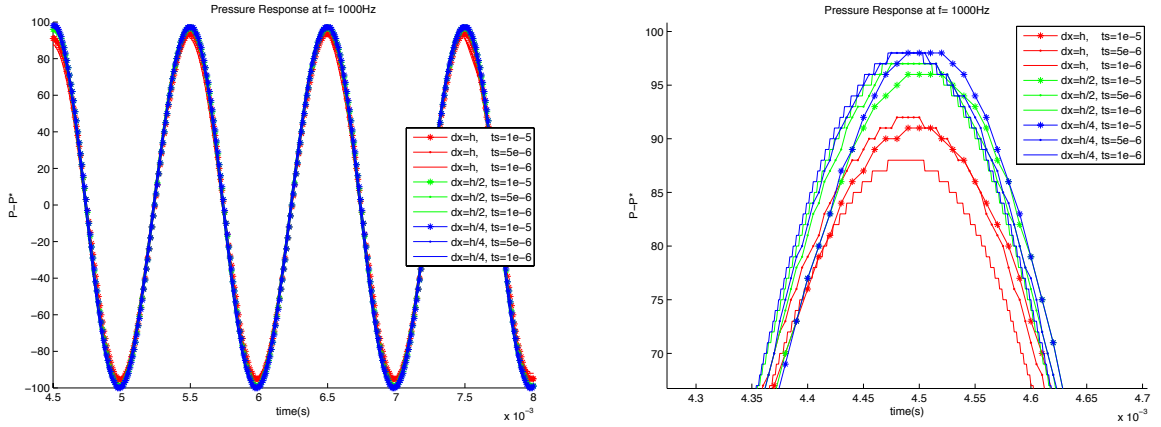

(a) Pressure response with initial condition subtracted

(b) Focus on a single peak

Figure 3.4: Pressure Response in 1D Duct comparing time step and mesh size

A second test was performed to determine the effect that the discontinuity capturing feature has on the accuracy of the unsteady results. In PHASTA there are three types of discontinuity capturing features; DC- Mallet, DC-Quadratic, and DC-minimum. Each is implemented by adding an extra term to the SUPG method but with varying strengths. These features are crucial in obtaining a stable solution when shock waves are present. As such, one of these features must be

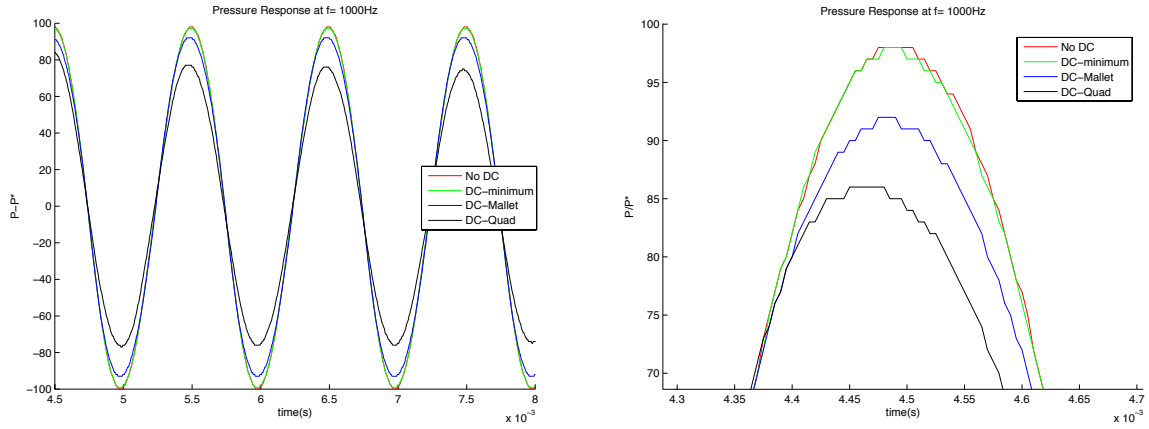

(a) Pressure response with initial condition subtracted

(b) Focus on a single peak

Figure 3.5: Pressure Response in 1D Duct comparing discontinuity capturing settings

used for the actual inlet simulations. In the test case the same perturbation was added to the inflow plane as the previous tests using a time step of $\Delta t = 1e-5(s)$ and mesh size of $\Delta x = 0.0125(m)$. This test was run with each of the discontinuity capturing features and was compared to the base run without this feature on. Again, a 100 Pa amplitude, 1000Hz sinusoidal perturbation was applied at the inflow boundary condition. Figures 3.5(a) and 3.5(b) show the results of this test which clearly illustrate that the DC-minimum feature should be used to avoid excessive damping of the perturbation.

The final test compares PHASTA's ability to propagate small amplitude disturbances to those predicted by theory. In this test the same simple 1D duct was used to analyze a Riemann problem as described in Knight [29]. The Riemann problem is an initial value problem in which two flow states are separated by a partition or diaphragm as seen in Figure 3.6. At time zero the diaphragm is burst and the flow finds a new equilibrium as two characteristic waves and a contact surface wave (or equivalently, a fast acoustic, slow acoustic, and entropy wave) move through the flow field at $u + c$, $u - c$, and u respectively (Figure 3.7). Here u is the local velocity and c is the speed of sound. The amplitude of flow variables of the waves can be predicted by solving the Riemann problem as described in Knight. In PHASTA, this problem was set up for the 1D duct case by placing the imaginary diaphragm at the inflow boundary condition. The solution

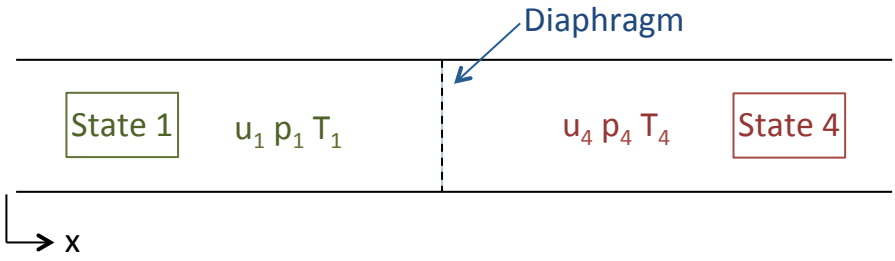

Figure 3.6: Riemann Problem at t = 0 (Knight [29])

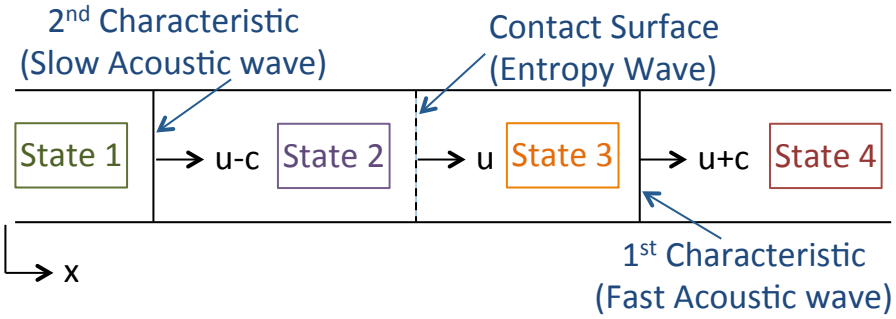

Figure 3.7: Riemann Problem at t > 0

was run using the optimized settings described previously. Table 3.3 compares the speeds of the disturbance waves and associated jumps in pressure from the PHASTA results with that predicted by the solution to the Riemann problem. From this table it can be seen that PHASTA accurately models both the speed of the disturbance waves as well as the jump in flow states. Note that the contact surface wave (or entropy wave) does not cause a jump in pressure although it does cause jumps in temperature and density.

Table 3.3: Riemann Problem Results

	P_1 (Pa)	P_2 (Pa)	P_3 (Pa)	P_4 (Pa)	δ^+ (m/s)	δ^e (m/s)	δ^- (m/s)
Riemann Problem Solution	11697	11647	11647	11597	826.1	531.1	236.0
PHASTA Solution	11697	11646.9	11646.9	11597	822.4	531.9	238.1
Percent Difference	0.000	0.001	0.001	0.000	0.448	0.151	0.890

From these results, we see that a change in single flow variable causes three disturbance waves

to propagate through the flow field. An alternative method for representing this phenomenon is detailed by MacMartin [40] and was briefly mentioned in Section 2.6. In MacMartin, non-dimensional perturbations to the flow variables (u, P, T, and/or ρ) are converted to equivalent fast acoustic (δ^+), slow acoustic (δ^-), and entropy (δ^e) wave disturbances using the conversion matrix in Equation (3.1). These disturbance waves propagate through a general 1D flow at $u + c$, $u - c$, and u respectively. The propagation delay of each wave at any point in the flow field can be found using Equations (2.14) in Section 2.6. At any point, the flow properties in between the waves can be found by converting a single disturbance wave to equivalent flow field perturbations using the conversion matrix in Equation (3.2). Representing flow variable perturbations this way was found to be the most convenient method and is how disturbances will be represented throughout the rest of the paper.

$$\begin{bmatrix} 2\delta^+ \\ 2\delta^- \\ \delta^e \end{bmatrix} = \begin{bmatrix} 1 & \gamma M & 0 \\ 1 & -\gamma M & 0 \\ -1/\gamma & 0 & 1 \end{bmatrix} \begin{bmatrix} \frac{\delta p}{p} \\ \frac{\delta u}{u} \\ \frac{\delta \rho}{\rho} \end{bmatrix} \tag{3.1}$$

$$\begin{bmatrix} \left(\frac{\delta p}{p}\right) \\ \gamma M \left(\frac{\delta u}{u}\right) \\ \gamma \left(\frac{\delta \rho}{\rho}\right) \\ \gamma (\delta M) \end{bmatrix} = \begin{bmatrix} 1 & 1 & 0 \\ 1 & -1 & 0 \\ 1 & 1 & \gamma \\ M^- & -M^+ & \gamma M/2 \end{bmatrix} \begin{bmatrix} \delta^+ \\ \delta^- \\ \delta^e \end{bmatrix} \tag{3.2}$$

Before moving on to the steady state and dynamics PHASTA results for the actual inlet model, it is necessary to discuss the results of these test cases in one more context as they explain a more complex behavior seen in inlet model. Most notably, in the external compression flow field of

the inlet. In the previous discussion, two types of tests were applied to the 1D duct flow case. The first applied a 100 Pa amplitude, 1000 Hz sinusoidal pressure disturbance and the second applied a single 100 Pa pressure step, both to the inflow boundary condition. These tests can be visualized at the same time step during each simulation in Figure 3.8, and are labeled 'Test a', and 'Test b' respectively. 'Test b' clearly moves through the flow field as two pressure jumps. Likewise, when these two tests are presented side by side it can be seen that the sinusoidal pressure disturbance test also moves as two pressure waves ,albeit sinusoidally varying ones. It can be seen that in the region where just the first characteristic (fast acoustic wave) has moved through the flow field there is a simple sine wave. Conversely, in the region where the second characteristic wave(slow acoustic wave) has traveled there is a complex interaction of the two disturbances. In other words at a given point in the flow field the interaction between the two overlapping is both unique and predictable. More generally, the response at any given point is the response of three waves, including the entropy wave, as mentioned before. For ease of presentation, pressure was reported here because it is only affected by two of the three disturbance waves and is thus easier to visualize.

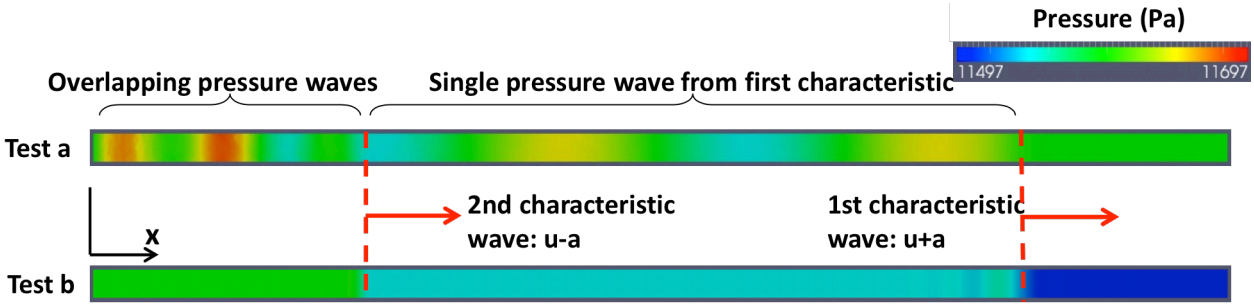

Figure 3.8: 1-D test example

"Test a" from Figure 3.8 was repeated at discrete frequencies between 100 and 1000 Hz. The response was measured at a distance of 1m from the inflow plane and the resulting max amplitude was recorded. As mentioned before the pressure response to these disturbances can be modeled simply as the overlapping of two equal amplitude pressure waves. Eqn. (3.3) below is the simplified version of two sinusoidal waves, with equal amplitudes A and propagation speeds of $u+a$ and $u-a$

respectively, added together.

$$P = A * cos\left(\pi f\left(\frac{x}{u-c} - \frac{x}{u+c}\right)\right) * sin\left(\pi f\left(2t - \frac{x}{u+c} - \frac{x}{u-c}\right)\right) \tag{3.3}$$

From Equation (3.3) it is clear that the resulting max amplitude at location x is simply the combination of the applied perturbation amplitude A and the cosine term. Figure 3.9 displays both the results of the discrete frequency pressure perturbation tests and the predicted amplitudes using Equation (3.3). The Bode plot in Figure 3.9 was created by taking the ratio of measured perturbation amplitude to the applied amplitude for both the test case and predicted value from Equation (3.3). As can be seen, the equation perfectly predicts the response of the test case at each frequency in both magnitude and phase.

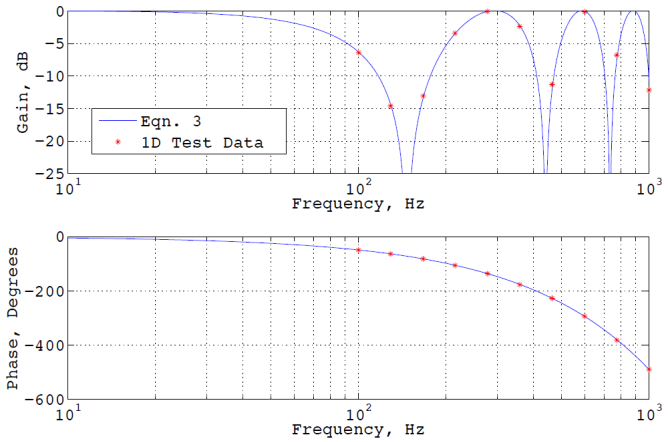

Figure 3.9: Bode plot of 1-D test example

The behavior seen in Figure 3.9 can be expected whenever a sinusoidal flow variable perturbation is applied to supersonic flow. Namely, that based on both location, flow state and frequency of disturbance, different points in the flow field will have wildly different responses. For the purposes of this research, these types of disturbances will be applied to the freestream, and as such, the response of the external compression flow field will respond with a similar behavior. These results show that a more sophisticated disturbance propagation model is needed for the external

compression flow field than what was previously employed in Kopasakis [34]. This will become more apparent in the ensuing 1D Model section.

3.2 Steady State PHASTA Results

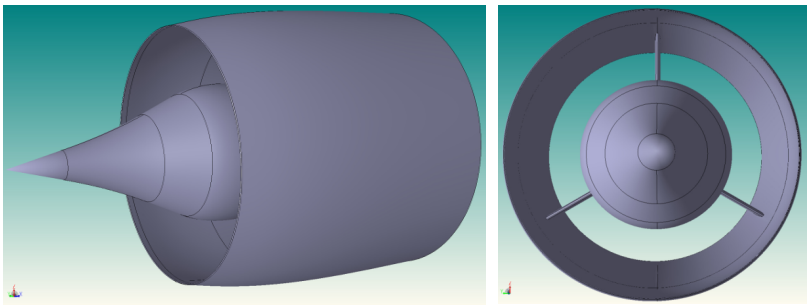

(a) 3-D View (b) Y-Z Plane

Figure 3.10: 3D Inlet Model

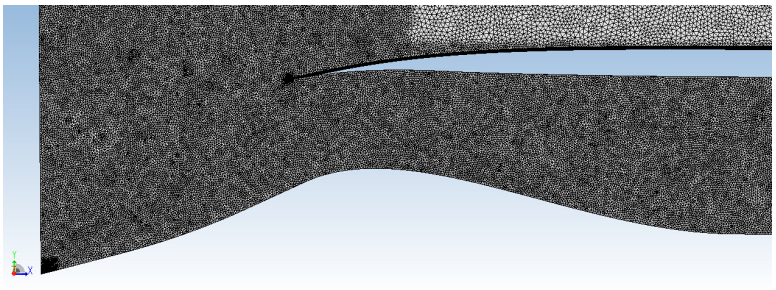

Figure 3.11: Meshed Fluid Domain of 2D Model (X-Y Plane of the 3D Model)

In PHASTA, two models were created, a 3-D model(Figure 3.10) and a 2-D model (Figure 3.11). The 2-D model is a 10° section of the Y-Z plane in the 3D model. PHASTA is strictly a 3D flow solver so the domain still has three dimensions but the flow is restricted to streamwise and radial directions. This was done to help understand what order of fidelity was needed for different simulations. The thought being that a 3-D model was probably not needed for free stream disturbances and the 2-D model would suffice. This would cut down on unnecessary computational expense and allow for more trial to be run. Conversely, cases involving changes in angle of attack would most likely necessitate a 3-D model but running 2-D model would help determine what dy-

namics might be missing from the future Simulink model and help facilitate potential correction factors if needed. So far both models have been confirmed against a previous GE model to provide the correct steady state results.

All steady state results were obtained using the optimized setting determined in the previous section. However the mesh size of dx = 0.0125m is only true of the bulk flow. Two areas employed mesh refinement due to better resolve the local flow structure. As can be seem in Figure 3.11, the regions at the centerbody tip and the cowl lip were refined by a factor of ten. This was done to help resolve the sudden change in flow direction in each area. Additionally, an extra 3m of straight duct was added to the internal duct portion of the inlet with a mesh that slow transition to approximate 30 times coarser. This was done to artificially dampen solution noise that exists between the normal shock and the exit plane. Without the this extra length, numerical perturbations can reflect off the exit plane and persist in this region, causing longer convergence times and potential error in dynamic results. This mesh was used for all of the 2D for all 2D simulations. The same mesh sizes were revolved to produce the mesh used in the 3D simulations (36 times larger mesh).

Likewise, all of the 2D and 3D simulations used the same boundary and initial conditions. For the current research only the cruise condition was considered and as such, the flow was supersonic in the free stream and subsonic at the exit of the inlet's internal duct. For these conditions it is necessary to specify the entire flow state at the upstream boundary condition because the Navier-Stokes equations have a hyperbolic mathematical form. Static pressure was used as the sole exit boundary condition within the inlet as it was shown in Section 2.7 to be an accurate choice. All surfaces, as well as the slip planes used to 'cut' the 3D model and create the 2D model, were treated as slip surfaces to adhere to the inviscid flow assumption. For the initial conditions, the free stream variables were used in all regions external to the inlet and in the internal duct region, the flow states were varied linearly from the free stream to he exit BC following the strategy from the normal shock test case in the previous section. The boundary conditions and initial conditions are summarized in Table 3.4.

The first steady state tests were used to compare PHASTA's results with simulations run by

Table 3.4: Boundary Conditions Used for PHASTA Inlet Simulations

Boundary Type	**Boundary Condition**
Inflow	$P_\infty, T_\infty, and\ V_\infty$
Supersonic Outflow	None
Subsonic Outflow	$P = P_B$
Walls and Slip Planes	$\vec{V} \cdot \vec{n} = 0, \partial T/\partial x_n = 0$

GE using the supercritical operating condition ($P_B = 45,930\ Pa$) at the cruise altitude ($M_\infty = 1.7$, h=15.24 km). The results of the 3-D model represented in the x-z plane are shown in Figure 3.12(a). This figure illustrates the complicated flow field consisting of shocks, isentropic compression waves, and expansion waves upstream of the normal shock. Using these results, the outflow conditions of the inlet were measured by finding the integral averaged state at the exit plane ($P_2, M_2\ and\ \dot{m}$). The outflow conditions of the 2-D model were obtained using the same technique. These results were compared to those obtained by General Electric (GE) and are shown in Figure 3.12(b). As can be seen in this Table, both models match the GE model very closely, showing less than 1% error in the flow variables of interest. Based on these results, the PHASTA models were able to

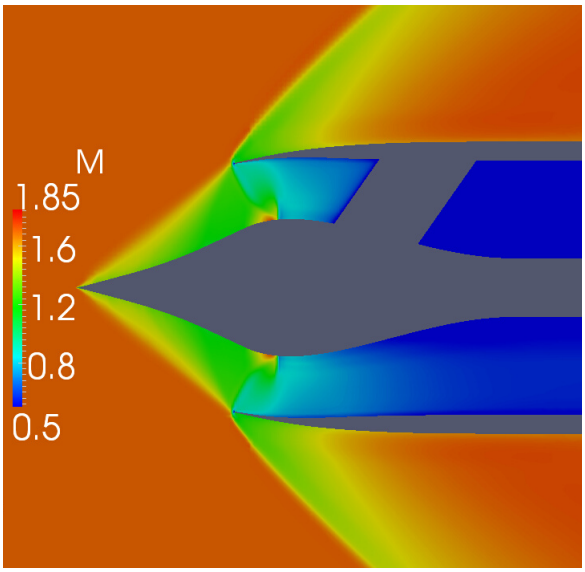

(a) 3-D model in x-z plane

	M_2	P_2 (Pa)	Mass Flow (kg/s)
GE	0.530	45930	191
PHASTA 2D	0.523	45856	189
PHASTA 3D	0.524	45783	189

(b) Steady state comparison

Figure 3.12: Steady state results

obtain accurate steady state representations of the inlet at cruise.

Additionally, these results show that the 2D and 3D models provide adequate representations of flow field at steady state. With this in mind, the inlet was run to steady state at four other operating conditions using the 2D model to minimize computational expense. The operating condition spanning fully sub-critical to super-critical, was controlled by varying the back pressure(P_B) as a percentage of the back pressure at the critical operating point ($P_B = 46,388\ Pa$). Table 3.5 and Figure 3.13 display the total pressure recovery normalized by the freestream total pressure as well as the mass flow rate at the compressor face normalized by the theoretical maximum captured mass flow rate. The theoretical maximum captured mass flow rate is determined by the free stream flow conditions and the radius of the cowl lip. Figure 3.14 displays the steady state flow field for four of these operating points. The most interesting feature from these simulations is the inlets sensitivity to back pressure at the critical operating point (Figure 3.14(c)). It can be seen that a ~1% increase in back pressure slightly alters the flow field by pushing the normal shock slightly upstream to become subcritical (Figure 3.14(b)). However, an additional ~1% increase in back pressure causes the normal shock to move almost halfway up the inlet, resulting in large losses both in total pressure and in captured mass flow rate (Figure 3.14(a)).

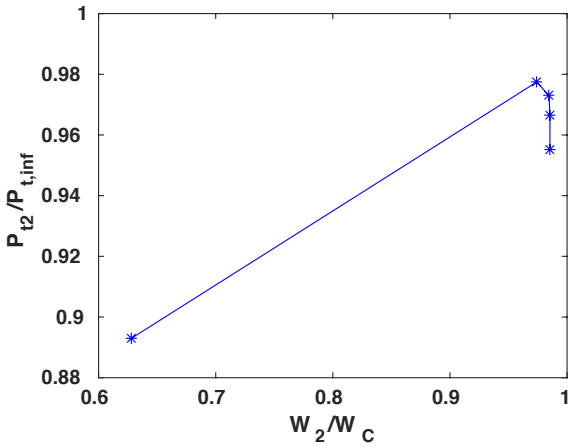

Figure 3.13: Cane Curve

Table 3.5: Cane Curve Results

Operating Condition	$\frac{P_B}{P_{B(Critical)}}$	$\frac{P_{T2}}{P_{T\infty}}$	$\frac{W_2}{W_{Cap}}$
Subcritical	1.023	0.8929	0.6276
Subcritcal	1.012	0.9774	0.9741
Critical	1.000	0.9730	0.9846
Supercritical	0.989	0.9664	0.9854
Supercritical	0.972	0.9554	0.9854

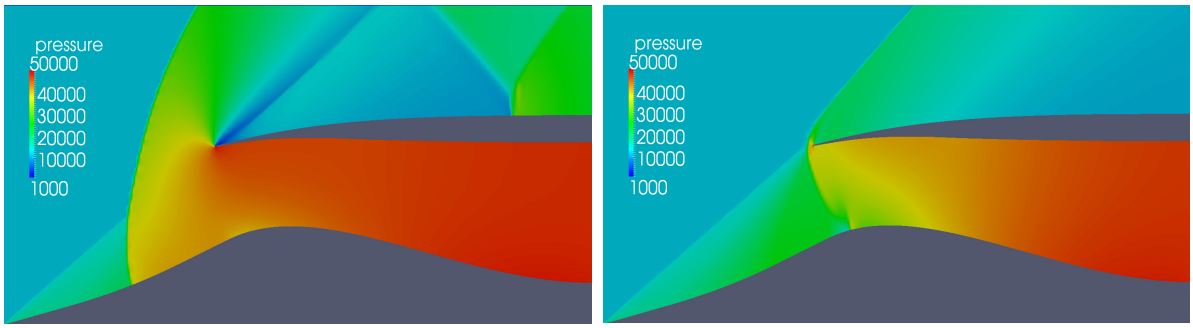

(a) $1.023P_{B(Critical)}$ (b) $1.012P_{B(Critical)}$

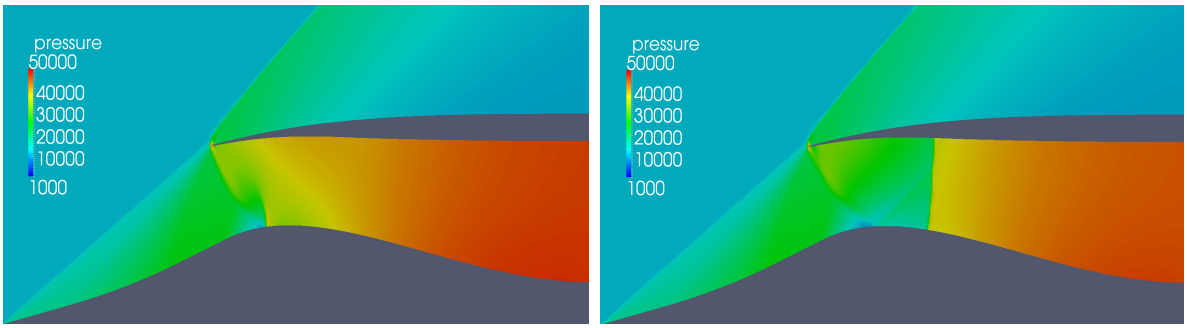

(c) $1.000P_{B(Critical)}$ (d) $0.972P_{B(Critical)}$

Figure 3.14: Operating Points

3.3 Dynamic PHASTA Results

With successful confirmation of the steady state results achieved, dynamic tests could be applied. All of these tests used a second order time integrator and a step size of $ts = 1e-5s$. The first test performed involved applying sinusoidal pressure perturbations to the inflow plane of the 2-D model (Figure 3.15). These perturbations were applied with an amplitude of 100Pa and at discrete frequencies between 10 and 2000 Hz. The pressure response was then measured at the outflow plane where the compressor face would be in the real propulsion system. The same test was also performed with the 3-D model but for a fewer number of frequencies due to the computational expense involved with the larger mesh.

Figure 3.16(a) shows the results of these tests in the form of a Bode plot where the gain is measured using the ratio of the max amplitude in pressure at the exit to the applied pressure amplitude at the inflow. What's important to note is that the 3-D test results overlap the 2-D

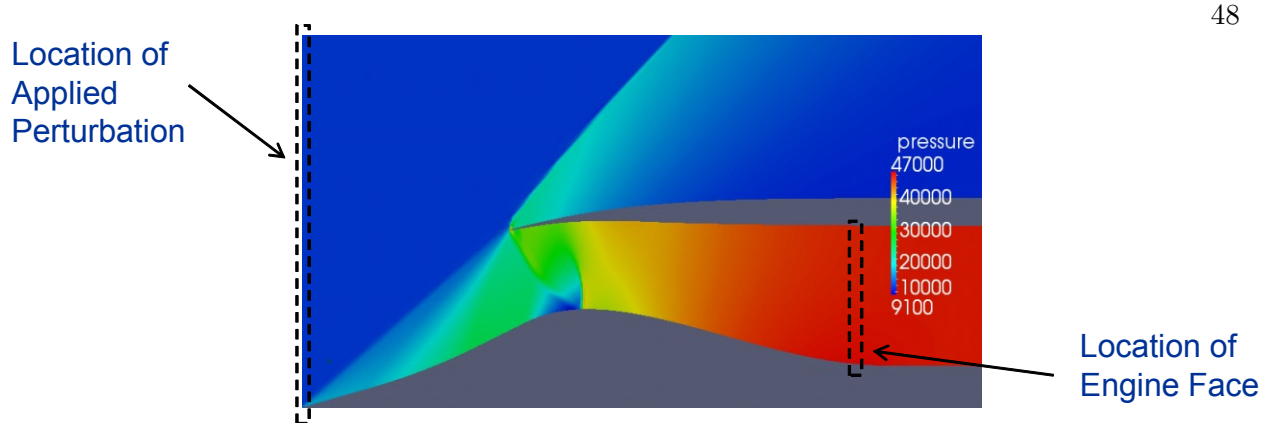

Figure 3.15: Location of perturbations shown on 2D model results

tests almost exactly. This was expected to happen because the flow field should not change around the centerbody, because the steady state solution is axisymmetric and the applied disturbance wave is normal to the primary flow direction. The results show that the 2-D model is an accurate representation of the inlets response to flow pressure perturbations. Furthermore, its appears that the inlets response varies significantly with frequency. It will be shown shortly that his is in fact an artifact of the pressure hard exit boundary condition and the subsequent disturbance reflection.

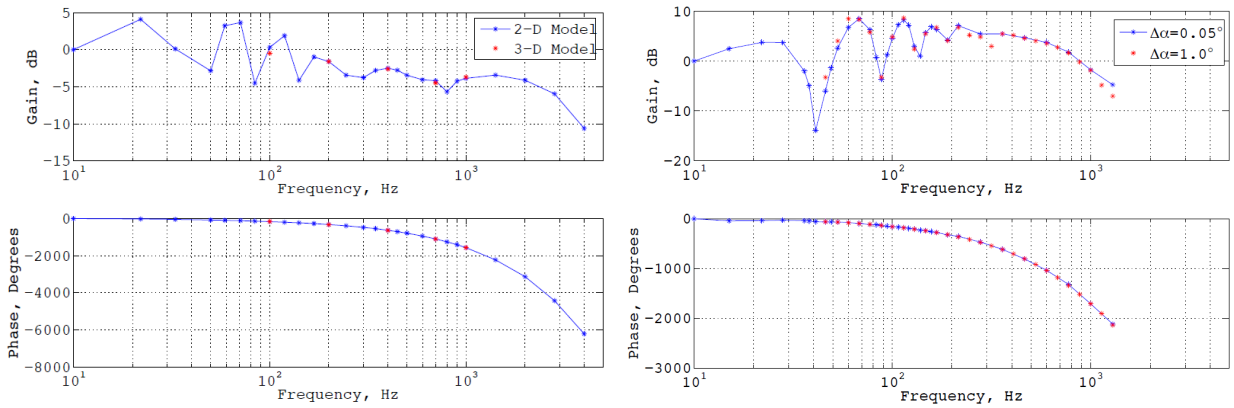

(a) Response to pressure perturbation

(b) Response to angle of attack perturbation

Figure 3.16: Bode plots of dynamic results

Following this test, the same perturbation was applied to the 2-D model at the operating points shown in Figure 3.14. For these cases a subset of frequencies were tested at (f =

$50, 80, 100, 200, 400$, and $1000Hz$). The results of these tests are shown in Figure 3.17. From here it appears that the inlets response varies significantly depending on both frequency and operating condition. Again it will be shown, that this is the affect of the exit boundary condition.

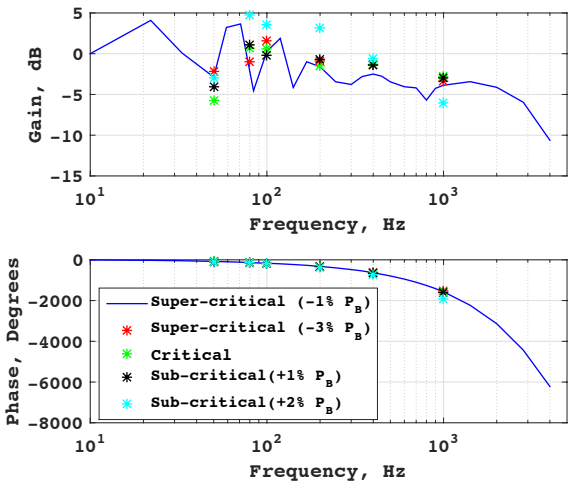

Figure 3.17: Response to pressure perturbations at various operating points

Another important feature of the PHASTA dynamic models is their response to variations in angle of attack. A series of tests were performed on the 2-D model by applying sinusoidal perturbations to the u and v velocity components to simulate perturbations in angle of attack. The corresponding change in pressure was measured at the outflow plane and used to create the Bode plot in Figure 3.16(b). The angle of attack tests were performed once with a max angle of attack of 0.05° and again with a max angle of 1.0°. The smaller angle is more realistic and is on the order of expected disturbances. The larger angle of 1.0° was applied to determine if the inlets response remained the same over a large range of disturbances even if it is unrealistic. From the results in Figure 3.16(a) it can be seen that the response is almost exactly the same for both situations. This means that any transfer functions potentially developed from these tests will be accurate for all expected perturbation amplitudes.

Additionally, $\Delta\alpha$ perturbations tests have been run on the 3-D model. The max angle of attack was 0.05° and the perturbations were applied at 6 select frequencies ($f = 88, 100, 215, 464, 681,$

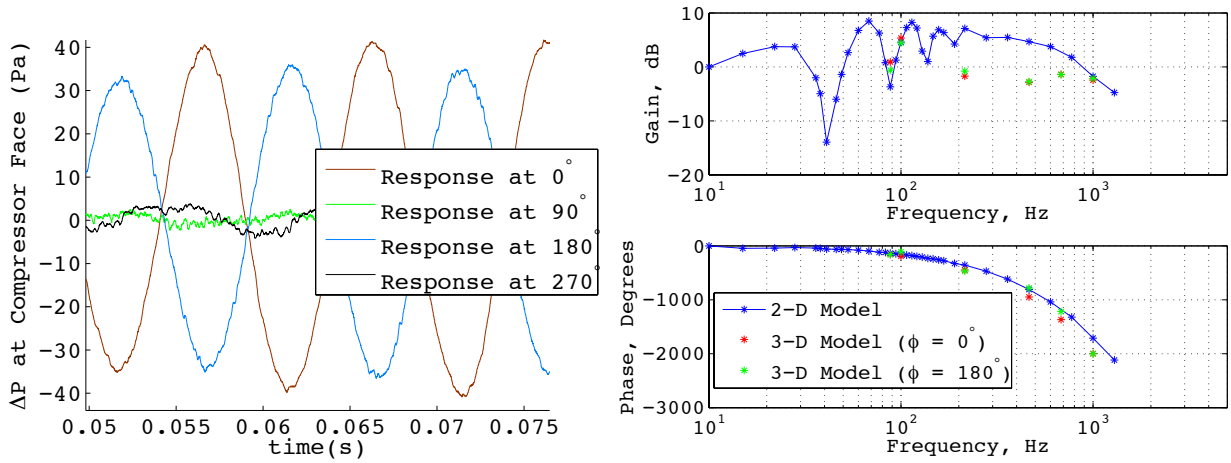

(a) 3D model's response to $100Hz$, $0.05°\Delta\alpha$ perturbation

(b) Response of 2D and 3D models to $0.05°\Delta\alpha$ angle of attack perturbation

Figure 3.18: 3D model angle of attack results

and $1000Hz$). Two distant features of note stand out from these results. The first is that the response at the compressor face differs depending on the azimuthal angle ϕ. This can be seen from Figure 3.18(a) where the response to a 100 Hz perturbation is measured at 4 different locations ($\phi = 0°, 90°, 180°$, and $270°$) on the compressor face by averaging the response of 7 probes along each respective line. The results show that the responses at $\phi = 90°$ and $270°$ are very small in magnitude while the responses at the $\phi = 0°$ and $180°$ are large in magnitude as well as $180°$ out of phase. This makes sense because the freestream disturbance is oriented along the x-y plane which includes the $\phi = 0°$ and $180°$ azimuthal angles but is perpendicular to $\phi = 90°$ and $270°$.

The second result of note is the preliminary Bode plot generated from the 3D case. As with the 2D case, the Bode plot is created by measuring the magnitude of the pressure response at the compressor face in relation to the applied angle of attack. In Figure 3.18(b) it can be seen that the results of the 3D case seem to match the data from the 2D case well at frequencies near 100 Hz but begin to diverge at higher frequencies. Whats more, is that there seems to be a phase shift at these frequencies as well. This is thought to result from the fact that the disturbances are not propagating completely in the x-direction and are free to reflect off of the wall of the internal duct.

These results prove the need for using a 3D model when simulating angle of attack perturbations and that a more complicated correction factor would be needed to reproduce these results in the lower order 1D model.

The results of both the 2-D and 3-D $\Delta\alpha$ perturbations tests seem to show the strong frequency dependance that the pressure perturbation tests displayed. Namely, that the gain contained large 'peaks' and 'valleys' close together. This behavior is easily explained with the help of the simple 1-D test case seen in Section 3.1. The behavior seen in Figure 3.9 is the same as that seen in both the pressure and angle of attack perturbation tests performed on the inlet (Figures 3.16(b) and 3.16(a)). This behavior is the result of the perturbation wave passing the measured response point, reflecting off of the outflow plane of the CFD domain, and overlapping with itself. This 'overlapping' occurs at a predictable time based on the speed of the perturbation and the length of the additional computational space ($\sim$ 0.025s in these simulations). Furthermore, this affect is only seen at frequencies below $\sim$ 200 HZ due to the coarseness of the grid spacing in the additional length which dampens the amplitude of the perturbations.

To illustrate this affect the same data was analyzed a second time but this time the response

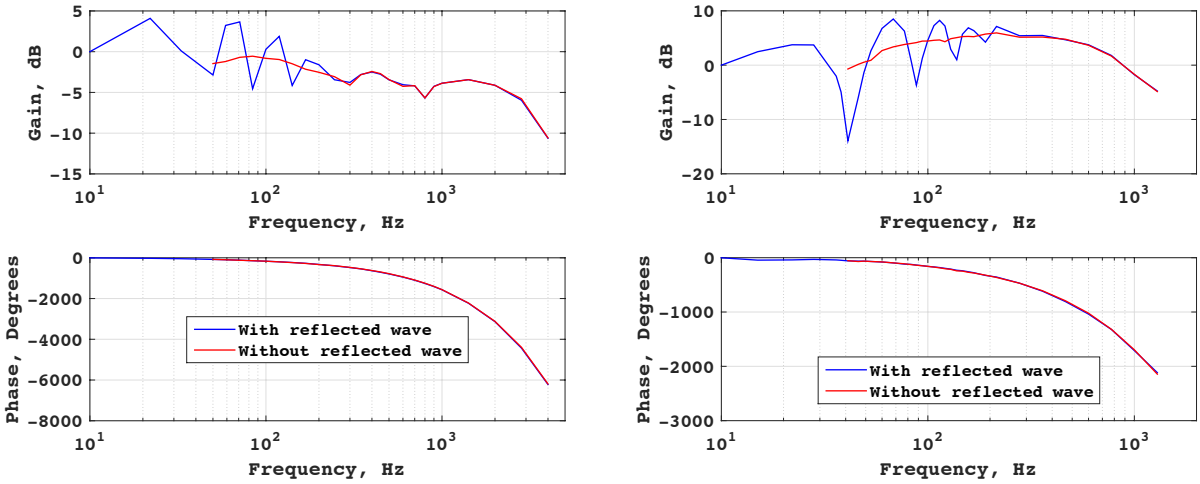

(a) Response to pressure perturbation

(b) Response to angle of attack perturbation

Figure 3.19: Bode plots of perturbation response before and after reflection

was recorded prior to the arrival of the reflected wave ($t < 0.025s$). In Figures 3.19(a) and 3.19(b) it can be seen that the 'peaks' and 'valleys' apparent in the previous results no longer exist. Without the reflected perturbation wave the response is similar to what has been previously shown for these types of tests, as in Kopasakis et al. It is clear from these results that the including or excluding the reflected wave has a significant influence on how the data is presented. If Figures 3.16 and 3.17 are now replotted without the reflected disturbance a slightly different picture is painted. In Figure 3.20(a), the main take away is essentially the same. Namely, that the 2-D and 3-D models give the same response to pressure perturbations and are equal representations of the flow field. The only difference is that the response is smoother. In Figure 3.20(b) it is now more clear that the 2-D model greatly overestimates the response to angle of attack perturbations. Previously, this could be seen somewhat but the shape of the Bode plots due to the disturbance reflection masked how large the difference was. The new results strengthen the belief that the 2-D model does not accurately portray angle of attack disturbances. In hindsight the 2D simulations are fundamentally flawed. The axisymmetric BC with this disturbance is like a "ring" of velocity perturbations as you revolve the applied velocity around the body which is inaccurate for angle of attack perturbations. Finally, Figure 3.21 shows the updated version of Figure 3.17 with the perturbation reflection. From these results, the response of the inlet now looks much less dependent on operating condition. The gain follows approximately the same trend as the baseline case. One interesting trend can be gathered however from this figure. It seems that, in general, the inlet in sub-critical operating conditions has a larger gain than at supercritical operating conditions. This is most likely due to that fact that the normal shock is further upstream and therefore has a higher average Mach number upstream of the shock, which creates a larger pressure jump across the shock.

The main question from these results is; which type of simulation is more accurate? It can be argued that both results have value. On the one hand, the length and grid coarseness of the extra length of computation domain are arbitrary and thus the exact shape of the initial Bode plots are unique to these simulations. However, in reality the inlet will have a compressor fan attached to it at the point where the response was measured so it is not possible to place the end

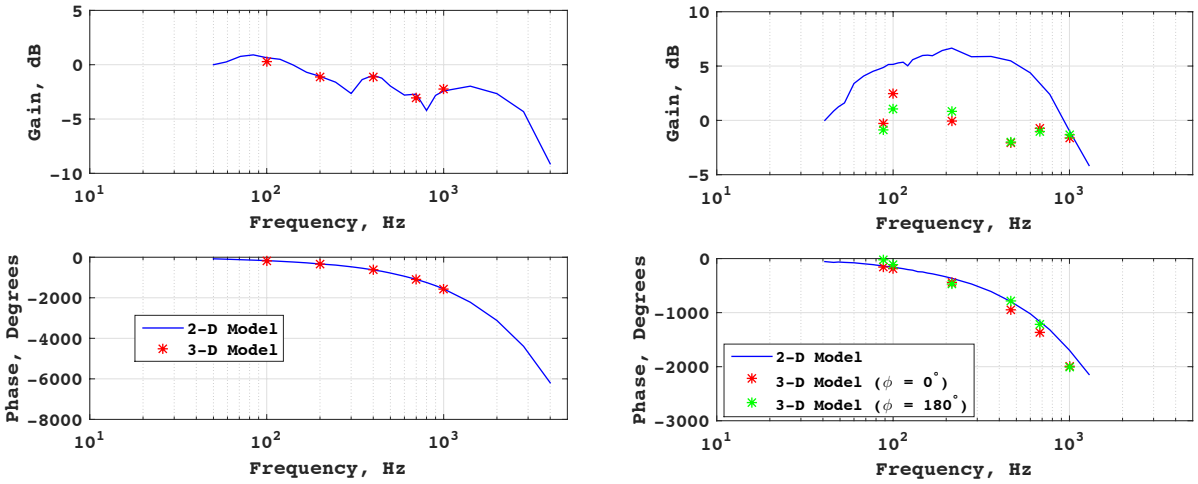

(a) Response to pressure perturbation

(b) Response to angle of attack perturbation

Figure 3.20: Bode plots of dynamic results without perturbation reflection

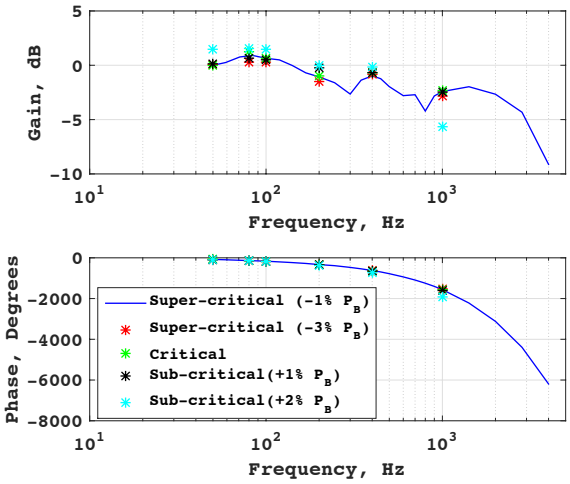

Figure 3.21: Response to pressure perturbations at various operating points without perturbation reflection

of the computational domain there if the response is to be measured. The domain will have to be placed somewhere and this behavior will occur in those cases as well. It is therefore important to present these results as cautionary tale moving forward so future researchers are aware of this potential issue. That being said, it is believed that the latter cases are more accurate and also more valuable. The engines response to these perturbations is the most important take away from

these tests. And while the compressor face will cause reflections to propagate upstream in the real case, all but a few of these simulations showed that this did not affect the normal shock position. In subcritical cases at a perturbation frequency of 50 HZ, the shock was shown to oscillate some. However, this too is dependent on the location of the exit plane so the exact movement cannot be considered accurate. For now the PHASTA results will be seen as accurately representing the inlets response to perturbations prior to the reflected wave. In a subsequent chapter, the 1-D model will use these results as a verification tool. Regardless of how the PHASTA results are viewed if the 1D model uses the same domain and produces the same results it can be said to provide an equivalent representation of the flow field.

3.4 External Compression Dynamic Results

Before moving on to the sections concerning the 1-D model development, it is important to discuss the results of one final PHASTA simulation as it is motivation for the next section. As mentioned previously, most quasi-1D inlet models in existence either ignore the dynamics of the external compression region or use a simple time delay for the propagation of disturbances through the region. A test case was performed using solely the external portion of the inlets centerbody. This geometry was converted to a 2-D representation and run to steady state using inflow cruise conditions ($M_\infty = 1.7$, P_∞, and T_∞). After this, probes were located in the flow field spaced evenly in the x-direction and y-direction (400 total). Finally a step in pressure with an amplitude of 100 Pa was applied at the inflow plane and its propagation through the flow field was recorded. The process is detailed in Figure 3.22.

The results from this test can be seen in Figure 3.23. Here, the disturbance was recorded at three locations marked with a star as seen in Figure 3.23(a). In Figure 3.23(b), the y-axis variable "P_{Prime}" refers to the pressure rise due to the perturbation where the local steady state pressure has been subtracted out. As predicted, the disturbance propagates as two distinct waves in the free stream, which can be seen in Figure 3.23(b). However, one feature stood out from the test that differed from expectations. Namely, that the rise time to the new steady state within the

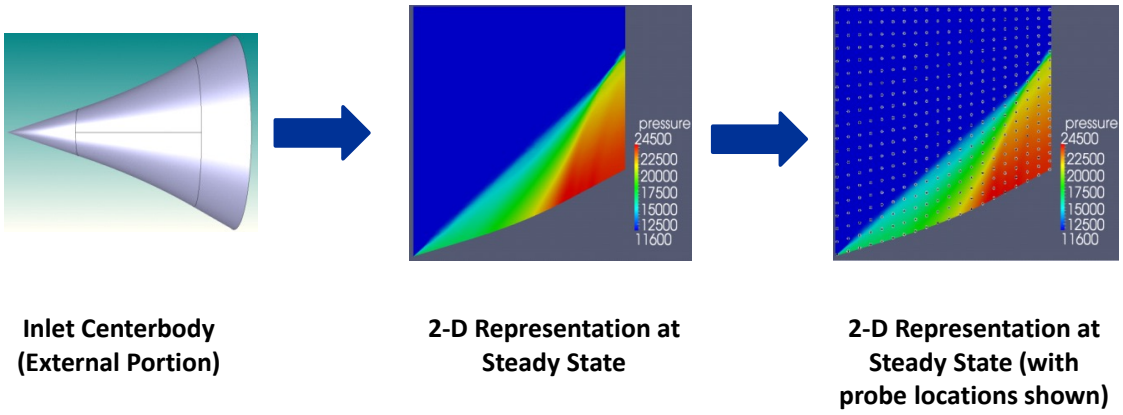

Figure 3.22: Dynamic Test of Eternal Compression Flow Field

shock field did not occur in two distinct steps as was the case with the simple 1-D test case in Figure 3.8 (Test b) and as is seen at the free stream location(green data) of Figure 3.23(b). Instead three steps are seen at the points within the shock wave. The first and last are due to the fast and slow acoustic waves as was expected. The second wave however, was due to the entropy wave which normally does not affect the pressure response downstream of a disturbance. This case differs from the previous 1-D test case due to the conical shock wave. Consequently, the entropy wave temporarily changed the shock angle as it passed through, causing a jump in flow variables.

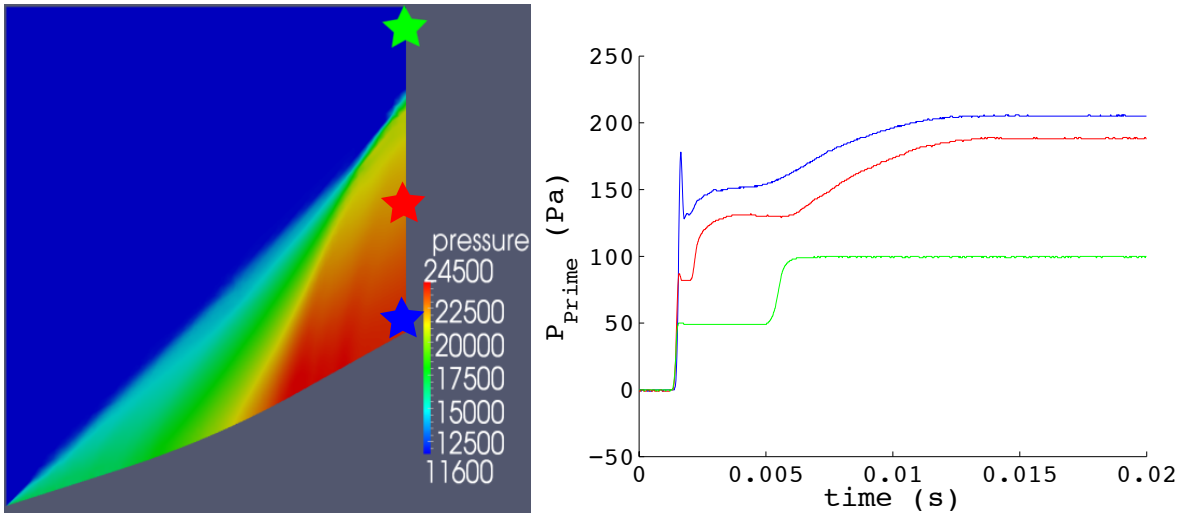

(a) Location of the three example probes

(b) Response pressure step perturbation

Figure 3.23: Preliminary external compression dynamic results

Additionally, the slow acoustic wave is seen to approach the new steady state condition asymptotically. The reason for this behavior, as will be shown in the next section, is because the response at any given point in the shock field is due an upstream region of influence predicted by characteristic lines. Disturbances will propagate through the flow field at different speeds depending on the local velocity and speed of sound. The response at a given point is therefore the result of the single step disturbance being distorted in time by the local flow properties at different points within its zone of influence. Previous attempts to model the external compression field use the states predicted by isentropic relations combined with a time delay to compensate for the propagation of disturbances. The results of this test show that a more sophisticated technique is needed to accurately capture the dynamic response of the external compression flow field. Furthermore, this test illustrates the need for a high fidelity model to help guide the development of the lower order model.

Chapter 4

External Compression Flow Field Modeling

It was seen in the previous chapter that perturbations move through the external compression flow field in a nontrivial manner. The following chapter will be devoted to developing a dynamically accurate 1-D model for this portion of the inlet. First an accurate steady state method is presented which was developed using the axisymmetric method of characteristics (MOC) combined with a Taylor-Maccoll (TM) equation solver. The accuracy of the TM solver is first verified using a GUI from the NASA Glenn website. From here, the development of the MOC code is presented and then verified using the results from PHASTA. Then a method for transforming a 2-D flow field into an equivalent 1-D representation will be presented. This is necessary for its implementation in the 1-D model. Lastly, a novel approach to modeling the unsteady dynamics of the external flow field will be presented. This approach combines aspects of previous models [1, 40], where flow field disturbances are decomposed into characteristic wave disturbances with a new method for propagating these disturbances throughout the flow field.

4.1 Taylor-Maccoll Equation Solver

The axisymmetric MOC is used to solve the steady state solution of the external flow field but this method requires a known solution state to 'seed' it. Fortunately, the TM equations accurately represent the flow at the tip of the centerbody. As mentioned in Section 2, the TM equations are accurate for semi-infinite cones in supersonic flow. The initial portion of the inlet's centerbody has a constant flow deletion angle and therefore fits this description. The process for calculating a

solution to the TM equations was described in Section 2 and will be briefly reiterated here.

Under the assumptions just described, the flow variables are constant along ray emanating from the cone's tip and the Euler equations, written in spherical coordinates, can be reduced to a single ordinary differential equation (the TM equation). This equation has no closed form solution so it must be integrated numerically. There are two approaches that can be used to accomplish this. The first is the direct method that starts by solving for the flow variables at the cone"s surface and then integrating the Taylor-Maccoll equation until a boundary condition is matched at the shock wave. The second is the inverse method, which is used in this research, and reproduced from Anderson[4]. The inverse method starts by assuming a value for the angle of the oblique shock wave and calculating the Mach number and flow direction behind the shock using the theta-beta-Mach relations[4]. The remaining distance between the cone's surface and the shock is broken up into incremental flow angles. A numerical integrator can be used to solve for the flow field. If the correct shock wave angle is used the normal component of velocity will be zero. In most cases this will not be true for the first guess so an iterative process must be used. Once the correct shock angle is found within a prescribed error tolerance the flow field around the cone will be correctly solved for.

For the purposes of this research, the above described method was programed in Matlab and the 4^{th} order accurate Runge-Kutta ODE solver ODE45 was used to iterate the TM equation. The results of this process compare favorably to those from the GUI on the NASA GRC website [20] (Figures 4.1(a) and 4.1(b)). As mentioned, the code solves the Taylor-Maccoll equations numerically and is guided by the user set tolerance of the normal velocity error at the cones surface. Figure 4.1 shows that favorable results can be obtained with a relatively low error in the calculated shock angle by prescribing a relatively high error tolerance. This resulted in very quick calculation time (< 2 sec). It should be noted that the equation solver behind the GUI on the NASA website most likely uses either the direct or inverse method to solve the TM equations. It is not known which method is used the process is iterative in either case and similar error tolerance must be specified. The user is not given the option to set this tolerance which is most likely the reason that the results

do not converge exactly. Given that the results of the TM solver used in this research do converge after a prescribed error tolerance, it is likely that the final values achieved are more accurate.

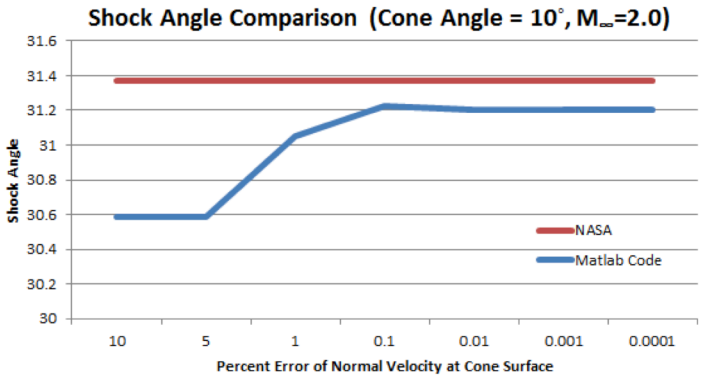

(a) Shock convergence study based on prescribed error at cone surface

	NASA Website	Matlab Code	% Error
Shock Angle	31.37	31.21	0.528
$M_{surface}/M_{\infty}$	0.912	0.917	0.548
$P_{surface}/P_{\infty}$	1.310	1.293	1.330
$T_{surface}/T_{\infty}$	1.080	1.076	0.364

(b) Comparison to NASA GRC website

Figure 4.1: Taylor-Maccoll solver results compared to NASA website [20]

4.2 Axisymmetric Method of Characteristics

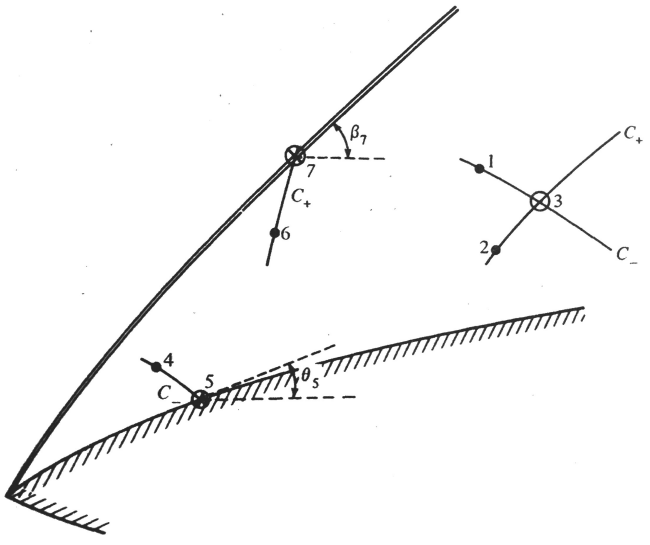

Figure 4.2: Axisymmetric MOC mesh generation (Anderson[4])

The MOC was chosen to model the external compression flow field because it is the best combination of accuracy and computational speed that satisfies the assumptions for this model. In this region of the flow field, the flow is axisymmetric, supersonic, irrotational and is assumed to

be inviscid and therefore the axisymmetric MOC is applicable [4]. In Section 2.3 the method of characteristics was briefly described. Its implementation is a little more nuanced and the source material [4] that the code is based off of provides an outline but not a complete description of how to apply it. For this reason, there likely exists several equally valid approaches to using the method, therefore some time will be spent on exactly how the method was used in this research.

The MOC works for supersonic, unsteady, irrotational flow because both characteristic lines point downstream. For this type of flow, Equation (4.1) describes the direction of both the positive and negative characteristic lines at any point in the flow field.

$$\left(\frac{dr}{dx}\right)_{C_\pm} = tan\left(\theta \pm \mu\right) \tag{4.1}$$

$$\mu = sin^{-1}\left(\frac{1}{M}\right) \tag{4.2}$$

Here θ is the local flow direction, μ is the Mach angle which is found from Equation (4.2), and $C_\pm$ corresponds to the positive and negative characteristic lines. For these equations, cylindrical coordinates are assumed and x and r correspond to the axial and radial directions respectively. Along these lines the compatibility equations describe the variation of the flow properties. They are seen represented as in Equation (4.3).

$$d\left(\theta \mp \nu\right)_{C_\pm} = \frac{1}{\sqrt{M^2-1} \pm cot\theta}\left(\frac{dr}{r}\right) \tag{4.3}$$

$$\nu = \sqrt{\frac{\gamma+1}{\gamma-1}}tan^{-1}\sqrt{\left(\frac{\gamma-1}{\gamma+1}\right)\left(M^2-1\right)} - tan^{-1}\sqrt{M^2-1} \tag{4.4}$$

Here, M is the local Mach number, γ is the ratio of specific heats and ν is the Prandtl-Meyer function seen in Equation (4.4). If the flow state is known at two adjacent points, the flow at a new point can be determined by finding the intersection point of the positive characteristic line of one initial point and the negative characteristic line of the other point. This is seen in Figure 4.1(b), where the negative characteristic of point 1 intersects with the positive characteristic of point 2

at point 3. At point 3, the compatibility equations (4.3) are solved numerically and the solution is found. Therefore, if a know line of data points is located at some point upstream, the entire solution of the flow field can be determined using this process. The exact way in which this was accomplished will now be shown.

Unlike two dimensional supersonic flows, both the characteristic line and compatibility equations are described by ODEs which require a numerical method to solve for them. Using the forward difference method Equations (4.1) and (4.3) can be recast as Equations (4.5) and (4.6) between two points (i and j) in the flow field:

$$\left(\frac{r_j - r_i}{x_j - x_i}\right)_{C_\pm} = tan\left(\theta_i \pm \mu_i\right) \tag{4.5}$$

$$\left(\theta_j \mp \nu_j\right)_{C_\pm} = \frac{1}{\sqrt{M_i^2 - 1} \pm cot\theta_i}\left(\frac{r_j - r_i}{r_i}\right) + \left(\theta_i \mp \nu_i\right)_{C_\pm} \tag{4.6}$$

If Equations (4.5) are expressed in terms of the flow state at points 1 and 3 using the positive characteristic version of Equations (4.5) and the flow state at points 2 and 3 using the negative characteristic version of Equations (4.5), they can be combined algebraically to find the location of point 3 resulting in Equations (4.7) and (4.8):

$$x_3 = \frac{x_2 tan\left(\theta_2 - \mu_2\right) - x_1 tan\left(\theta_1 + \mu_1\right) - r_2 + r_1}{tan\left(\theta_2 - \mu_2\right) - tan\left(\theta_1 + \mu_1\right)} \tag{4.7}$$

$$r_3 = \left(x_3 - x_2\right) tan\left(\theta_2 - \mu_2\right) + r_2 \tag{4.8}$$

Likewise, if Equations (4.6) are expressed along the positive characteristic line from point 1 to point 3 and along the negative characteristic line from point 2 to point 3, they can be combined to find the flow direction θ and the P.M. function ν at point 3.

$$\theta_3 = \frac{1}{2}\left[\left(\theta + \nu\right)_3 + \left(\theta - \nu\right)_3\right] \tag{4.9}$$

$$\nu_3 = \frac{1}{2}\left[(\theta+\nu)_3 - (\theta-\nu)_3\right] \tag{4.10}$$

These equations hold for points that are in the region between the centerbody surface and the conical shock wave. For points on the surface, the flow angle is known so the negative characteristic line coming from a point just above the surface (point 4 in Figure 4.1(b)) can be used to find the state of the flow on the surface (point 5 in Figure 4.1(b)). Using the negative characteristic version of eqns (4.1) and the geometry of the surface the new point can be found at point 5. Additionally, the PM function can be found from the negative characteristic form of Equation (4.6) along with the known flow angle θ_5. This results in eqns (4.11) and (4.12):

$$(\theta+\nu)_5 = \frac{1}{\sqrt{M_4^2-1} - cot\theta_4}\left(\frac{r_5 - r_4}{r_4}\right) + (\theta+\nu)_4 \tag{4.11}$$

$$\nu_5 = (\theta+\nu)_5 - \theta_5 \tag{4.12}$$

Likewise, points near the conical shock wave require similar treatment. For points on at the shock wave, the flow angle is also known so the positive characteristic line coming from a point below the shock (point 6 in Figure 4.1(b)) can be used to find the state of the flow on the surface (point 7 in Figure 4.1(b)). Using eqns (4.1) and the assumed initial shock angle, the new point at the shock can be found. From here, the positive characteristic form of the PM function can be found from Equation (4.13).

$$(\theta-\nu)_7 = \frac{1}{\sqrt{M_6^2-1} + cot\theta_6}\left(\frac{r_7 - r_6}{r_6}\right) + (\theta-\nu)_6 \tag{4.13}$$

However, in this case the shock angle itself can change due to the influence of flow behind it. For these points an iterative process is used were the shock angle calculated previously is used to find the states behind at point 7 using the theta-beta-Mach Equation. The values for θ and ν predicted from this local shock angle is compared to that predicted by Equation (4.13). If the difference is too large a new guess for the local shock angle is used and the process is repeated.

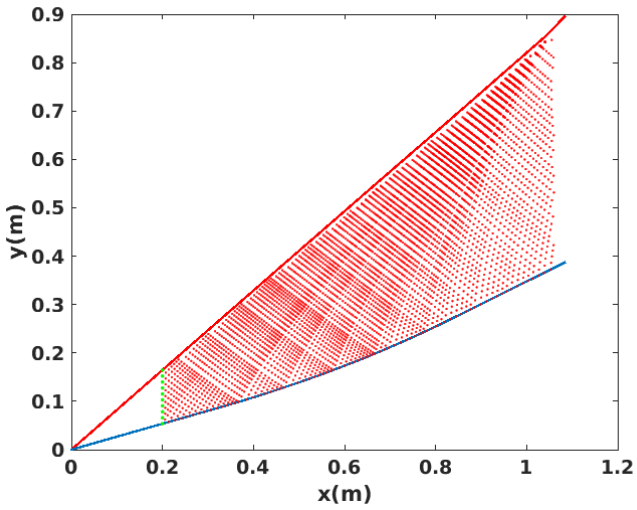

Figure 4.3: Axisymmetric MOC mesh

The above process describes how individual mesh points are created but not the entire process. Overall, the MOC solutions starts by determining the initial shock wave and the solution in the semi infinite cone portion of the centerbody using the TM equation solver. Using this solution the MOC method can be seeded with an initial data line (green points in Figure 4.3). These points are interpolated from the TM solution and their grid spacing (Δr) was shown to influence the accuracy of the final MOC solution. A finer grid spacing initially led to a more accurate final solution but also increased computational expense. From this initial data line new points were created by looping over the initial points and creating new mesh points using Equations (4.7)-(4.13) for interior, surface, and shock points. From here a new line of data down stream was created and the process continued (red points in Figure 4.3). This process had to altered however because it was found that the mesh points concentrated around compression waves emanating from the curvature of the centerbody in the isentropic compression region. Left on its own, the mesh generation process stalled as the mesh points became too concentrated and each new line of data was generated at shorter and shorter distances downstream. This issue was overcome by creating a conditions that removed new points if they were to close to pre-existing point from a previously created data line. With this fix the solution was generated successfully. One interesting takeaway is that this process

helps visually the flow field just by the grouping of mesh points. The compression waves do exist in the flow field and this grouping of mesh points as seen in Figure 4.3 illustrates where they are.

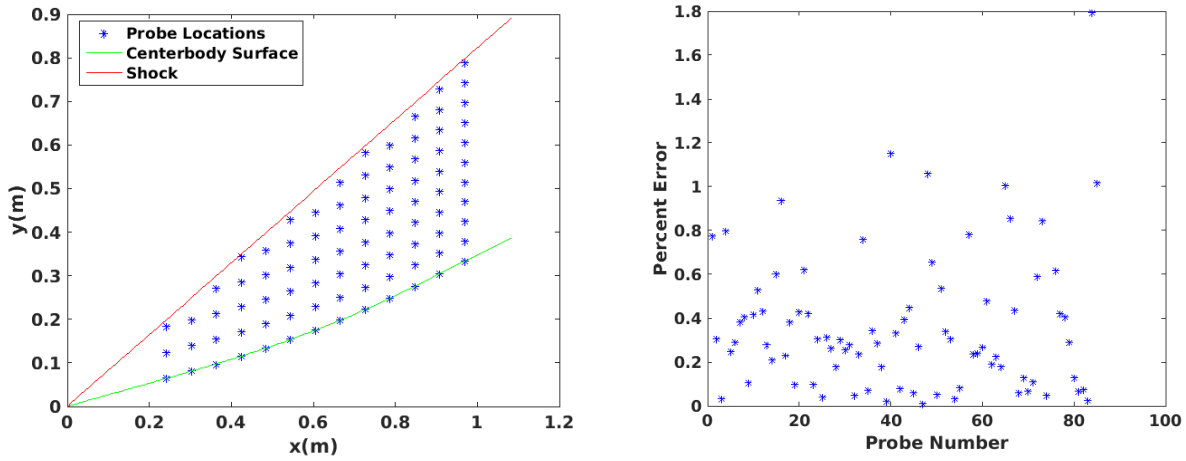

(a) Probe locations

(b) Relative error in Mach number

Figure 4.4: Comparison of MOC and PHASTA solutions

To evaluate the accuracy of this method, the results from the previously discussed PHASTA simulations were compared with it. To do this, probes were placed in both the PHASTA and MOC solution fields as seen in Figure 4.4(a). The flow states were then interpolated from the solutions at each probe point. Figure 4.4(b) shows the relative error at each probe location between the two solutions. As can be seen in this figure, the MOC solution compares to PHASTA extremely well. In all but a few locations the percent difference was less than %1. Similar tests were performed for the flow variables resulting in the same level of accuracy. From, these results it was concluded that the MOC formulation used here provided an accurate steady state representation of the external compression flow field.

4.3 Equivalent 1-D Representation of a 3-D Flow Field

With the confirmation of the MOC code as an accurate representation of the external flow field, it is now an appropriate point to discuss how this will fit into the 1-D model. The output of the MOC is a 2-D solution field spanning the axial and radial directions. For implementation

into the 1-D code, an accurate 1-D representation is needed. The reason being, is because the internal duct portion during critical(plane A Figure 4.5) and supercritical (not shown) operation and the flow field aft of the normal shock during subcritical operation(planes B and C Figure 4.5) is modeled using quasi 1-D equations. These equations need the MOC solution as an upstream boundary condition in order run. Initially, the flow state(P, ρ, T, etc.) at a given x location was averaged and used to determine the basic conservation flow variables $\boldsymbol{U}$. However, this approached resulted in large errors in mass flow rate and thus compromised the total solution. For this reason, the method for determining an equivalent 1-D flow field found in the LAPIN report [57] was used.

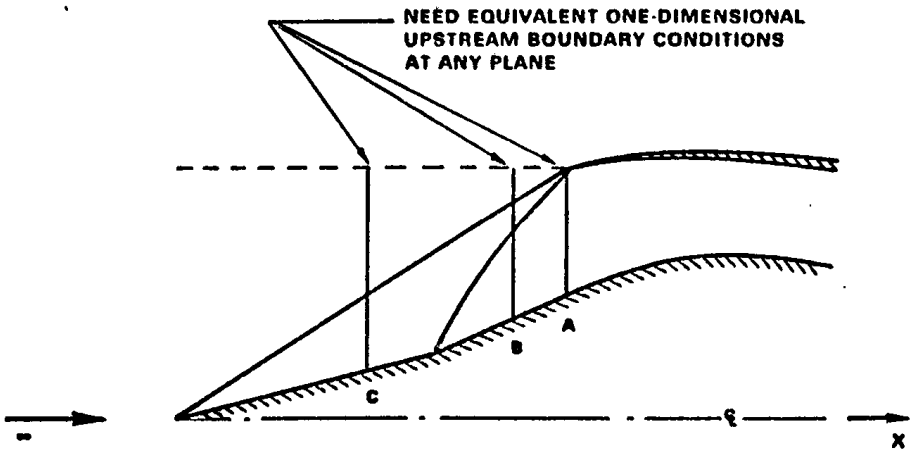

Figure 4.5: Equivalent 1-D States (LAPIN report [57])

In the LAPIN report the process of converting a 2-D flow field to an equivalent 1-D representation is detailed. The derivation presented in this report contains an error so a brief derivation will be shown here. For any given plane in the external flow field (A, B, or C in Figure 4.5), the area integral average flux through that plane can be calculated with Equations (4.14), (4.15) and (4.16).

Continuity:

$$Q_1 = \int_A \rho u dA \tag{4.14}$$

Momentum:

$$Q_2 = \int_A (p + \rho u V)\, dA \tag{4.15}$$

Energy:

$$Q_3 = \int_A (\rho E_{tot} + p)\, u dA \tag{4.16}$$

Here, V is the total velocity and u is the velocity component in the x-direction. When evaluating MOC results, the integrals in these equations were evaluated using a combination of the trapezoidal rule and Richardson extrapolation. The details of these method are standard and are detailed in (reference numerical methods class notes). Conversely, when PHASTA results were being evaluated, the post processing tool Paraview was used to evaluate these equations by taking advantage of its surface integration tool chain. In Paraview, a 2-D plane or 'slice' can be placed in a 3-D solution field and a built-in integrator finds the integral over the slice area. This was accomplished by writing a code in Python which looped over the solution files for a given number of time steps, performed the integration using Paraview, and saving the files the a .csv file. From there the filed is converted to a Matlab file to continue post-processing the data.

In terms of the conservative flow state variables $\boldsymbol{U}$, the Q equations can be represented as:

Continuity:

$$Q_1 = U_2 \tag{4.17}$$

Momentum:

$$Q_2 = \left[(\gamma - 1)\, U_3 + \left(\frac{3-\gamma}{2}\right)\left(\frac{U_2^2}{U_1}\right)\right] \tag{4.18}$$

Energy:

$$Q_3 = \left[\gamma U_3 - \left(\frac{\gamma - 1}{2}\right)\left(\frac{U_2^2}{U_1}\right)\right]\left(\frac{U_2}{U_1}\right) \tag{4.19}$$

It was found that the equation for the flux term in the momentum equation had an error by re-dressed these equations. The $(\gamma - 1)\, U_3$ term is listed as $(\gamma + 1)\, U_3$ in the LAPIN report. This

caused the initial solution to be incorrect. In addition to this error, the following equations had to be re-derived to calculate the conservative flow variables. The original equations were found to be inaccurate. From here, the conservative flow state variables $\boldsymbol{U}$ can be solved for using Equations (4.20), (4.21) and (4.22).

$$U_2 = Q_1 \tag{4.20}$$

$$\frac{U_2}{U_1} = \frac{-b \pm \sqrt{b^2 - 4ac}}{2a} \tag{4.21}$$

$$U_3 = \frac{Q_2}{\gamma - 1} - \frac{3 - \gamma}{2\left(\gamma - 1\right)} Q_1 \frac{U_2}{U_1} \tag{4.22}$$

where,

$$a = -\frac{(\gamma + 1)}{2\left(\gamma - 1\right)} Q_1 \tag{4.23}$$

$$b = \frac{\gamma}{\gamma - 1} Q_2 \tag{4.24}$$

$$c = -Q_3 \tag{4.25}$$

From this point on, this method will be used to transition from a 2-D flow field to a 1-D representation when necessary.

4.4 Dynamic Modeling of the External Compression Flow Field

With the steady state solution for the external compression flow field calculated successfully using the MOC, it was then possible to create a dynamic model. Initially the method detailed by MacMartin and mentioned in Section 2.3 was tested. The initial results were promising but

ultimately the method was not able to be adapted to the external compression flow field. Although this method was unsuccessful it did provide several insights that were key in development of the final model. Namely, the decomposition of flow variable perturbations into disturbance waves and the propagation speed of these waves. Ultimately, a new method was created where temporary steady state solutions were found for each of the disturbance waves created using the MOC and the transition time between these solutions was modeled using their propagation delays along streamlines. The details of the process will now be shown.

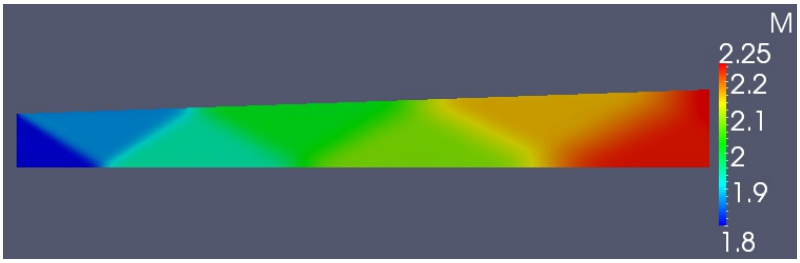

(a) Supersonic Expansion

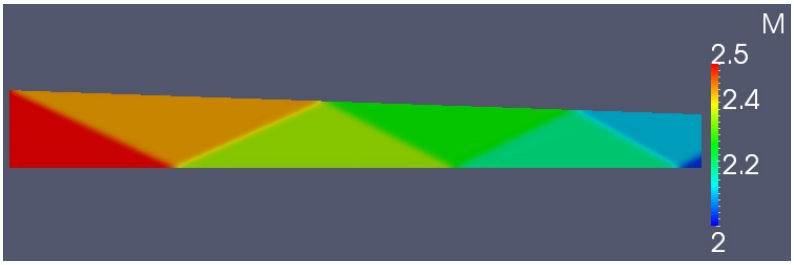

(b) Supersonic Compression

Figure 4.6: 2D duct test case PHASTA simulations

To test the method created by MacMartin, a simple 2-D duct with an area ratio of 1.454 between the inflow and outflow planes was created in PHASTA. The duct could be run as either supersonic expansion (Figure 4.6(a)) or supersonic compression (Figure 4.6(b)) depending on the choice of the inflow plane. For both of these simulations, PHASTA was run to steady state using the conditions in Table 4.1, where the flow remained supersonic throughout and therefore no exit boundary conditions were needed. In both cases, after steady state was achieved a step in pressure of 100 Pa was applied to the inflow plane and the response was measured at a distance of 1.05m downstream.

Table 4.1: 2D test case boundary conditions

Boundary Condition	**Supersonic Expansion**	**Supersonic Compression**
Inflow M	1.8	2.5
Inflow P (Pa)	11597	11597
Inflow T (K)	216.65	216.65
Slip Walls	$\vec{V} \cdot \vec{n} = 0, \partial T/\partial x_n = 0$	$\vec{V} \cdot \vec{n} = 0, \partial T/\partial x_n = 0$

Next the method detailed by MacMartin was implemented in Matlab. First, the applied pressure perturbation of $\delta p = 100Pa$ was decomposed into three disturbance waves using Equation (3.1). Then, the time delay of each disturbance wave was computed using Equations (2.14). Next, the amplitude gain was calculated for the fast and slow acoustic waves using Equation (2.15). Finally, the disturbance waves were converted back to flow variables using Equation (3.2). As can be seen in Figures 4.7(a) and 4.7(b), this method did an excellent job of predicting both the amplitude and time delay of the disturbance waves created by the pressure perturbation. Here the change in pressure at the measured down stream point (x = 1.05m) due to the applied pressure perturbation is shown.

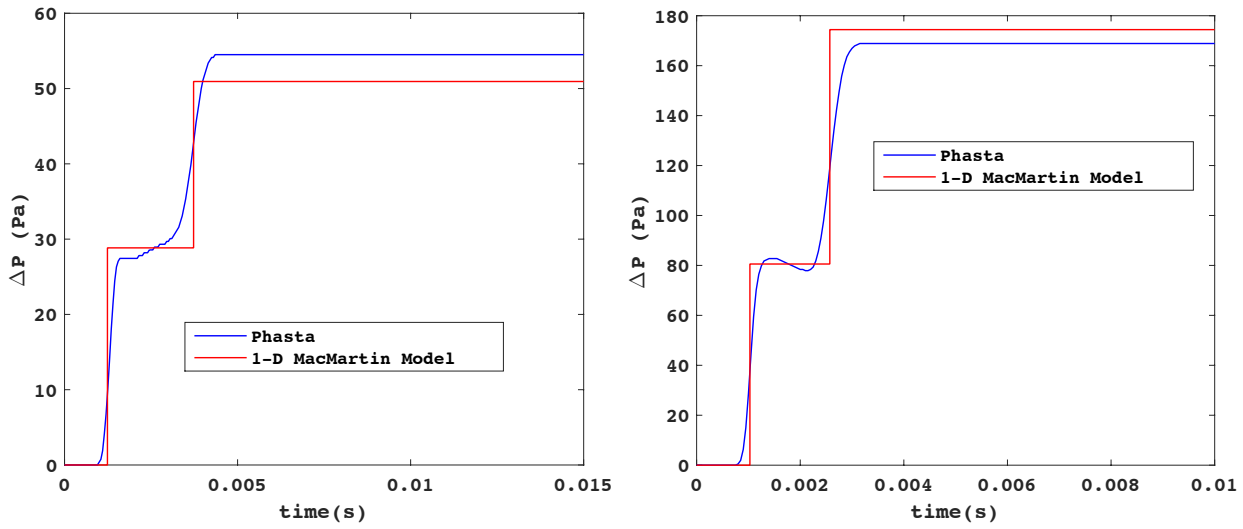

(a) Supersonic Expansion

(b) Supersonic Compression

Figure 4.7: 2D duct test case results

With these results, the MacMartin method was then applied to the external compression

flow field of the inlet. In this case the MOC was used to find the steady state solution of the external compression portion of the inlet. Freestream conditions were applied at cruise altitude to the inflow plane as summarized in Table 3.4. In this approach, the integral area average of the MOC solution was taken at 33 equally spaced locations in the axial direction, spanning the entire external flow field, from the freesteam to where the cowl lip region would be located in the real inlet case ($x = X_{CL}$). This was done using Equations (4.14)- (4.22). The MacMartin method that was detailed in the 2-D duct case was then run using this 1-D representation using the same pressure perturbation of $\delta p = 100Pa$. To verify this test, the external compression PHASTA model seen in Section 3.4 was run to steady state using the boundary conditions in Table 3.4 and the mesh and time discretization setting discussed in Section 3.1. For this simulation, no exit boundary conditions were applied, as the flow remained supersonic throughout the whole solution field. The simulation was then perturbed with a pressure perturbation of $\delta p = 100Pa$ at the inflow plane. The response was recorded at the cowl lip location($x = X_{CL}$) at a sampling rate of 20000Hz by using the Python script and the Paraview post processing program discussed previously.

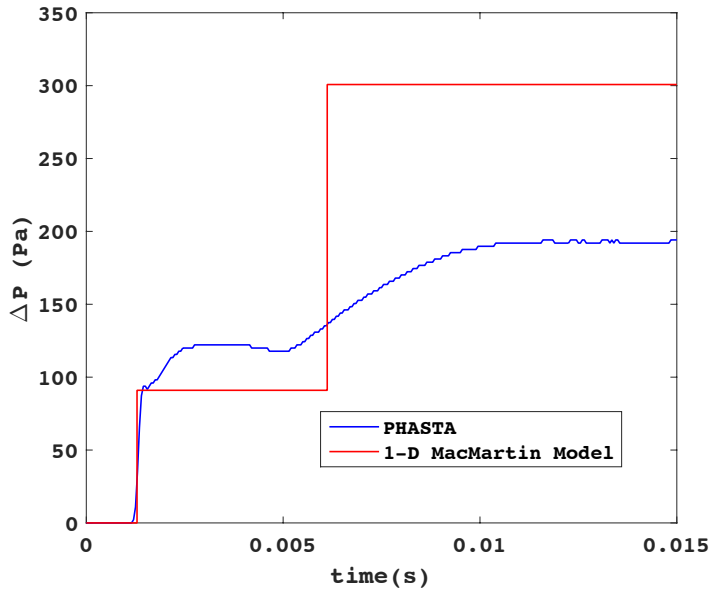

Figure 4.8: MacMartin model applied to the external compression flow field

As can be seen in Figure 4.8, the MacMartin method applied to the reduced MOC solution

does not do an adequate job of simulating the dynamic response of the flow field. There are two reasons for this. First, the time delay predicted using this method predicts the disturbance to move as two step waves. The PHASTA results clearly show that this is not accurate especially in the case of the slow acoustic wave. The reason, as discussed in Section 3.4, is because the disturbance waves are warped by the axially and radially varying speed of sound and velocity throughout the flow field. The second reason, is that by reducing external compression flow field to a 1-D representation, the affects of the conical shock wave are neglected. In MacMartin, an equation is derived for the propagation of disturbance waves through a normal shock (Equation (2.16)). Here, he discusses the affect of the normal shock on amplify or damping the disturbance waves. However, this equation does not apply to oblique or conical shock waves. Additionally, without accounting for the conical shockwave, the affects of the entropy wave are completely missing. This happens, because although the entropy wave does not affect the pressure directly, it does affect the strength of the shock wave as it passes through it and thus indirectly raises the pressure aft of the shock. One solution to this problem, would be to re-derive the normal shock equation in MacMartin for oblique and conical shockwaves. However, this, if successful, would only account for the correct amplification factors across the shockwave and not account for the correct time response. This is problematic because one of the main goals of this research is to successfully model the response to sinusoidal perturbations. As can be seen in Figure 4.8, the length of the response to a pressure perturbation in time is on the scale of the frequencies of interest. Therefore, using a method that does not accurately capture this affect would result in completely erroneous responses to sinusoidal perturbations.

The solution to this issue involved using a novel approach to propagate disturbances through the flow field. To start the solution, the steady state problem was solved using the MOC. Then the incoming flow variable disturbance was decomposed into the 3 constituent disturbance waves (δ^+, δ^e and δ^-) using Equation (3.1). Then each of these waves was individually converted back into flow variable disturbances using Equation (3.2). Next, each of these disturbances represented in flow state variables are used as freesteam inputs to find a new temporary steady state solution using

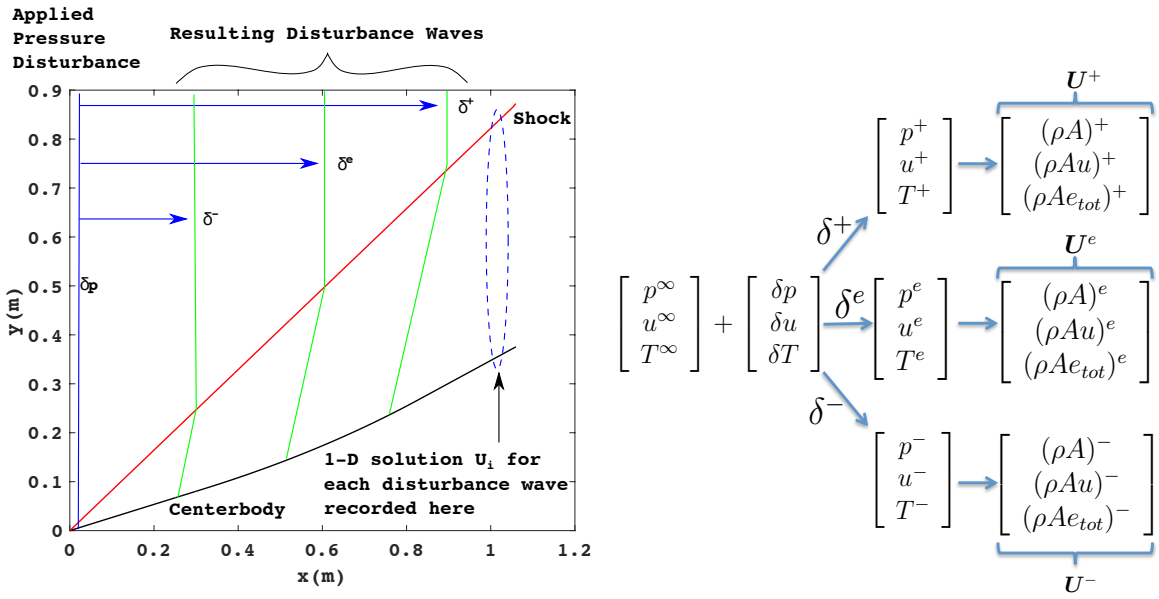

(a) Disturbances in solution field

(b) Flow variable decomposition

Figure 4.9: Decomposition of disturbance into separate 1-D steady states

the MOC, resulting in four overall MOC solutions for the entire flow field. The 1-D representation of at the plane of a given x-location i is then found using Equations (4.14)- (4.22) for each of these solution states which is represented by Equation (4.26). This process is illustrated in Figure 4.9.

$$\boldsymbol{U_i} = \left[\boldsymbol{U_i^{\infty}} \;\; \boldsymbol{U_i^{+}} \;\; \boldsymbol{U_i^{e}} \;\; \boldsymbol{U_i^{-}}\right] \tag{4.26}$$

However, this process only provides the temporary steady state solutions and not the full transient response. To accomplish this, the initial steady state solution is interpolated along streamlines placed at a constant inflow seed height Δy a seen in Figure 4.10(a). Then the streamlines are looped through and Equations (2.14) are used to determine the time that it takes each disturbance wave to be translated along a given streamline. The "j^{th}" stream line is then assigned a vector seen in Equation (4.27) which stores this information for each streamline that corresponds to the disturbance wave solutions in Equation (4.26).

$$\boldsymbol{\tau(j)} = \left[t_0 \;\; \tau^{+} \;\; \tau^{e} \;\; \tau^{-}\right] \tag{4.27}$$

Finally the solution to either a step or sinusoidal freesteam flow variable disturbance can be calculated by assuming that the 1-D representation of the flow field a given x-location i, transitions through each of the temporary steady state MOC solutions as the disturbance waves are propagated and distorted along the streamlines(Figure 4.10(a)). The process is as follows. First, the time for the entire simulation is set, which spans from $t = 0$ to $t >= T_f$, where T_f is the time it takes the slowest disturbance wave to travel the slowest streamline. Then a time step size is prescribed and the total number of time steps are looped through. At each time step the number of streamlines are looped through and the local steady solution is interpolated from Equation (4.26) using the time step and the current streamlines disturbance wave delay vector Equation (4.27). At a given x-location i, the plane normal to the axial direction is divided in N_r points and at each point the local solution is interpolated from the streamline solutions. Finally, the 1-D representation is determined using Equations (4.14)- (4.22) resulting in the full unsteady result at the plane of a given x-location $U_i(t)$.

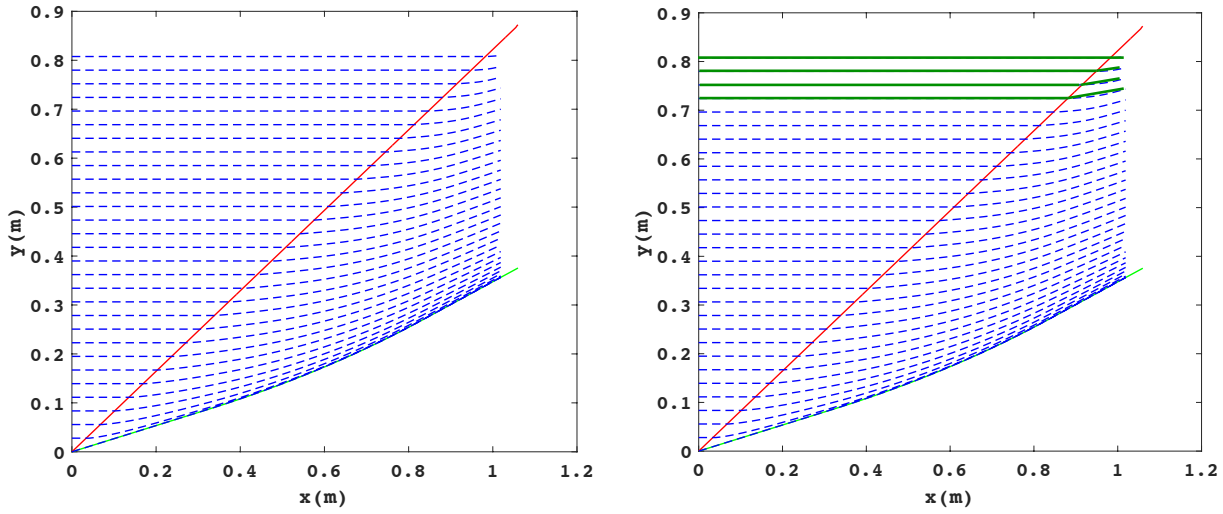

(a) Streamlines at initial steady state

(b) Example at time t_1

Figure 4.10: Streamlines in the solution field

For example, assume at some time t_1 the fast acoustic wave has arrived at the location labeled in Figure 4.9(a) along some streamlines but not others. This is seen in Figure 4.10(b),

where the green streamlines represents streamlines along which the fast acoustic wave has arrived at the chosen plane and the blue streamlines represent streamlines where it hasn't. At this time (t_1) the solution as a function of radial direction r can be represented in Equation (4.28).

$$\boldsymbol{U}(t_1, r) = \left[\boldsymbol{U^{SS}}(r_0), \boldsymbol{U^{SS}}(r_1), ..., \boldsymbol{U}^{+}(r_{Nr-1}), \boldsymbol{U}^{+}(r_{Nr})\right] \tag{4.28}$$

Here the green terms correspond to the steady state solution of the fast acoustic wave and the blue terms correspond to the initial unperturbed steady state solution. The current equivalent 1-D solution at the measured exit plane can be calculated from Equation (4.29). This process is repeated at every time step allowing the solution to capture the transient response of the external compression flow field.

$$\boldsymbol{U}(t_1) = \frac{1}{A}\int_A \boldsymbol{U}(t_1, r)dA \tag{4.29}$$

A similar process is used for sinusoidal free stream perturbations. In this case however, the response is the result of the superposition of three overlapping sine waves offset by their respective time delays. Again, the free stream flow variable is converted into the three principal disturbance waves and then converted into four separate steady state solutions. Here the time vector is set in the same way and the number of time steps and streamlines are looped over. At each time step, Equation (4.30) is used to find the response for each streamline. Here τ is the time delay associated with each wave and the amplitude results from the difference between the steady state of each wave. Each term is added after the current time step exceeds the time delay for a given disturbance. As with the step disturbance, the final result is obtained by taking the area integral average of all of the streamlines at the exit plane using Equation (4.29).

$$\begin{aligned}\boldsymbol{U}(t, r) = \boldsymbol{U}^{\infty}(t, r) &+ (\boldsymbol{U}^{+}(t, r) - \boldsymbol{U}^{\infty}(t, r))sin[2\pi f(t - \tau^{+})] \\ &+ (\boldsymbol{U}^{e}(t, r) - \boldsymbol{U}^{+}(t, r))sin[2\pi f(t - \tau^{e})] \\ &+ (\boldsymbol{U}^{-}(t, r) - \boldsymbol{U}^{e}(t, r))sin[2\pi f(t - \tau^{-})]\end{aligned} \tag{4.30}$$

Table 4.2: Temporary inflow conditions for each disturbance wave due to pressure disturbance

Inflow Variable	**Unperturbed Freestream**	**Fast Acoustic Wave δ^+**	**Entropy Wave δ^e**	**Slow Acoustic Wave δ^-**
M	1.7000	1.7020	1.7041	1.7000
P (Pa)	11597	11647	11647	11697
T (K)	216.65	216.92	216.38	216.65
u (m/s)	501.57	502.48	502.48	501.57

To test the effectiveness of the new dynamic external compression model, two tests were created. For both test cases, the steady state solution was first found at the cruise conditions seen in the second column of Table 4.2. In the first test a step input in pressure of 100 Pa was added to the steady state solution. Using the method just described, this perturbation is used to find three new temporary steady state solutions with the corresponding free stream inputs seen in Table 4.2. Using this method the dynamic response at the exit plan ($x = X_{CL}$) was calculated. To verify the accuracy of this method, the external compression model in PHASTA (Figure 3.23(a)) was run to steady state using the first column of Table 4.2 and was then perturbed with the same 100 Pa step in free stream pressure. The equivalent 1D representation was then recorded at a sampling frequency of 20,000 Hz using Equations (4.14)- (4.22). Figures 4.11(a), 4.11(b), and 4.11(c) compare the response in conservative flow variables (U_i) at the cowl lip location, between the PHASTA simulations and the new dynamic model. As can be seen from these figures the new method matches the results from PHASTA almost exactly. Not only is the amplitude of each wave predicted well but so is the transient response in between the arrival of each disturbance wave.

For sinusoidal disturbances, it is crucial that both of these features are captured. This is seen in the second test where the same steady state solution was perturbed using a 100 Pa amplitude, 500 Hz freestream pressure disturbance. In this case, the same temporary steady solution were used as in the previous test, as seen in Table 4.2, to determine the relative amplitudes of each wave expressed in Equation (4.30). Using the the new method, the response in conservative flow variables(U_i), is seen in Figures 4.12(a), 4.12(b), and 4.12(c). As with the previous case, the response is compared to PHASTA using the same steady state solution and sinusoidal pressure

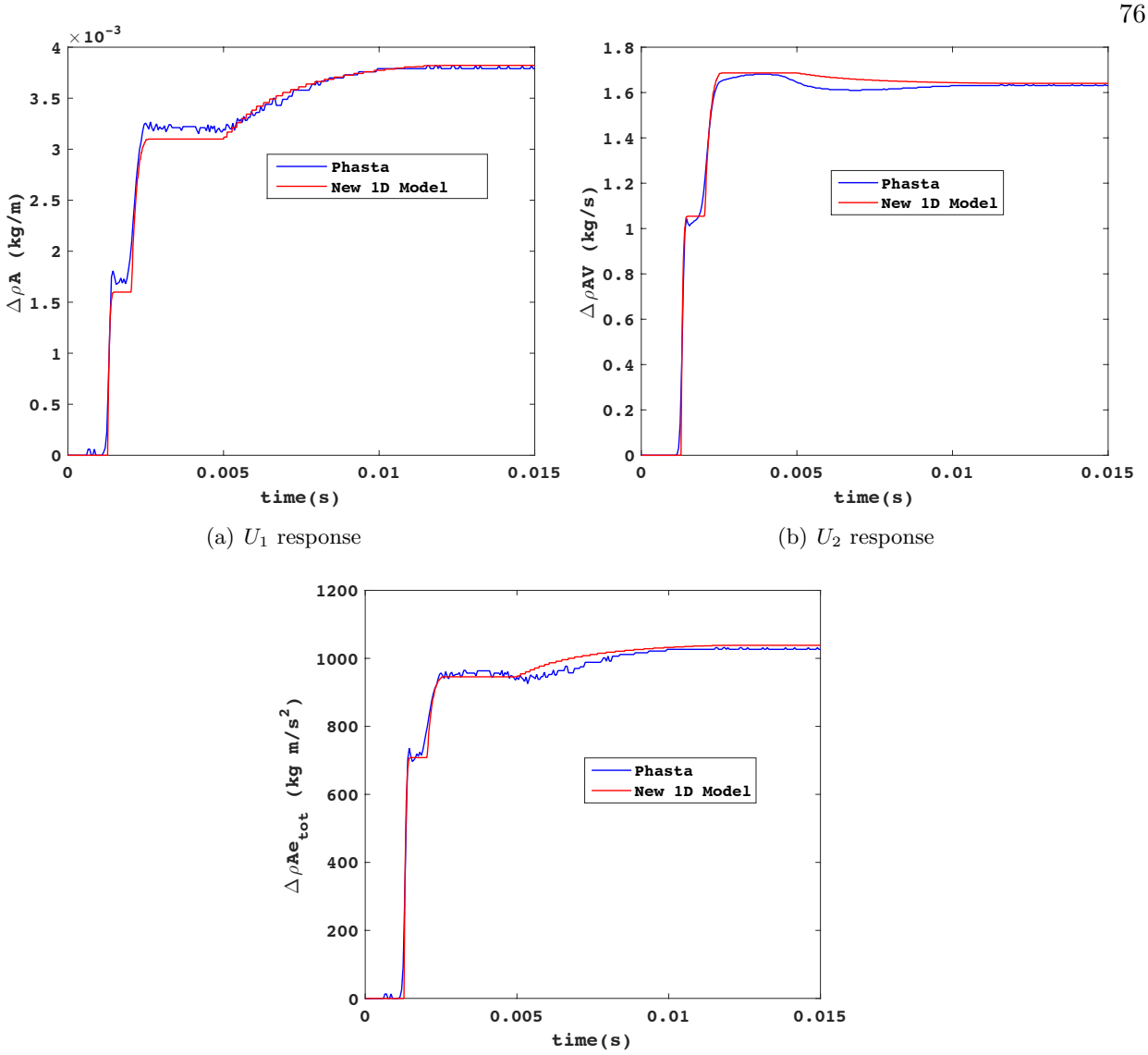

(a) U_1 response

(b) U_2 response

(c) U_3 response

Figure 4.11: Response to 100 Pa freestream pressure step

perturbation. From these figures, it can be seen that the new external compression dynamic model matches the PHASTA results almost exactly.

From these results and those of the previous test it is concluded that the new model is an accurate representation of the dynamics of the external compression flow field in response to low amplitude flow field perturbations. The formulation of this model is believed to be physically valid for the following reasons. First, in one dimensional flow it has been shown that single flow field

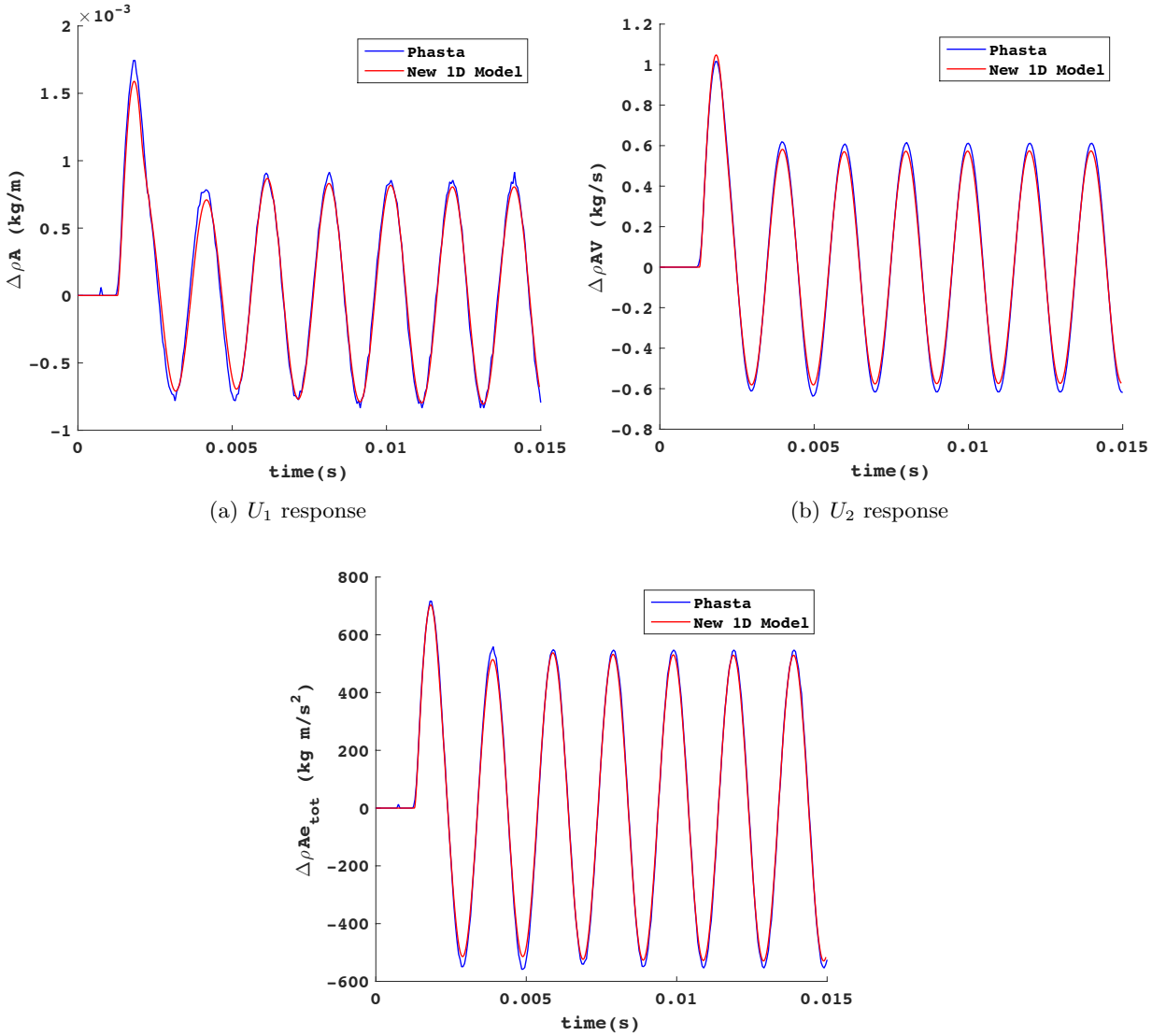

(a) U_1 response

(b) U_2 response

(c) U_3 response

Figure 4.12: Response to a 500 Hz, 100 Pa freestream pressure disturbance

perturbations create the three disturbance waves used in this modeling process to find the new temporary steady state solutions. Since the perturbation is applied at the free stream this portion of the flow field can be approximated as 1-D. Additionally, these waves are shown to propagate at $u + c$, u, and $u - c$ based on the local flow conditions. In the true three dimensional case, the disturbances will propagate along characteristic lines throughout the flow field, so that each portion of the disturbance wave actually spreads out in a fairly complicated manner. This is why

the individual probe points in Figure 3.23 in Section 3.4 show a similar behavior as the 1-D average and not three distinct steps as would be expected if the disturbances actually moved solely along streamlines. This method uses the approximation that the disturbances move along streamlines but in the 1-D case this is considered valid because we are interested in the average 1-D cross-sectional response of the flow field and this approximation is in fact a 1-D average of how these disturbances would propagate along characteristic lines. For this research the 1-D approximation is more valuable because if the disturbance waves were propagated along characteristic lines, as in the 3-D case, the method would essentially amount to an unsteady MOC formulation which would be much more computational expensive. In the end the 1-D average would be taken anyways, so there would be no advantage to doing this, especially considering how accurate the current method is. In the next section, this model will be combined with other methods discussed in the Background Section (2) to piece together a complete 1-D dynamic inlet model.

Chapter 5

Quasi 1-D External Compression Inlet Model

The main purpose of this research is to create a quasi 1-D external compression inlet in the Matlab environment. To reiterate, the inlet model should be accurate in both steady state and dynamic operation over a range of operating points spanning subcritical, critical, and supercritical operation. With the creation of the dynamic external compression model detailed in the previous chapter, it is now possible to discuss the overall inlet model. In this chapter the different modeling regions of the inlet model seen in Figure 2.17 will be discussed in detail. First, the external compression model will be slightly modified to accommodate a moving boundary between the external field and the internal duct modeling. This region is separated by the normal shock during critical and subcritical operation. In these situations the normal shock can move upstream and downstream and the inlet must capture this movement correctly. Next, the internal duct modeling which uses quasi 1-D CFD is detailed. This region is modeled using the MacCormack method as stated in the Background Section(2). Next, the cowl lip spillage model necessary for critical and subcritical operation will be discussed. Initially, the method from the LAPIN report discussed in Section 2 was used. As will be shown, this method was only able to be implemented for a specific operating point and was extremely unstable. To remedy this, a new method was created using data from the PHASTA simulations. Next, the exit boundary conditions used for this modeled will be discussed. The method detailed in Paynter is used and is compared to the original constant pressure boundary condition for accuracy. Finally, the results of the reduced order model will be compared to the PHASTA simulations. It will be shown this model matches PHASTA with very

low error for both steady state and dynamic operation for all of the operating points tested.

5.1 External Compression Flow Field

The external compression portion of the inlet is modeled using the method detailed in the previous section. To recap, this model use the MOC combined with a Taylor-Maccoll equation solve to determine the steady state solution of the flow field. Flow field disturbances are converted into characteristic disturbances waves which are used to create three new temporary steady state solutions. The unsteady solution is determined by assuming that the flow field transitions between these solutions along streamlines and the integral area average is taken at each time step at a prescribed location. In the previous section this was done at the end of the external compression flow field where the cowl lip or start of the internal duct is located. For supercritical operation this is accurate because the normal shock is located within the duct and the boundary between external compression flow field modeling and quasi 1-D CFD is at this location. However, for critical and subcritical operation the normal shock is located outside of the cowl lip. In these cases quasi 1-D CFD is used to model everything downstream of the normal shock the the external compression flow field must be used to find the equivalent 1-D solution upstream of the normal shock. For this reason, the external compression model was modified to have the equivalent 1-D state taken at equal spaced locations from the tip of the centerbody to the cowl lip region. The grid spacing of these locations is determined by the grid spacing of the internal duct domain.

With this modification, the external compression model can be incorporated into the overall inlet model. First the free stream Mach number (M_∞), pressure (P_∞), and temperature (T_∞) are prescribed and the initial steady state solution is determined using the MOC and the TM equation solver. Then, using the grid spacing determined by the internal duct model, the external compression flow field is reduced to an equivalent 1-D solution using Equations (4.14)- (4.22) from the freestream to the cowl lip location. This solution is then saved so that future simulations at these conditions do not require the flow field to be solved again. A benefit of the completely supersonic flow field is that the downstream flow field in the internal duct does not the affect the

solution so it can be used in any simulation under these conditions. Next, if a flow field perturbation is applied, it is converted into the three characteristic disturbance waves DELS. The MOC is used to determine the steady solutions for each wave and the equivalent 1-D solution is determined for each location from the freestream to the cowl lip location. Again, this solution is saved for possible future simulations because regardless of the perturbation type or frequency, these disturbance wave solutions can be reused to save computational expense. Finally the specific perturbation type(step or sinusoidal) is solved for using the methods described in the previous section. This results in the entire solution for the external compression flow field (expressed as $U_i^E(x,t)$) independent of the internal duct solution which will be described in the following section. This decoupling of solutions is again possible because internal duct flow field does not affect the upstream solution in the purely supersonic external compression flow field.

5.2 Internal Duct Modeling

The internal duct portion of the supersonic inlet is modeled using quasi 1-D CFD. The domain spans either the cowl lip location or the normal shock to compressor face depending on operating condition. As mentioned in the Background Section (2), if it is assumed that the flow is quasi one dimensional, an ideal gas, inviscid, and has no external heat sources, then the quasi 1-D CFD Equations (2.9), (2.10), (2.11), and (2.12) can be used to model this portion of the inlet. The method used to solve these equations is the MacCormack method. The method was briefly discussed in the Background Section (2) and a full derivation of the method will be skipped here. What is contained here is how the internal duct model fits into the overall model and what modifications were made to it. Following this, the initial results of the internal duct modeling will be shown as compared to the results from PHASTA.

Under supercritical operation, the internal duct portion of the inlet spans the cowl lip region to the compressor face. The upstream boundary conditions are taken from the last cell of the external compression flow at the cowl lip and the downstream boundary conditions are are applied as to best emulate the compressor face (more detail here in Section 5.4). The time step used

is determined from the applied grid spacing dx and using a CFL number of 0.2026. The initial conditions used to start the simulation are taken either from the equivalent 1-D representation of PHASTA data at steady state using Equations (4.14)- (4.22) or from the final time step of a previous solution. From here the total number of time steps is looped over using the MacCormack method as is consistent with Anderson [5]. For supercritical operation, nothing more is needed and the internal duct solution can be solved for$(U_i^I(x,t))$. The domain split for this situation is seen in Figure 5.1(a).

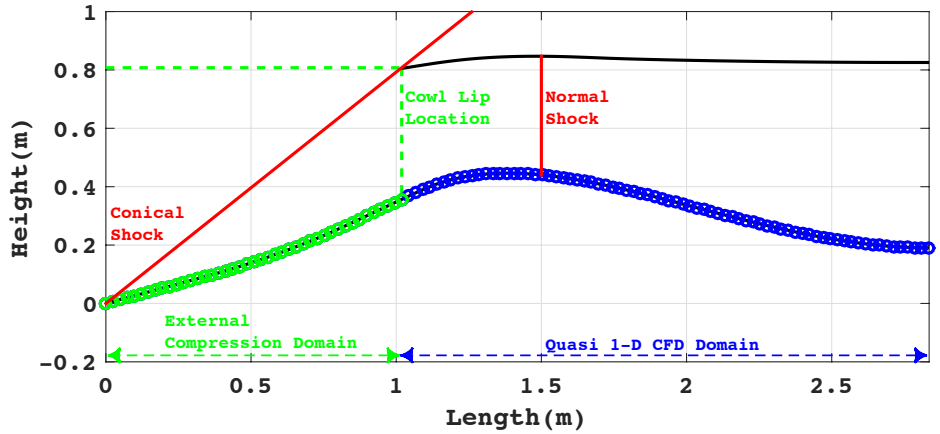

(a) Supercritical Operation

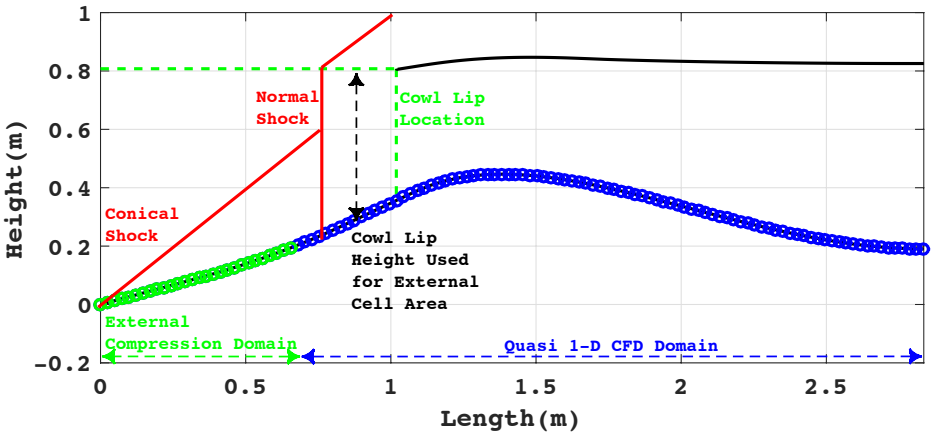

(b) Subcritical Operation

Figure 5.1: External compression and quasi 1-D CFD domains

For critical and subcritical operation however, the normal shock wave is expelled from the inlet and the MacCormack method must be modified to account for the domain moving upstream

with the shock. As the back pressure at the compressor face is raised the normal shock moves upstream to adjust to the flow field. Once, the normal shock reaches the cowl lip the domain must be extended to allow it to keep moving freely. This is done by extending the CFD domain upstream by 4 cells as seen in Figure 5.1(b) for subcritical operation. The area used for each new cell is taken from the difference in height between the cowl lip and the centerbody, also seen in Figure 5.1(b). At each time step the shock position is determined from Equation (5.1) by looping through the solution field in x.

$$x_{Shock} = max\left(\frac{\partial P(x)}{\partial x} \bullet \frac{\partial M(x)}{\partial x}\right) \tag{5.1}$$

Here, the max is taken as the combined max gradient of the Mach number and pressure, where the gradients are evaluated using the central difference method. At each time step, the upstream boundary is moved to allow proper shock motion. At this point the total solution is updated as $U_i(x,t) = [U_i^E(x,t), U_i^I(x,t)]$. This procedure works because the external compression flow field has already been solved for the total time of the simulation. Likewise, if the shock moves downstream, the previous internal duct cell is converted back to an external compression cell using the pre-calculated value at that time step.

Table 5.1: Boundary conditions from PHASTA for the internal duct test

Boundary Type	**Boundary Condition**
$P_{CowlLip}$	24,349(Pa)
$u_{CowlLip}$	430.84(m/s)
$T_{CowlLip}$	249.24(K)
P_B	45,930(Pa)

To test the accuracy of the MacCormack method to simulate the internal duct portion of the inlet independent of the inlet model, it was compared to the PHASTA data at the supercritical operating point seen in Figure 3.12(a) in Section 3.2. To do this, the PHASTA data at the cowl lip was used as the upstream boundary conditions for the internal duct and the same constant pressure was used at the exit boundary conditions as seen in Table 5.1. The results of this test are seen in

Figure 5.2(a). These results are presented in non-dimensional form using the max value for each flow variable to non-dimensionalize the data. As can be seen here the results match very closely including the normal shock position.

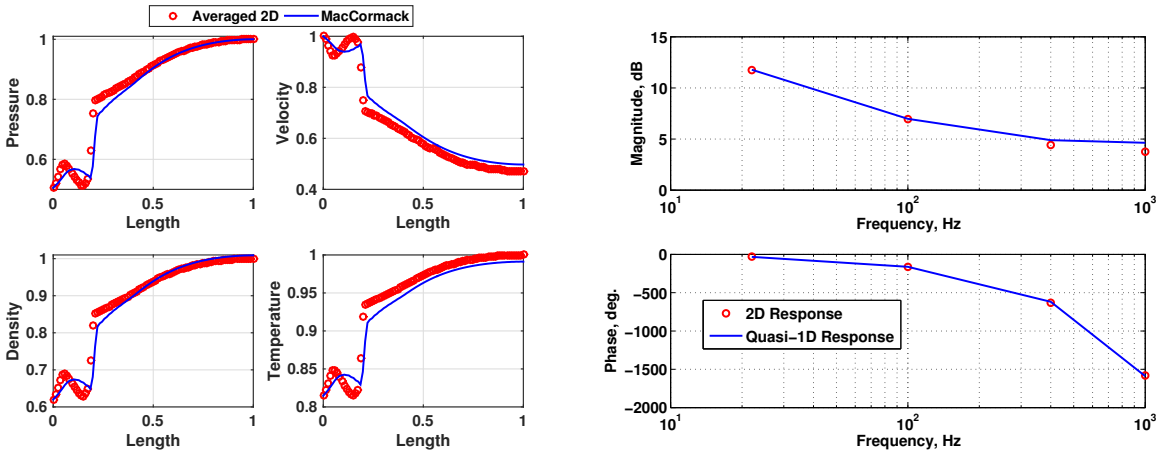

(a) Steady state

(b) Response to 100 Pa pressure perturbation

Figure 5.2: Internal Duct Comparison(Connolly [15])

From here the dynamic response of the internal duct to upstream perturbations was tested. As before the data from PHASTA was used to determine the upstream boundary conditions at the cowl lip location and the same exit pressure was used as a downstream boundary condition. The PHASTA data came from the supercritical pressure perturbation tests in Section 3.3 using freestream perturbations with a 100 Pa amplitude sinusoidal disturbance at frequencies of f = [10, 100, 400, 1000] Hz. In Figure 5.2(b), the dynamic response of the internal duct and PHASTA are displayed in the form of a Bode plot. As can be seen, the dynamic response of the internal duct is almost exactly the same as PHASTA both in gain and frequency response. With these results it is concluded that the internal duct is modeled correctly using the MacCormack method.

5.3 Cowl Lip Spillage

In Section 5.2 the MacCormack method was modified to allow the quasi 1-D CFD domain to change as the normal shock moved under sub-critical and critical operation. For these operating

points, an additional modification is needed to account for the mass flow spillage around the cowl region. This can be seen in Figure 3.14 in Section 3.2 where the flow is spilling out around the cowl lip after the normal shock. In Figure 5.1(b) the domain for the external compression field was defined by the centerbody and the cowl lip height. To account for this flow spillage, extra terms must be added to the quasi 1-D equations ((2.9), (2.10), and (2.11)) as seen in Equations (5.2), (5.3), and (5.4).

Continuity:

$$\frac{\partial}{\partial t}(\rho A) + \frac{\partial}{\partial x}(\rho A u_x) = S1_{Spill} \tag{5.2}$$

Momentum:

$$\frac{\partial}{\partial t}(\rho A u_x) + \frac{\partial}{\partial x}\left(\rho A u_x^2\right) = -A\frac{\partial p}{\partial x} + S2_{Spill} \tag{5.3}$$

Energy:

$$\frac{\partial}{\partial t}(\rho A E_{tot}) + \frac{\partial}{\partial x}(\rho A u_x H_{tot}) = -p\frac{\partial A}{\partial t} + S3_{Spill} \tag{5.4}$$

Here each Si_{Spill} term represents the amount of mass, momentum, and energy that leaves the domain. In the vector representation of the conservation equations (Equation (2.13)) this can be expressed as Equation (5.5).

$$\boldsymbol{U_{,t}} + \boldsymbol{F_{,x}} = \boldsymbol{S} + \boldsymbol{S_{Spill}} \tag{5.5}$$

These terms are needed for two reasons. First, without them the flow values downstream of the normal shock and at the compressor face will be in accurate. This is unacceptable both for taking meaningful results from the inlet model and when combining the inlet with the rest of engine as part of a much larger simulation. Therefore simply locking the shock wave at a known location for a given back pressure is not an option. The second reason, is that without these terms the solution becomes unstable. This happens because as the normal shock is expelled from the internal duct, it keeps moving upstream towards the centerbody causing the solution to crash because there is no pressure relief to match the applied boundary conditions. To solve this issue, two method

are presented. The first is the method from the LAPIN report which was detailed in Section 2. This method ended up being accurate for only a single operating condition so it was ultimately abandoned. A brief summary method is still presented however because considerable progress was made in getting it to work correctly and future research could potentially make it more general. This is the ideal situation because then the inlet model would be completely independent of outside data, either from CFD simulations or test data. The second method, which was implemented in the final inlet model, uses data from the PHASTA simulations to determine these spillage terms. As will be seen, this method works extremely well. It is able to predict the correct shock location while maintaining low steady state error and was found to be robust for the cruise condition at which it was applied.

The method in the LAPIN report was detailed in Section 2. There it was shown that the method predicts the mass flow spillage around the cowl lip by modifying a previous method by Moeckel [41]. In Moeckel, a method for determining the mass spillage around a pitot tube using a correction factor F, based on the known theoretical supersonic flow around a cylinder was developed. In LAPIN, this method was modified using the conditions upstream of the normal shock and the conditions at the cowl lip during the upstart condition for a mixed compression inlet to create a new set of correction factors Fc_i. In applying this method for the research contained here, it was found that the original correction factor F reported in the LAPIN report had an error. The first step in using this method was to follow the original paper by Moeckel and create a function to correctly predict this correction factor as a function of pre-shock Mach number. For brevity, the details are left out of this thesis and can be found in Moeckel. From here one correction factor was calculated for each conservation equation spillage term as described in the LAPIN report. The spillage term for the continuity equation was determined using Equations (2.8) and (2.7) and analogous terms were found for the momentum and energy equations by replacing the ρU terms with ρU^2 and $\rho U e_{tot}$ respectively. Here the correction terms were applied to the local conservation terms U_i isentropically expanded to the sonic condition. These spillage terms were then added to the quasi 1-D equations seen in Equations (5.2), (5.3), and (5.4) and incorporated into the MacCormack

method.

Initially, this method did not work and the normal shock moved to the free stream, as in the case without spillage terms, and the solution became unstable. It was found that if limits were placed on the correction factors Fc_i, seen in Table 5.2, then a stable solution was able to be found. At a back pressure of $47,119(Pa)$ or $1.017P_{B(Critical)}$ and using the cruise freestream conditions seen in Table 3.4, the LAPIN spillage method allowed the inlet to match the data from PHASTA very closely as seen in Figure 5.3. Here the shock location is off by only 2 cells and the steady state pressure error at the compressor face is 0.891%, with similar results for the other flow variables. However, although a stable solution was found for several operating points using these limits, an accurate solution was only able to be produced for this single sub-critical operating point. At other operating conditions there were large errors in the steady state solution on the order of 50%. An attempt was made to scale the limits with the back pressure but without success. Ultimately, this would not be a good solution as the method would then lose generality.

Table 5.2: LAPIN correction factor limits

Correction Factor	Limits
Continuity Fc_1	[0.50, 0.74]
Momentum Fc_2	[0.50, 0.75]
Energy Fc_3	[0.99, 1.00]

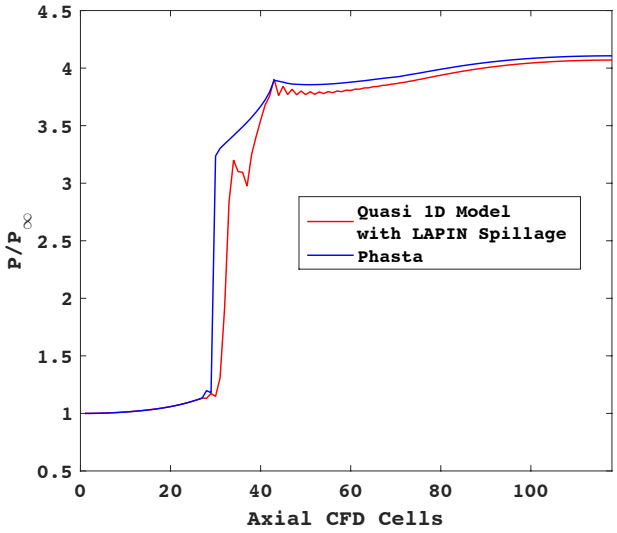

Figure 5.3: Steady state pressure using LAPIN spillage model

These results show that it may be possible to use this method in the future with modification. It is also possible that this may have been considered a success for the purposes of the LAPIN

report. In that report the model used was a mixed compression inlet and their main concern was inlet upstart. For mixed compression inlets the design point is at the supercritical operating with the normal shock inside the duct. It may have been that the authors were only concerned with a single upstart or sub-critical operating point since it is an off design consideration. In that case it would make sense not to test the model at several sub-critical operating conditions for accuracy. For this research, this functionality does not suffice and so it was not used in the final model.

As a result of the limitations of the LAPIN method, a new spillage model was created using the data from PHASTA simulations. In this method, the 1-D solution was extracted from PHASTA simulations at four sub-critical operating points. Here, the equivalent 1-D solution is taken at equally spaced locations from the freestream to the cowl lip, using Equations (4.14)-(4.22) and the cowl lip height to determine the area of each cell as seen in Figure 5.1(b). At steady state, the unsteady term in Equation(5.5) $\boldsymbol{U_{,t}}$ is zero and the equation can be reduced to Equation(5.6).

$$\boldsymbol{F_{,x}} = \boldsymbol{S} + \boldsymbol{S_{Spill}} \tag{5.6}$$

Here the flux term $F_{,x}$ can be approximated using the central difference method and the spillage terms can be solved for using Equation(5.7).

$$\boldsymbol{S_{Spill}} = \frac{\boldsymbol{F_{i+1}} - \boldsymbol{F_{i-1}}}{2\Delta x} - \boldsymbol{S} \tag{5.7}$$

At each operating point the normal shock position is also known, so the spillage terms at each location x of the external compression portion of the inlet can be correlated with the shock position. Using this data the spillage terms were curve fit as function of shock position using linear interpolation. In this way the inlet adjusts naturally as the shock moves out of the inlet. This method was successful in predicting both the shock position and flow field down stream of the normal shock. The results will be shown in the final section of this chapter. The main benefit of this method is that it is robust at this freestream condition allowing the flow field to adjust properly to changes in back pressure. The downside is that the model is dependent on PHASTA data and

so this model most likely will not work at different freestream conditions. Fortunately, only steady state CFD data is needed so generalizing this inlet to work at different parts of the flight envelope would require only a modest number of additional CFD simulations.

5.4 Exit Boundary Conditions

For all of the simulations performed so far, the applied exit boundary condition has been a constant back pressure. In Section 2 this was shown to be an accurate boundary condition for steady state but not the most accurate when studying the unsteady response of an inlet. In Section 2 a method was presented by Paynter et. al. [45] to properly model the effects of a compressor face as the exit boundary condition in a quasi 1-D CFD model. To briefly reiterate, this method linearizes the 1-D Euler equations along characteristic lines to develop boundary conditions based purely on a refection parameter R. The reflection parameter can be used to set constant pressure, constant velocity, nonreflecting, or realistic boundary conditions based off of the compressor blade stagger angle. In this section, the capability of this model is tested using different values of the reflection parameter R to set the exit boundary condition. For the final results presented in this thesis, which verify the accuracy of the inlet using the results from PHASTA, a constant pressure boundary condition is still used because that was the boundary condition used in the PHASTA simulations. The purpose here is to show this capability has been added to the quasi 1-D inlet model for future studies when the compressor face blade geometry is known.

To test the capability of the new exit boundary condition model a test was developed. First the quasi 1-D inlet model was run to steady state at the supercritical operating condition using a back pressure $45,089(Pa)$ or $0.972P_{B(Critical)}$ and the freestream conditions seen in Table 3.4. A step in pressure of 100 Pa was applied to the freestream and measured at a point 0.291 m in front of the exit plane. As with the PHASTA simulations a 3m straight duct was added to the end of the inlet. For this test, this straight section eliminates the affects of changes in area to better analyze the properties of the reflected disturbance. This test was performed on the inlet using the original constant pressure exit boundary conditions along with the constant pressure($R = -1$) and constant

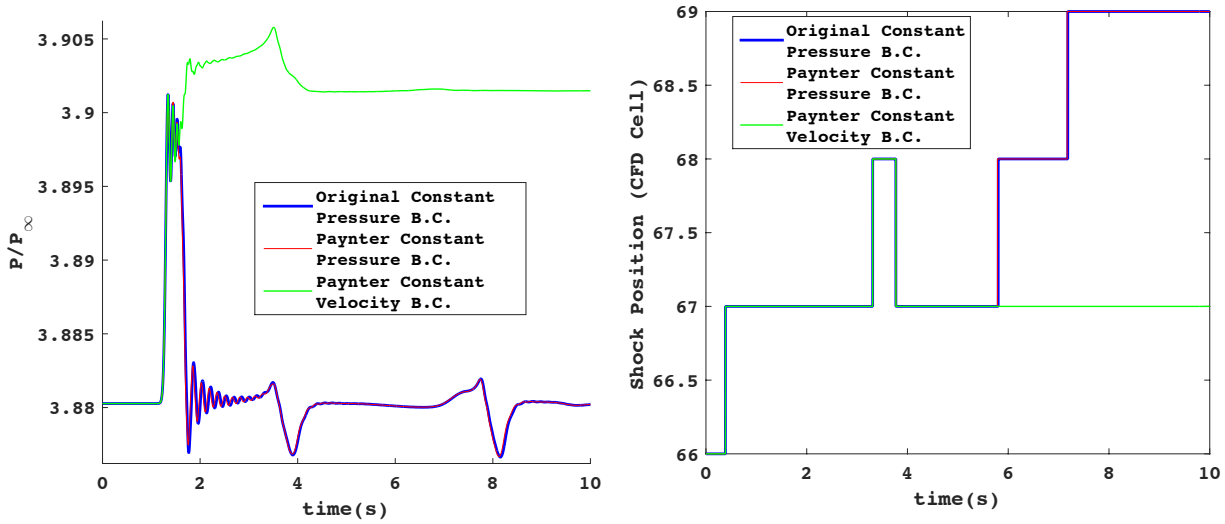

(a) Pressure response

(b) Shock position

Figure 5.4: Response upstream of exit boundary to freestream pressure step

velocity($R = 1$) boundary conditions using the Paynter model. In Figures 5.4(a) and 5.4(b) the results are presented as the response in pressure at measured location and the change in shock position respectively. in Figure 5.4(a) it seen that the initial wave is the same in all three cases but the reflected wave is greatly affected the choice of boundary condition. As can be seen in Figures 5.4, the results using the constant pressure boundary condition with the Paynter method exactly matches the original constant pressure boundary condition both in the reflected pressure wave and the affect on shock movement. Additionally, the behavior of the reflected pressure wave using the constant velocity boundary condition with the Paynter method matches the qualitative response seen in Paynter et. al. [45]. Namely that the reflected pressure wave has a positive amplitude above the mean pressure at that location. From these results it is concluded that the boundary condition method is working properly. Future simulations will use the correct boundary condition when the blade geometry is known.

5.5 Implementation of the Quasi 1-D Inlet Model in Matlab

As mentioned, the quasi 1D inlet model has been developed completely in the Matlab environment. The current version is written as a Matlab script with future plans to convert the code to a hybrid Matlab/Simulink model to interface more easily with the rest of the engine/vehicle model. The model was developed as a modification of a previous model which used the MacCormack method to model the internal duct portion of the inlet and data from separate CFD simulations to model the external portion of the inlet. The main contributions to the quasi 1-D inlet model are the dynamic external compression model detailed in Section 4 and the mass spillage model detailed in Section 5.3. The dynamic external compression model is run before the internal duct portion while the mass spillage model was integrated into the internal duct model and is called at each time step.

At the beginning of the quasi 1-D inlet model code, the geometry of the inlet and as well as the initial conditions are loaded. The geometry file includes points in x and y that locate the centerbody and the cowl surface of the inlet. The initial conditions provide the area averaged 1-D state and either come from an externally run CFD simulation, test data, or a previously run quasi 1-D inlet solution. Note, it is necessary to start from a previously run steady state file if a freestream disturbance is to be applied. From here, the parameters of the simulation are set, such as the total number of time steps, the CFL number, etc. Next, the steady state solution to the external compression portion of the inlet is obtained using the Method of Characteristics (MOC). The MOC solution can either be run, if using a new set of free stream values, or loaded from a previous solution. From here, if necessary, a disturbance is applied to the freestream. As mentioned in Section 4, the dynamic model is obtained by transitioning between three temporary steady state solutions caused be the subsequent disturbance waves, created by the free stream flow disturbance. These temporary states are based on the amplitude of the change in free stream values. Additionally, these temporary states are calculated using the MOC, like the original steady state solution, and is the most computational expensive portion of the external compression model.

For this reason, an option exists to save these states so that any subsequent simulations using the same magnitude disturbance will not have to repeat this step. For instance, if a 1 % change in pressure is applied as a step disturbance, the resulting temporary steady state solutions will be the same as is if a 100Hz 1% amplitude change in pressure sinusoidal disturbance was applied. From here, the type of applied disturbance is selected (step or sinusoidal wave) and the solution for the total number of time steps of the simulations is obtained for the external compression portion of the inlet. As mentioned in Section 4, this is possible because the flow is supersonic throughout this region and the external compression portion can be decoupled from the internal duct.

With this solution obtained, the internal duct portion of the code is run. The total number of time steps and the total number of points x in the streetwise direction are looped though and the MacCormack method is used to solve the internal duct portion of the inlet. At each time step the amount of spillage needed at the cowl lip is applied using the current normal shock position and the data from the PHASTA simulations. If the normal shock is inside of the duct then, then these spillage terms are not applied. Finally, at each time step, the solution data from the external compression model is used as an upstream boundary condition and the Paynter model is used for the exit boundary conditions. When the simulation is complete, the flow field data for each point x and for every time step is output to the Matlab work space. This process is summarized in the following pseudo code.

Algorithm 1 Quasi 1D Inlet Code

```
procedure Initialize Simulation
    Load geometry
    Load initial conditions
    Set simulation parameters(Δt, Δx, t, etc)
procedure External Compression Flow Field
    if New simulation = True then
        Determine steady state with MOC
    else
        Load steady state solution
    end if
    if Apply freestream disturbance = True then
        if Apply new disturbance = True then
            Calculate three temporary steady state solutions for resulting disturbance waves.
        else
            Load temporary steady state solutions
        end if
        Enter disturbance type (step or sinusoidal wave)
        Calculate dynamic response for the total length of the simulation.
    end if
procedure Internal Duct
    for Δt = 1 to t do
        Apply upstream BCs using external compression solution
        for Δx = 1 to L do
            Apply MacCormacks method
            Apply spillage where needed
        end for
        Apply downstream BCs using Paynter method
    end for
```

5.6 Steady State and Dynamic Results of the Quasi 1-D Inlet Model

With all of the individual sections of the quasi 1-D inlet model verified, it is now possible to simulate the entire inlet model. In the final version of the inlet model, the external compression portion of the inlet is modeled using a novel approach developed in Section 4, the internal duct portion is model using the MacCormack method, modified to allow a moving upstream boundary, the cowl lip spillage is modeled using a new approach developed in Section 5.3, and the exit boundary conditions are modeled using the method developed by Paynter, et. al. To verify the accuracy of the complete inlet model, results have been obtained and compared to the previous PHASTA results seen in Sections 3.2 and 3.3. These results have been obtained at both steady state and dynamically, at several operating point at the cruise freestream conditions. From these results, it will be shown that the reduced order model is an accurate representation of the inlet.

The first step in verifying the complete inlet model was to test its capability to model the inlet at steady state. To do this, the inlet was simulated at the freestream using the inflow boundary conditions seen in Table 3.4 and at the operating conditions seen in Table3.5. For each simulation, the back pressures in this table were applied as the exit boundary condition. Figures 5.5-5.9 show the pressure distribution from freestream to the compressor face location. In each of these figures it can be seen that both the steady state solution and the shock match the PHASTA results extremely well.

In particular, the error in the external compression portion is very low, at less than 1% in every simulation. The max error for every flow variable in each simulation is less the 5% and the max error for every flow variable at the compressor face location is less the 1.7% and less than 1% in most cases. The shock position is only off in two cases but matches PHASTA in all of the other instances. Once, at a supercritical operating point ($P_B = 0.989 P_{B(Critical)}$) and again at the critical operating point. The fact that the shock is spread out over more CFD cells than in PHASTA is due to the artificial viscosity used in the MacCormack method. The pressure distribution plots from Figures 5.5-5.9 are shown in Figures 5.10-5.14 to better illustrate the shock location comparison

between the two models. Additionally, the cowl lip spillage model does an excellent job modeling the spillage and allowing the inlet to operate at the subcritical operating conditions. Compared to the results using the spillage model from LAPIN seen in Figure 5.3, this is a large improvement. These results show that the reduced order model accurately models the inlet at steady state.

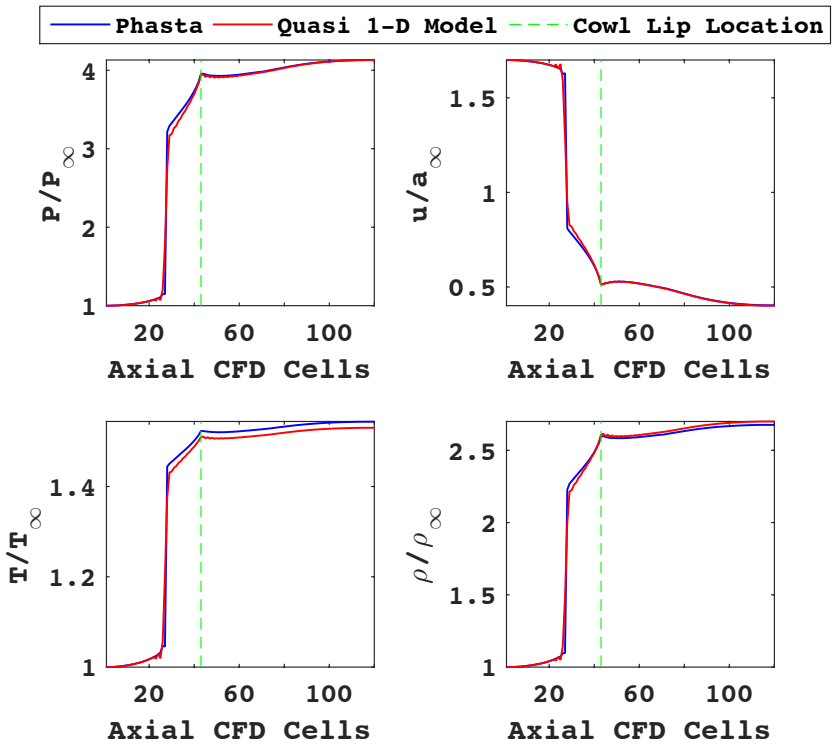

Figure 5.5: Steady state results $P_B = 1.023 P_{(Critical)}$

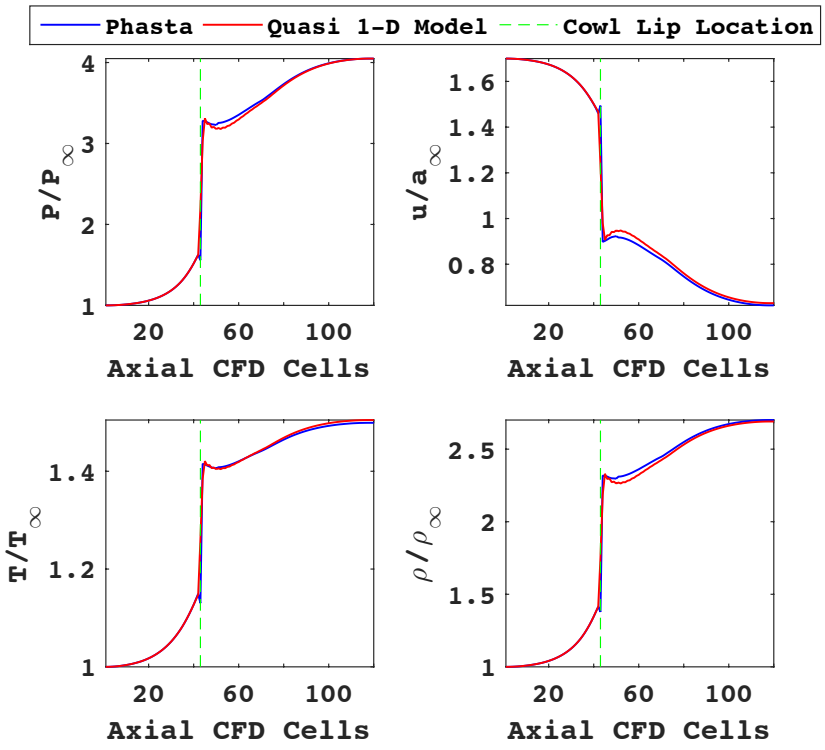

Figure 5.6: Steady state results $P_B = 1.012 P_{(Critical)}$

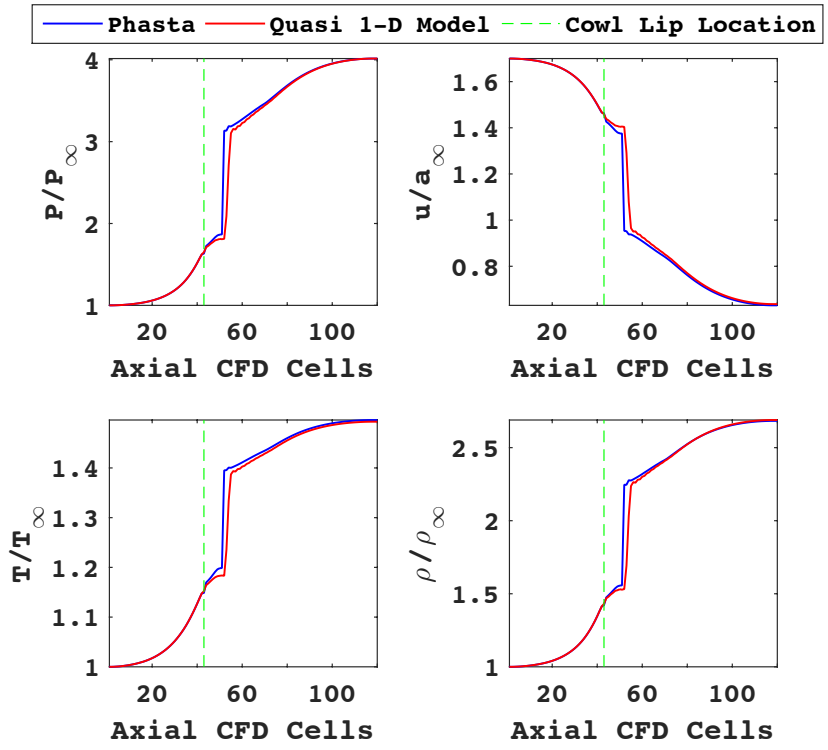

Figure 5.7: Steady state results $P_B = 1.000 P_{(Critical)}$

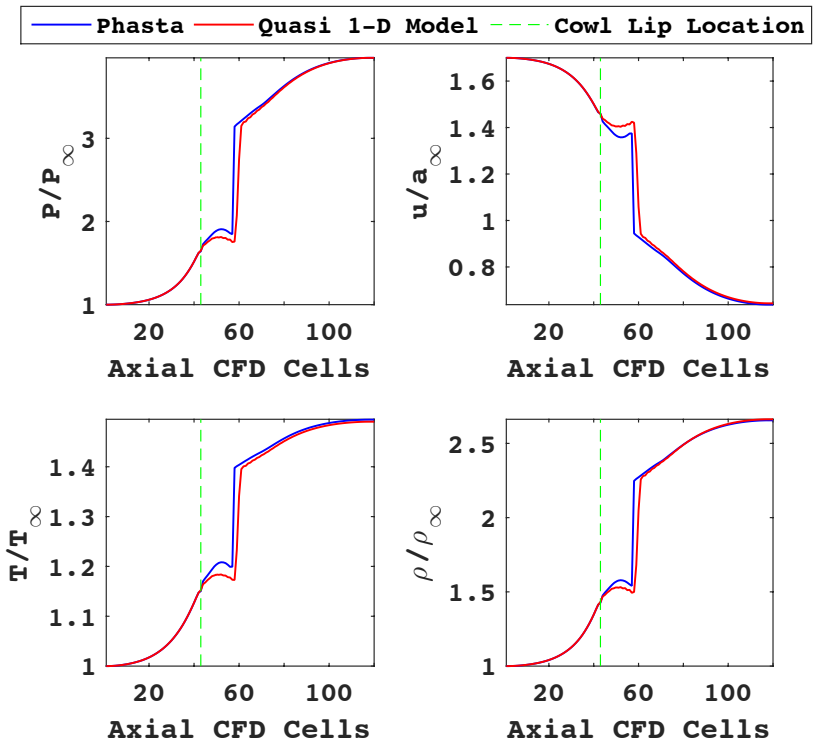

Figure 5.8: Steady state results $P_B = 0.989 P_{(Critical)}$

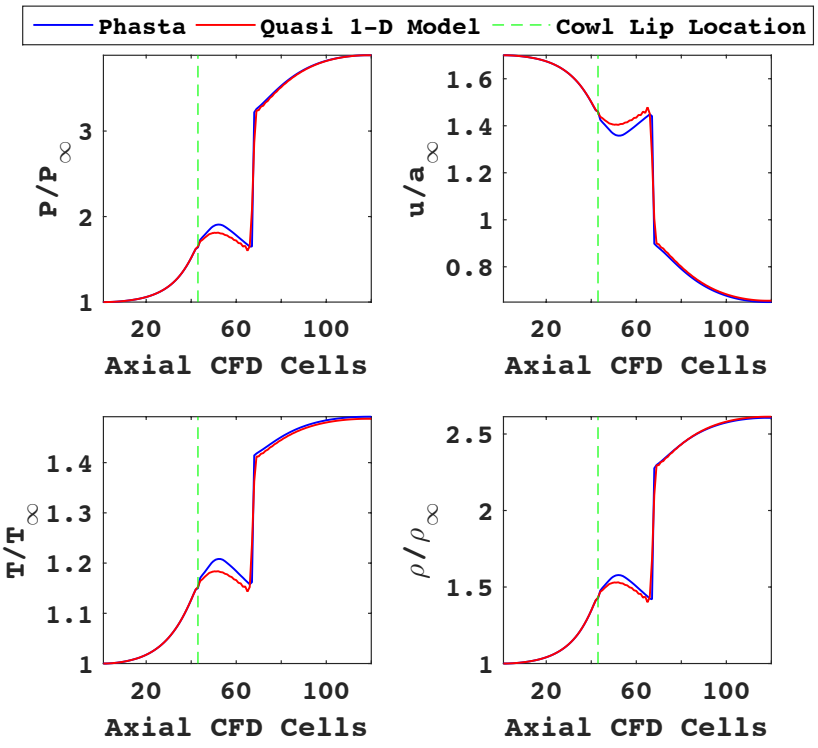

Figure 5.9: Steady state results $P_B = 0.972 P_{(Critical)}$

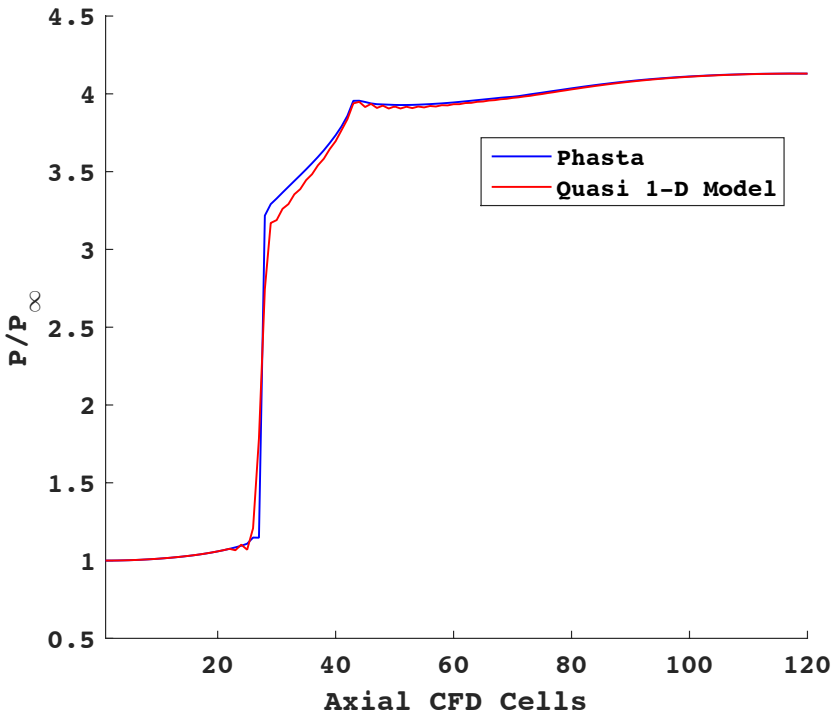

Figure 5.10: Steady state pressure distribution $P_B = 1.023 P_{(Critical)}$

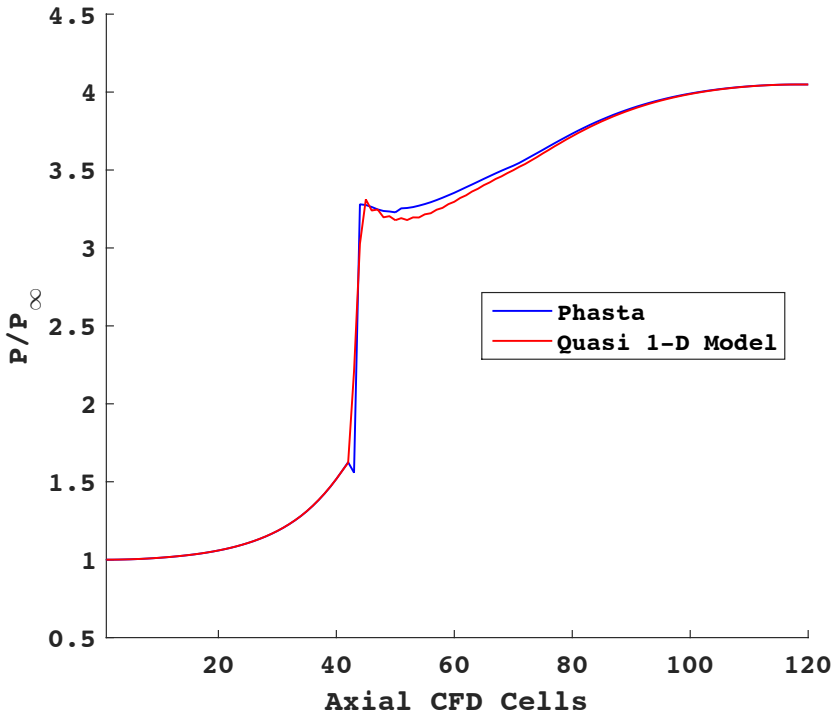

Figure 5.11: Steady state pressure distribution $P_B = 1.012 P_{(Critical)}$

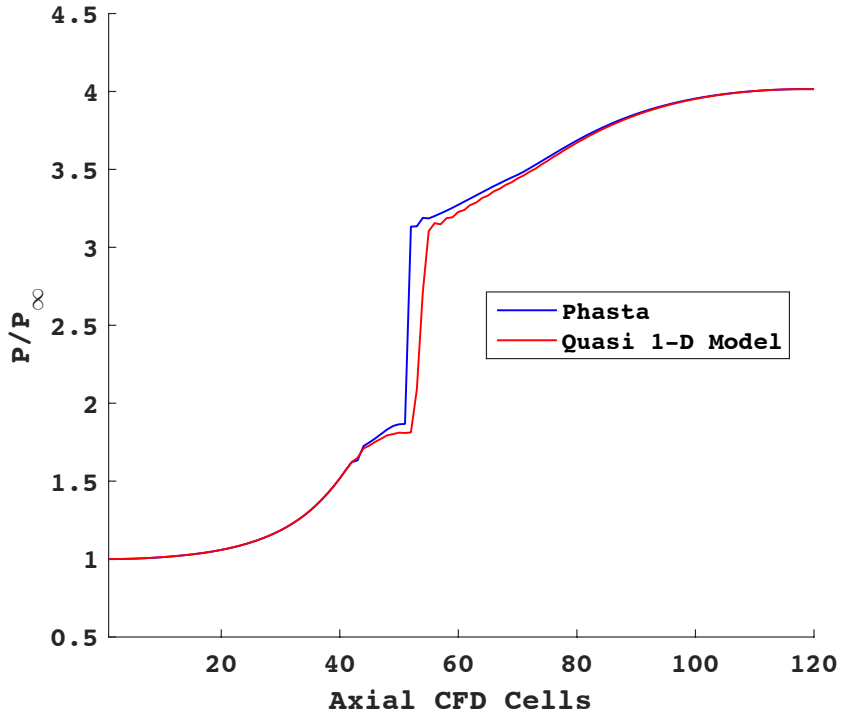

Figure 5.12: Steady state pressure distribution $P_B = 1.000 P_{(Critical)}$

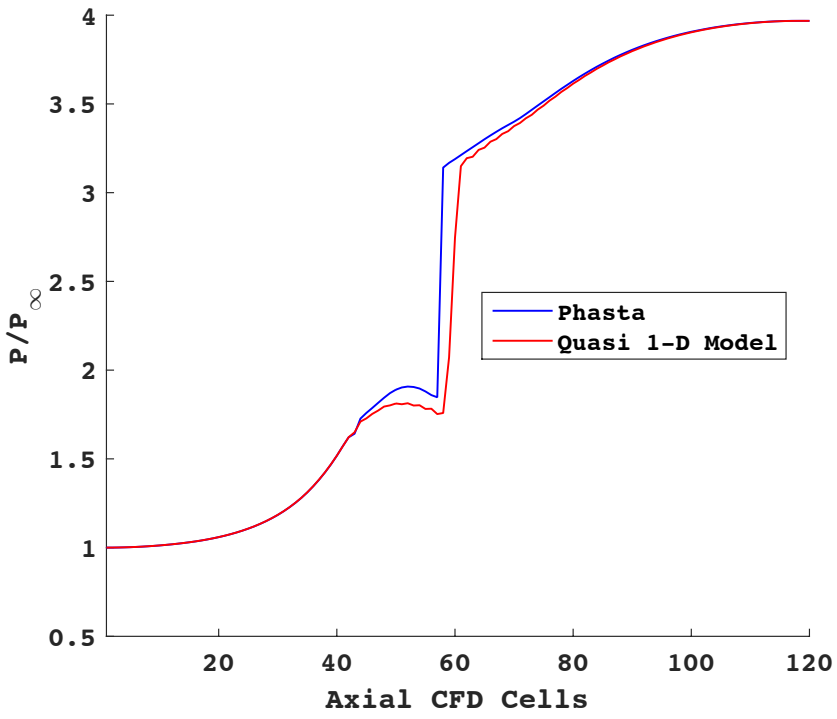

Figure 5.13: Steady state pressure distribution $P_B = 0.989 P_{(Critical)}$

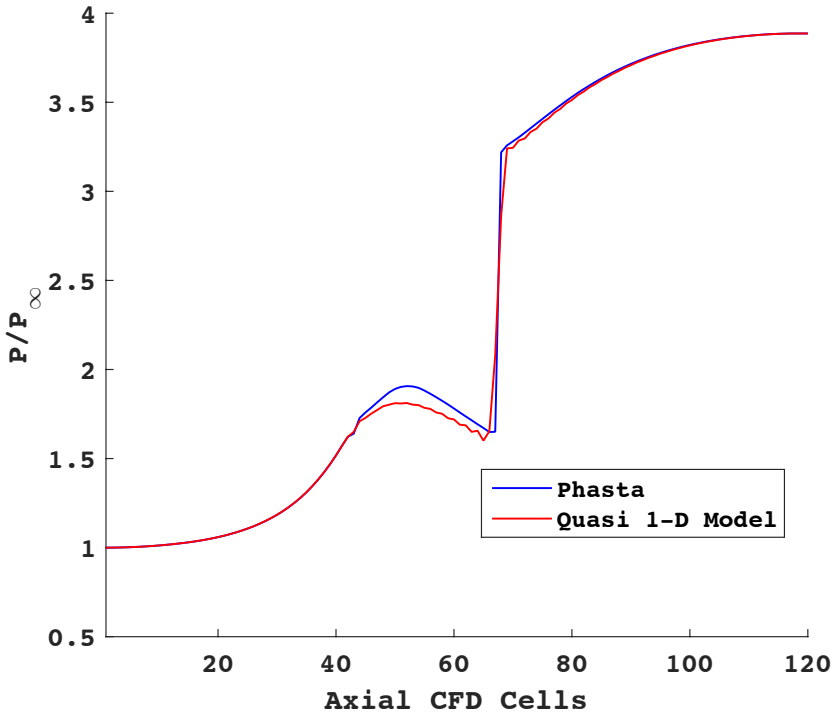

Figure 5.14: Steady state pressure distribution $P_B = 0.972P_{(Critical)}$

The final test in verifying the complete inlet model was to test its capability at handling freestream perturbations. For each of the operating points in the steady state tests, the freestream was perturbed with a 100 Pa amplitude sinusoidal pressure disturbance at multiple frequencies. In Figures 5.15-5.19, the response to 100 Hz free stream perturbation is measured at the compressor face. Here, the y-axis variable ΔP is the difference in the measured response in pressure due to the perturbation and the steady state value. The response is only shown to ~ 0.025s because after this time, the slow acoustic wave which is reflected off of the exit boundary arrives at the compressor location and interferes with the solution making it difficult to compare to PHASTA. This test was repeated for select frequencies between 50-1000 Hz for all of the operating conditions except the supercritical operating point ($P_B = 0.989P_{B(Critical)}$) as seen in Figures 5.20,5.21,5.22, and 5.24. In the supercritical case, frequencies between 50-2500Hz were chosen to compare with the extra data from PHASTA which is shown in Figure 5.23. As can be seen from these plots, the reduced order model matches both the gain and frequency results from PHASTA extremely well at each

operating point tested. However, the reduced order model does seem to lose some accuracy at higher frequencies. This may be due to the grid size of the internal duct portion of the 1-D model. Part of the reason the results match so well is because of the accuracy of the external compression model. As was seen in Section 3.1, the measured amplitude of an applied pressure perturbation in a supersonic flow field is dependent on the location it is measured due to the interference of the resulting disturbance waves. It is therefore important not only that the external compression model predicts this behavior correctly but that the normal shock wave is in the correct location for sub-critical operation as well. Overall, these results illustrate that the reduced order model correctly models the dynamics of the inlets response to small amplitude flow field perturbations.

Finally, the quasi 1-D inlet code ran much more efficiently than PHASTA for this type of simulation. The model was seen to simulate $532 timesteps/(min * proc)$ while PHASTA simulated only $0.041 timesteps/(min * proc)$. This is a factor of 13,000 times faster. These results were obtained by running the quasi 1-D inlet code on one processor for 4900 time steps which took 9.23 mins to complete. Likewise, PHASTA was run for 4000 time steps on 72 processors and took 1,365 mins to complete. Additional runs of both codes resulted in the same level of efficiency. PHASTA of course is a powerful generalized solver capable of solving a wide variety of flows while this code is tailored to simulate a supersonic inlet. Still, it speaks to the approach chosen, that this type of efficiency was able to be obtained while maintaining the desired accuracy.

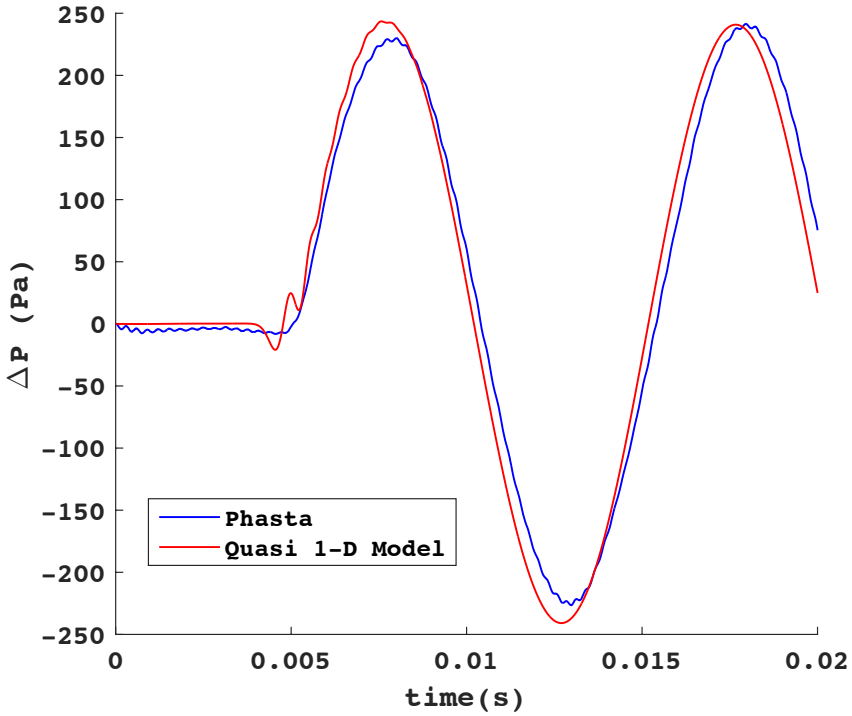

Figure 5.15: 100 Pa 100Hz pressure disturbance response with $P_B = 1.023P_{(Critical)}$

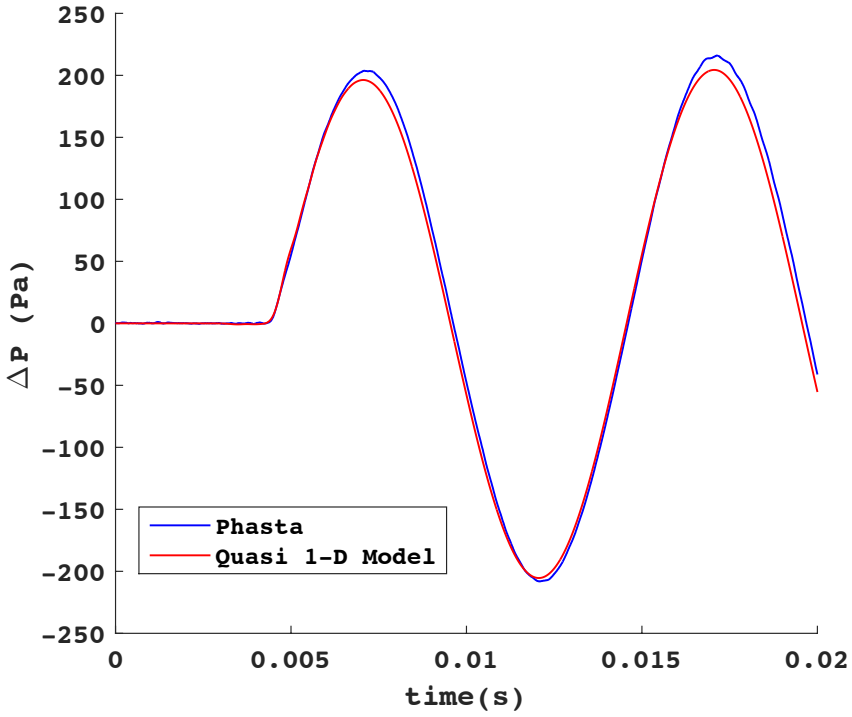

Figure 5.16: 100 Pa 100Hz pressure disturbance response with $P_B = 1.012P_{(Critical)}$

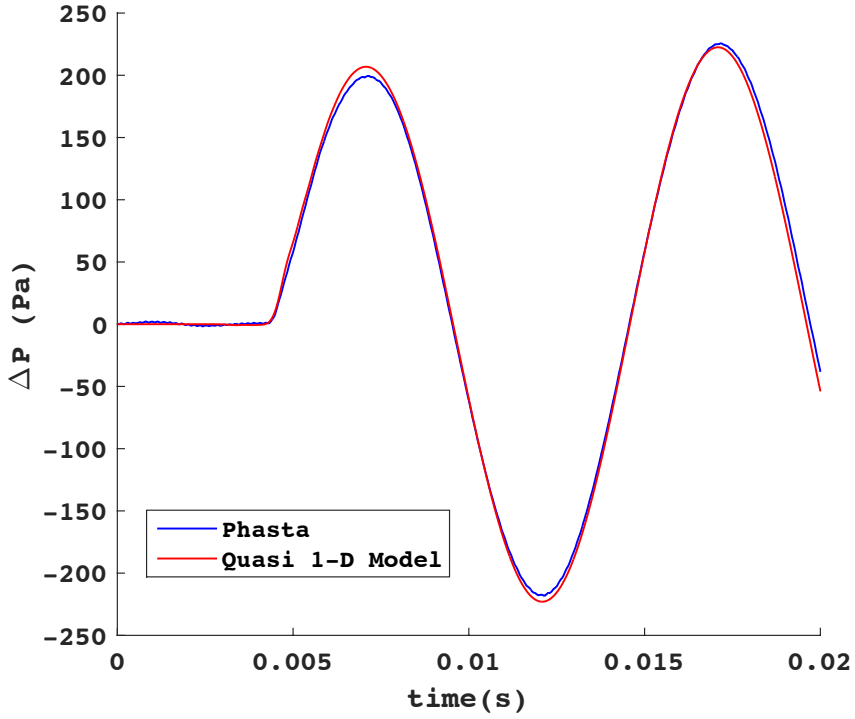

Figure 5.17: 100 Pa 100Hz pressure disturbance response with $P_B = 1.000 P_{(Critical)}$

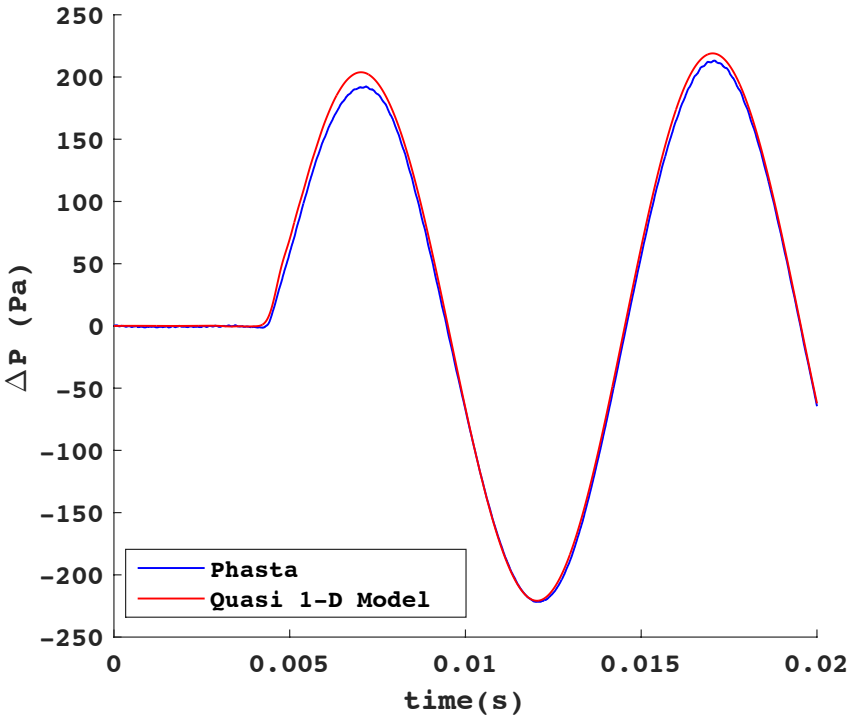

Figure 5.18: 100 Pa 100Hz pressure disturbance response with $P_B = 0.989 P_{(Critical)}$

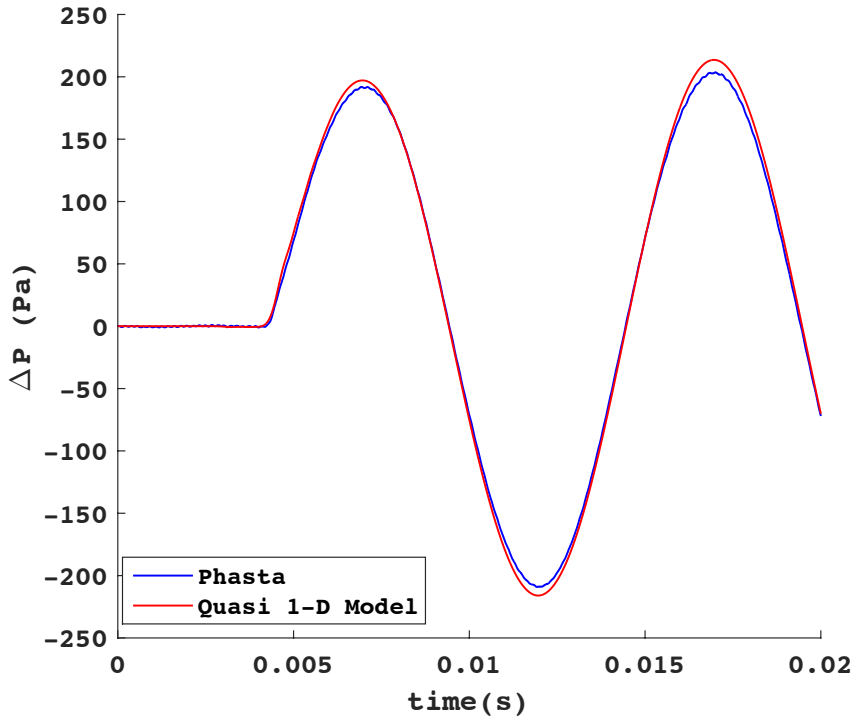

Figure 5.19: 100 Pa 100Hz pressure disturbance response with $P_B = 0.972P_{(Critical)}$

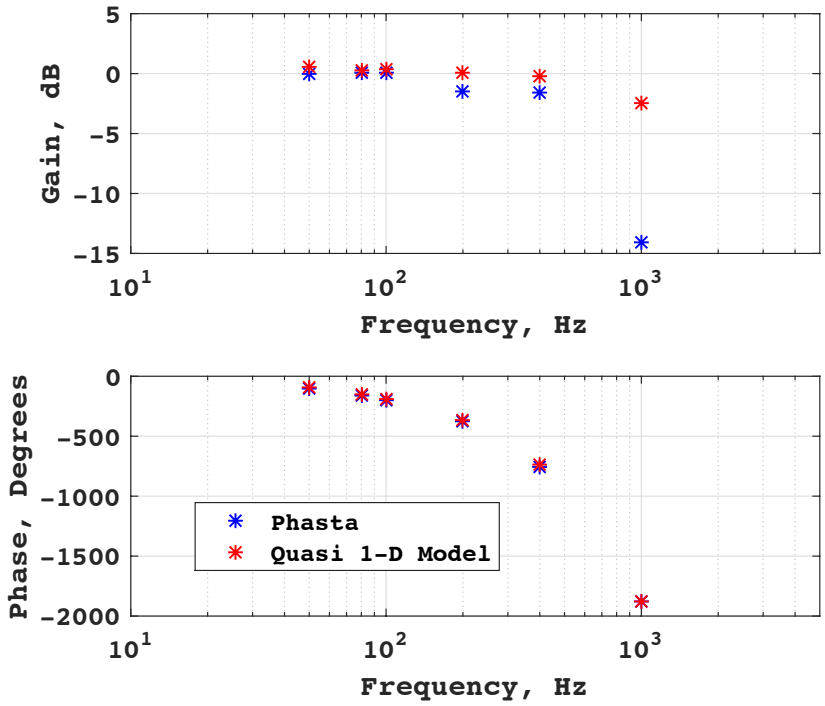

Figure 5.20: 100 Pa pressure disturbance Bode plot $P_B = 1.023P_{(Critical)}$

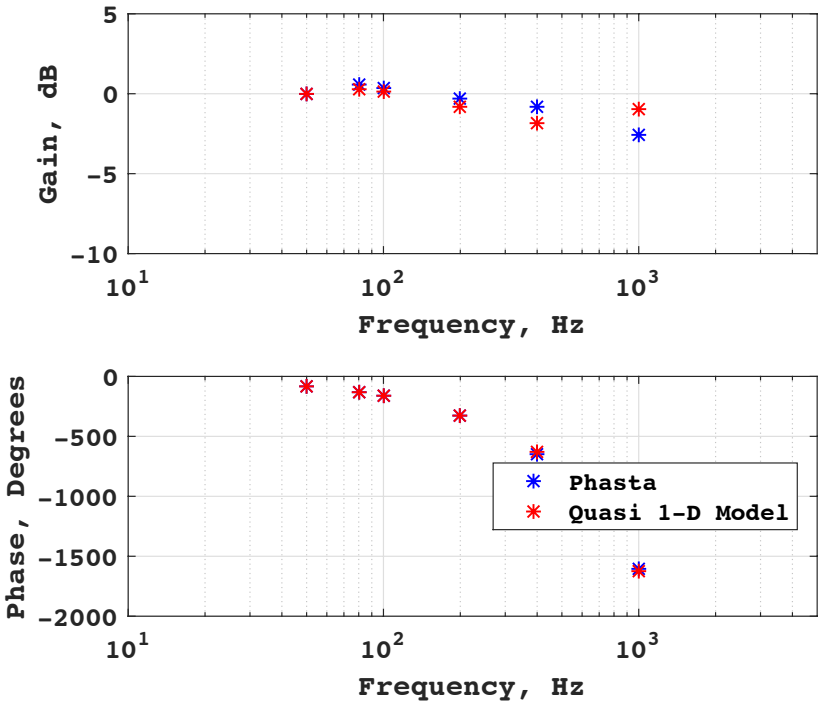

Figure 5.21: 100 Pa pressure disturbance Bode plot $P_B = 1.012 P_{(Critical)}$

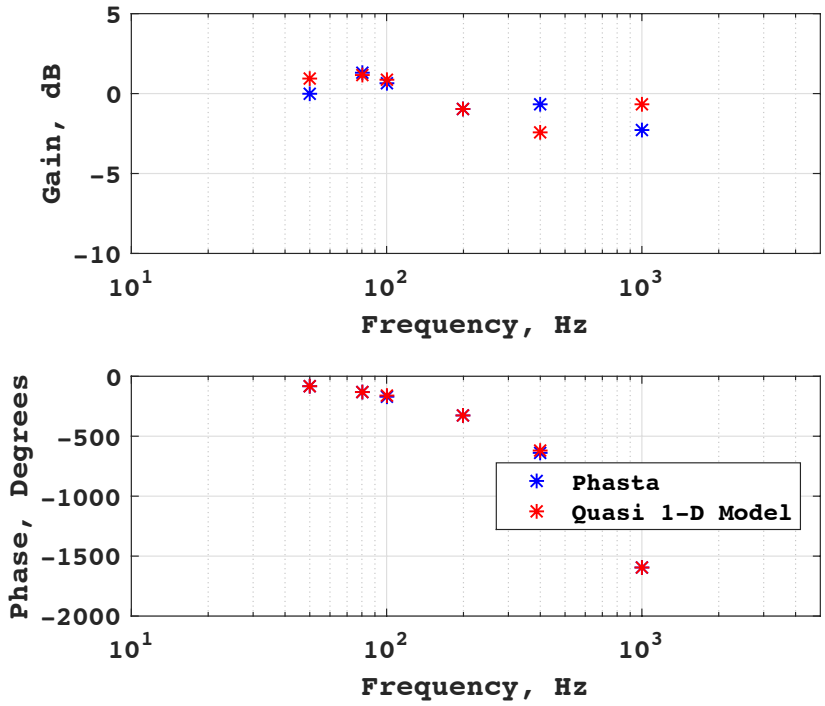

Figure 5.22: 100 Pa pressure disturbance Bode plot$P_B = 1.000 P_{(Critical)}$

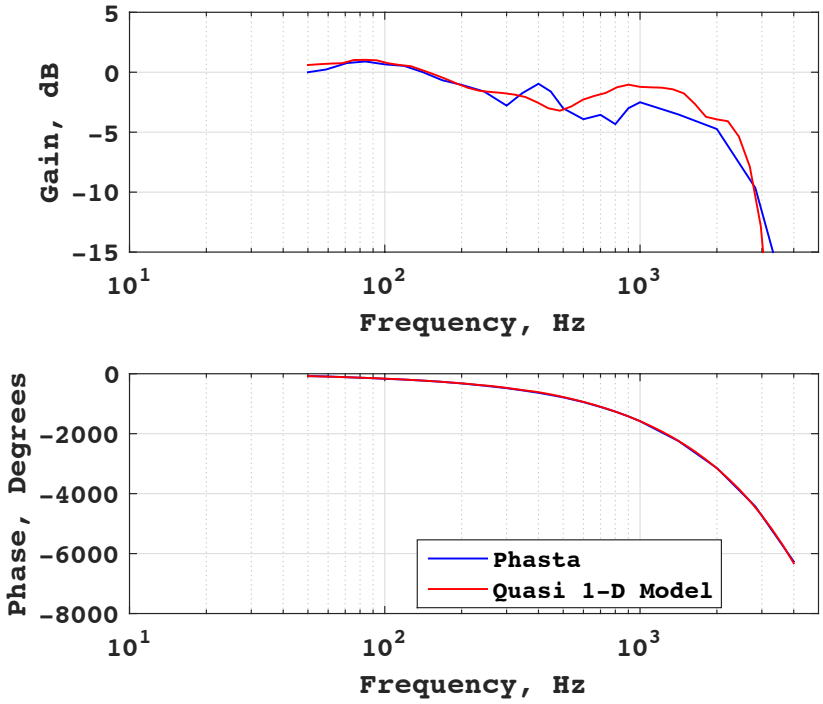

Figure 5.23: 100 Pa pressure disturbance Bode plot $P_B = 0.989P_{(Critical)}$

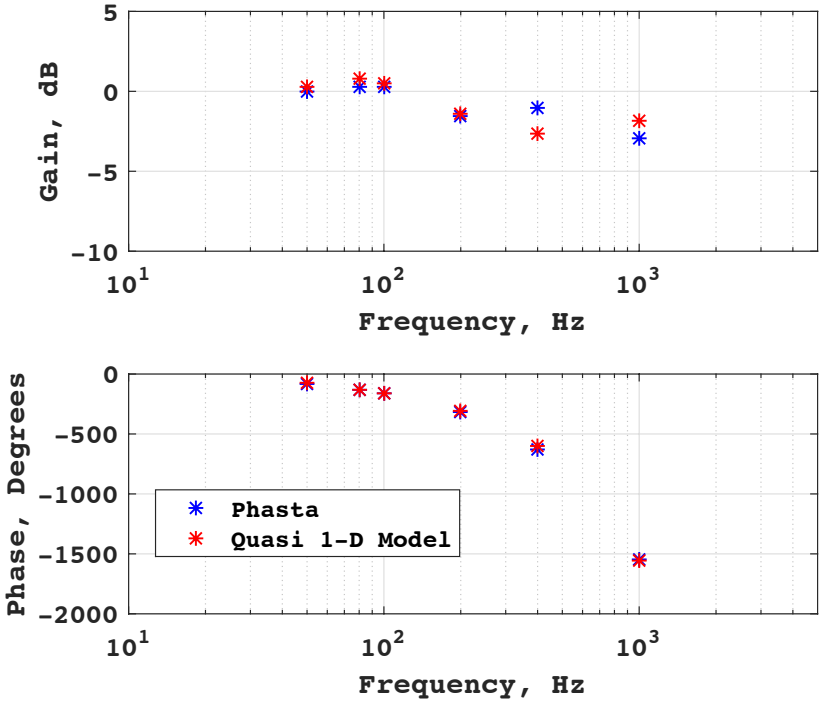

Figure 5.24: 100 Pa pressure disturbance Bode plot $P_B = 0.972P_{(Critical)}$

Chapter 6

Summary

The purpose of this research was to create a verified, dynamically accurate, general, quasi 1-D supersonic inlet model in the Matlab environment. The goals of this research were met by using a piecewise modeling approach by breaking up the inlet into five main sections which included the atmospheric model, the external compression region, the cowl lip region, the internal duct region, and the exit boundary conditions at the compressor face. These sections were modeled by combining established methods when possible and by creating new methods when necessary. Once complete, the reduced order inlet model was verified using the steady state and dynamic results of high fidelity CFD code PHASTA.

The first portion of the contained research established a baseline of results using PHASTA. Calibration tests were first performed using sample test cases to ensure that the settings were properly calibrated to analyze the inlet model. These sample tests included simulating a Riemann problem which was later used to establish the speeds of the characteristic waves which result from a flow variable perturbation. 2-D and 3-D models of the inlet were then simulated using PHASTA. These results were obtained both at steady state and dynamically over a wide range of operating conditions. This base of tests established the inlets response to both freestream perturbations and changes in back pressure. Additionally, these tests illustrated the effect of exit boundary location and how disturbances in the freestream can reflect off of this location and affect the solution within the flow field. The angle of attack perturbations using these models proved that the 2-D model is not capable of simulating these types of disturbances accurately. In retrospect, these are actually

two different types of disturbances with the 2-D angle of attack disturbance simulating a vortex ring rather than a change in angle of attack. Finally, the external compression portion of the inlet was isolated in order to visualize how free stream perturbations move through this region of the flow field. Using a step in freestream pressure, it was seen that the resulting disturbance waves are distorted as they move through the flow field due to the variation in local velocity and speed of sound. This result motivated the development of a novel dynamic external compression model.

In Section 4, a new dynamic external compression model was developed due to the findings of the previous chapter. This new approach involved decoupling a freestream flow disturbance into resulting disturbance waves and finding three new temporary 'steady state' solutions. These solutions were obtained using a combination of the Taylor-Maccoll equations and the Method of Characteristics. It was then shown that an accurate dynamic model could be obtained if these temporary solutions were transitioned between by finding the local transmission speed of each wave along streamlines. In this way the downstream characteristic speeds are averaged which results in an accurate 1-D representation downstream by taking the area weighted integral average of all of these streamlines. Again these results were verified using the CFD code PHASTA.

In the final chapter, the quasi 1-D inlet model was developed by piecing together established methods with the newly created external compression model. The Kopasakis model was used for the atmospheric model, the MacCormack method was used for internal duct portion and the Paynter method was used for the exit boundary conditions. In addition to these methods, a new cowl lip spillage model was created when it was found that the Lapin method was only viable for one operating condition. This new method was created using the results of PHASTA and while this caused the 1-D model to lose some of its generality, extending the model to new freestream operating points would require few additional CFD runs. Finally, the 1-D model was compared to PHASTA at both steady state and dynamically using freestream pressure perturbations over a range of frequencies. At each operating condition test, the 1-D model showed very little error when compared to PHASTA. The biggest errors encountered were at high frequency perturbations which are beyond the expected range of freestream perturbations.

In conclusion, there are several significant takeaways from this research. The main one is that this is the first accurate quasi 1-D external compression inlet, shown to operate at both sub-critical and super-critical operating points. This is mostly due to the novel external compression model developed during this research. All previous models were not capable of accurately simulating responses to freestream perturbations or at operating at multiple subcritical operating points. Additionally, this is the first quasi 1-D model to be verified dynamically by a high fidelity CFD code. Previous, models were only verified at steady state operation. Another take away is that this model was developed entirely in the Matlab environment. This makes it compatible with the remainder of the supersonic engine. In addition to that, it is also extremely efficient computationally. The model was seen to simulate $532 timesteps/(min * proc)$ while PHASTA simulated only $0.041 timesteps/(min * proc)$. This is a factor of 13,000 times faster. Finally, this inlet model is completely general with the exception of the spillage model as noted. This is a limitation, however extending the range of the model would require few additional CFD runs.

Going forward, there are a few recommendations to extend this research. The first would be to run the quasi 1-D model and PHASTA at different freestream Mach numbers. While the inlet model is general and should be able to operate at all supersonic freestream conditions below the hypersonic point, it would be good to extend the CFD data to enhance the spillage model. A second recommendation would be to replace the cowl lip spillage model using a physics based approach. This would allow the quasi 1-D model to be completely general but would most likely require a significant effort to complete. Finally, viscous simulations should me run using turbulence modeling to further verify the accuracy of the model. While it is believed that the behavior of the model should be dominated by inviscid phenomena, it is likely that certain subcritical operating points simulated may encroach on buzz limit which would greatly affect the performance at these points.

Bibliography

[1] U. Ahsun. Dynamic characterization and active control of unstarts in a near isentropic supersonic inlet. Master's thesis, MIT, Cambridge, Massachusetts, 2004.

[2] D. Amsallem and C. Farhat. Interpolation method for adapting reduced-order models and application to aeroelasticity. AIAA journal, 46(7):1803–1813, 2008.

[3] B. Anderson. Design of supersonic inlets by a computer program incorporating the method of characteristics. Technical Report 4960, NASA, 1969.

[4] J. Anderson. Modern compressible flow: with historical perspective. McGraw Hill Higher Education, 3 edition, 1990.

[5] J. Anderson. Computational Fluid Dynamics: The Basics with Applications. McGrawhill Inc, 1995.

[6] U.S. Standard Atmosphere. U.S. Government Printing Office, 1976.

[7] T. Bogar, M. Sajben, and J. Kroutil. Response of a supersonic inlet to downstream perturbations. Journal of Propulsion and Power, 1(2):118–125, 1985.

[8] A. N. Brooks and T. J. R. Hughes. Streamline upwind / Petrov-Galerkin formulations for convection dominated flows with particular emphasis on the incompressible Navier-Stokes equations. Comp. Meth. Appl. Mech. Engng., 32:199–259, 1982.

[9] K. Carlberg, C. Bou-Mosleh, and C. Farhat. Efficient non-linear model reduction via a least-squares petrov-galerkin projection and compressive tensor approximations. International Journal Numerical Methods in Engineering, 86(2):155–181, 2011.

[10] A. Chicatelli and T. Hartley. A method for generating reduced-order linear models of multidimensional supersonic inlets. Technical Report 207405, NASA, Hanover, MD., 5 1998.

[11] R. Chima. Analysis of buzz in a supersonic inlet. Technical Report 2012-217612, NASA, 2012.

[12] R. Chima, T. Conners, and T. Wayman. Coupled analysis of an inlet and fan for a quiet supersonic jet. AIAA Paper, 479, 2010.

[13] P. Chushkin. Numerical method of characteristics for three-dimensional supersonic flows. Progress in Aerospace Sciences, 9:41–122, 1968.

[14] J. Connolly, J.R. Carlson, G Kopasakis, and K. Woolwine. Nonlinear dynamic modeling of a supersonic commercialtransport turbo-machinery propulsion system for aero-propulso-servo-elasticity research. Technical report, 51st AIAA/ASME/SAE/ASEE Joint Propulsion Conference and Energy Forum (PowerPoint Slides), 2015.

[15] J. Connolly, G. Kopasakis, J.R. Carlson, and K Woolwine. Nonlinear dynamic modeling of a supersonic commercial transport turbo-machinery propulsion system for aero-propulso-servo-elasticity research. In ASME Turbo Expo 2015: Proceedings of the Turbine Technical Conference Exposition, pages 1–12, Montreal, Canada, 2015. ASME. GT2015-43681.

[16] M. Conway, A. Lavely, and G. Blaisdell. A computational investigation of flow through an axisymmetric supersonic inlet. AIAA, 2010. 2010-941.

[17] D. Dalle, M Fotia, and J. Driscoll. Reduced order models of 2d supersonic flow with applications to scramjet inlets. Journal of Propulsion and Power, 26(3):545–555, 2010.

[18] C. Fairall, A. White, and D. Thomson. A stochastic model of gravity-wave-induced clear-air turbulence. Journal of the atmospheric sciences, 48(15):1771–1790, 1991.

[19] D. Garrard, M. Davis, and G. Cole. A one dimensional, time dependent inlet / engine numerical simulation for aircraft propulsion systems. In Symposium on "Design Principles and Methods for Aircraft Gas Turbine Engines". RTO AVT Toulouse, France, 1998.

[20] NASA GRC. Taylor-maccoll solver at nasa grc website. `http://www.grc.nasa.gov/WWW/k-12/airplane/coneflow.html`. Accessed: 2015-03-30.

[21] N. Gupta, B. Gupta, N. Ananthkrishnan, G. Shevare, I. Park, and H. Yoon. Integrated modeling and simulation of an air-breathing combustion system dynamics. AIAA Paper, 6374, 2007.

[22] N. Gupta, B. Gupta, N. Anathkrishnan, G. Shevare, I. Park, and H. Yoo. Integrated modeling and simulation of an air-breathing combustion system dynamics. AIAA, page 31, 2007.

[23] B. He, J. Chang, W. Bao, and D. Yu. Supersonic inlet dynamics model based on equilibrium manifold. In 14th Space Planes and Hypersonic Systems and Technologies, page 8. AIAA/AHI, AIAA, 2006. 2006-7903.

[24] F. Hoblit. Gust loads on aircraft: concepts and applications. Aiaa, 1988.

[25] K. E. Jansen. Unstructured grid large eddy simulation of flow over an airfoil. In Annual Research Briefs, pages 161–173, NASA Ames / Stanford University, 1994. Center for Turbulence Research.

[26] K. E. Jansen. A stabilized finite element method for computing turbulence. Comp. Meth. Appl. Mech. Engng., 174:299–317, 1999.

[27] K. E. Jansen, C. H. Whiting, and G. M. Hulbert. A generalized-α method for integrating the filtered Navier-Stokes equations with a stabilized finite element method. Comp. Meth. Appl. Mech. Engng., 190:305–319, 1999.

[28] K.E. Jansen. Unstructured grid large eddy simulation of wall bounded flow. In Annual Research Briefs, pages 151–156, NASA Ames / Stanford University, 1993. Center for Turbulence Research.

[29] D. Knight. Elements of numerical methods for compressible flows, volume 19. Cambridge University Press, 2006.

[30] A. Kolmogorov. Dissipation of energy in locally isotropic turbulence. In Dokl. Akad. Nauk SSSR, volume 32, pages 16–18, 1941.

[31] G. Kopasakis. Atmospheric turbulence modeling for aero vehicles: Fractional order fits. Technical Report 2010-216961, NASA, 2010.

[32] G. Kopasakis. Modeling of atmospheric turbulence as disturbances for control design and evaluation of high speed propulsion systems. Journal of Dynamic Systems, Measurement, and Control, 134(2):021009, 2012.

[33] G. Kopasakis, J. Connolly, and J. Kratz. Quasi one-dimendional unsteady modeling of eternal compression supersonic inlets. Technical report, 48th AIAA/ASME/SAE/ASEE Joint Propulsion Conference and Exhibit (PowerPoint Slides), 2012.

[34] G. Kopasakis, J. Connolly, and J. Kratz. Quasi one-dimensional unsteady modeling of external compression supersonic inlets. In 48th Joint Propulsion Conference and Exhibit, page 12, Atlanta, Georgia, 8 2012. AIAA/ASME/SAE/ASEE, AIAA. 2012-4147.

[35] G. Kopasakis, J. Connolly, D. Paxson, and K. Woolwine. Quasi 1d modeling of mixed compression supersonic inlets. AIAA, page 15, 2012. 2012-0775.

[36] PK Kundu and IM Cohen. Fluid Mechanics. Elsevier Academic Press, 4 edition, 2008.

[37] G. Lassaux. High-fidelity reduced-order aerodynamic models: Application to active control engine inlets. Master's thesis, MIT, Cambridge, Massachusetts, 2002.

[38] T. Lieu and C. Farhat. Adaptation of aeroelastic reduced-order models and application to an f-16 configuration. AIAA journal, 45(6):1244–1257, 2007.

[39] T Lieu, C Farhat, and M Lesoinne. Reduced-order fluid/structure modeling of a complete aircraft configuration. Computer methods in applied mechanics and engineering, 195(41):5730–5742, 2006.

[40] D. MacMartin. Dynamics and control of shock motion in a near-isentropic inlet. Journal of Aircraft, 41(4):846–853, 2004.

[41] W. Moeckel. Approximate method for predicting form and location of detached shock waves ahead of plane or axially symmetric bodies. Technical Report 1921, NASA, 1949.

[42] G. Nastrom and K. Gage. A climatology of atmospheric wavenumber spectra of wind and temperature observed by commercial aircraft. Journal of the atmospheric sciences, 42(9):950–960, 1985.

[43] K. Numbers and A. Hamed. Development of a coupled inlet-engine dynamics analysis method. AIAA, pages 1–17, 1997.

[44] A. Opalski and M. Sajben. Inlet/compressor system response to short-duration acoustic disturbances. Journal of propulsion and power, 18(4):922–932, 2002.

[45] G. Paynter, L. Clark, and G. Cole. Modeling the response from a cascade to an upstream acoustic disturbance. AIAA journal, 38(8):1322–1330, 2000.

[46] J. Rakich. A method of characteristics for steady three-dimensional supersonic flow with application to inclined bodies of revolution. Technical Report 5341, NASA, 1969.

[47] M. Sajben and H. Said. Acoustic-wave/blade-row interactions establish boundary conditions for unsteady inlet flows. Journal of Propulsion and Power, 17(5):1090–1099, 2001.

[48] H. Sauerwein. Numerical calculations of multidimensional and unsteady flows by the method of characteristics. Journal of Computational Physics, 1(3):406–432, 1967.

[49] J. Seddon and E. L. Goldsmith. Intake aerodynamics. AIAA, 2 edition, 1999.

[50] J. Slater. Design and analysis tool for external-compression supersonic inlets. AIAA, page 20, 2012. 2012-0016.

[51] J. Slater. SUPIN: A Tool for the Aerodynamic Design and Analysis of Supersonic Inlets. NASA, 2014.

[52] V. Sorensen. Computer program for calculating flow fields in supersonic inlets. Technical Report 2897, NASA, Washington, D.C., 7 1965.

[53] W. Tank. Atmospheric disturbance environment definition. Technical Report 195315, NASA, 1994.

[54] W. Tank and J. Gillis. Atmospheric disturbance models for linear and nonlinear system response analysis. In AIAA 34th Aerospace Sciences Meeting and Exhibit, Reno, NV, 1996.

[55] C. A. Taylor, T. J. R. Hughes, and C. K. Zarins. Finite element modeling of blood flow in arteries. Comp. Meth. Appl. Mech. Engng., 158:155–196, 1998.

[56] G. Taylor and J. Maccoll. The air pressure on a cone moving at high speeds. i. In Proceedings of the Royal Society of London A: Mathematical, Physical and Engineering Sciences, volume 139, 838, pages 278–297. The Royal Society, 1933.

[57] M. Varner, W. Martindale, W. Phares, K. Kneile, and J.C. Adams. Large perturbation flow field analysis and simulation for supersonic inlets. Technical Report 174676, NASA, 1986.

[58] C. H. Whiting and K. E. Jansen. A stabilized finite element method for the incompressible Navier-Stokes equations using a hierarchical basis. International Journal of Numerical Methods in Fluids, 35:93–116, 2001.

[59] C. H. Whiting, K. E. Jansen, and S. Dey. Hierarchical basis in stabilized finite element methods for compressible flows. Comp. Meth. Appl. Mech. Engng., 192:5167–5185, 2003.

[60] K. Willcox, J. Peraire, and J. White. An arnoldi approach for generation of reduced-order models for turbomachinery. Computers & fluids, 31(3):369–389, 2002.